1993-03

Three dimensional vorticity field in the California current

Montenegro, Gonzalo

Monterey, California. Naval Postgraduate School

http://hdl.handle.net/10945/39873

AD-A276 951

NAVAL POSTGRADUATE SCHOOL
Monterey, California

DTIC
SELECTED
MAR 15 1994
S B D

THESIS

Three Dimensional Vorticity Field
In The California Current System

by

Gonzalo Montenegro

March, 1993

Thesis Advisor: Peter Chu

Approved for public release; distribution is unlimited.

DTIC QUALITY INSPECTED 1

94 3 14 023

REPORT DOCUMENTATION PAGE

1a Report Security Classification: Unclassified	1b Restrictive Markings

2a Security Classification Authority	3 Distribution/Availability of Report
2b Declassification/Downgrading Schedule	Approved for public release; distribution is unlimited.

4 Performing Organization Report Number(s)	5 Monitoring Organization Report Number(s)

6a Name of Performing Organization Naval Postgraduate School	6b Office Symbol (if applicable) OC	7a Name of Monitoring Organization Naval Postgraduate School

6c Address (city, state, and ZIP code) Monterey CA 93943-5000	7b Address (city, state, and ZIP code) Monterey CA 93943-5000

8a Name of Funding/Sponsoring Organization	6b Office Symbol (if applicable)	9 Procurement Instrument Identification Number

Address (city, state, and ZIP code)	10 Source of Funding Numbers			
	Program Element No	Project No	Task No	Work Unit Accession No

11 Title (include security classification) THREE DIMENSIONAL VORTICITY FIELD IN THE CALIFORNIA CURRENT

12 Personal Author(s) Gonzalo Montenegro

13a Type of Report Master's Thesis	13b Time Covered From To	14 Date of Report (year, month, day) MARCH 1993	15 Page Count 108

16 Supplementary Notation The views expressed in this thesis are those of the author and do not reflect the official policy or position of the Department of Defense or the U.S. Government.

17 Cosati Codes			18 Subject Terms (continue on reverse if necessary and identify by block number)
Field	Group	Subgroup	THREE DIMENSIONAL VORTICITY, C-VECTOR, CALIFORNIA CURRENT, Ψ FUNCTION

19 Abstract (continue on reverse if necessary and identify by block number)

Hydrographic data has traditionally been used only to determine dynamical features, specifically dynamic topography and geostrophic currents relative to an assumed level of no motion. However, the assumption of geostrophic balance has been questioned because of the neglect of ageostrophic effects. Measuring vorticity and vertical motion has always been technically demanding and costly. Due to the importance of these parameters new techniques have been developed, among them a diagnostic technique known as the C-vector Method, which uses the wind stress and the geostrophic balance as forcing functions to infer these quantities.

Using this technique, the three dimensional vorticity field was computed for the California current system during the Coastal Transition Zone (CTZ) program (17-26 March, 1987). Hydrographic (CTD) and wind data sets were used, assuming a "quasi-geostrophic" system. Also computed was the vertical vorticity of the C-vector, known as the Ψ function, which has a direct relationship with the vertical velocity, making it possible to infer upward or downward motion in coastal waters.

A satisfying correlation was found between surface temperature fields, satellite imagery, and vertical motions inferred from the Ψ function. The C-vector has therefore been shown to be a very reliable method of diagnosing vorticity and vertical circulation.

20 Distribution/Availability of Abstract __ unclassified/unlimited X_ same as report __ DTIC users	21 Abstract Security Classification Unclassified	
22a Name of Responsible Individual Peter Chu	22b Telephone (include Area Code) 408-656-3257	22c Office Symbol OC/Cu

Three Dimensional Vorticity Field In The California Current

by

Gonzalo Montenegro
Lieutenant, Ecuadorian Navy
Ecuadorian Naval Academy, 1983

Submitted in partial fulfillment
of the requirements for the degree of

MASTER OF SCIENCE IN METEOROLOGY AND PHYSICAL OCEANOGRAPHY

from the

NAVAL POSTGRADUATE SCHOOL
March, 1993

Author: _____
Lieutenant Gonzalo Montenegro

Approved by: _____
Associate Professor Peter Chu, Thesis Advisor

_____
Professor R. W. Garwood, Second Reader

_____
Professor Curtis A. Collins, Chairman,
Department of Oceanography

ii

ABSTRACT

Hydrographic data has traditionally been used only to determine dynamical features, specifically dynamic topography and geostrophic currents relative to an assumed level of no motion. However, the assumption of geostrophic balance has been questioned because of the neglect of ageostrophic effects. Measuring vorticity and vertical motion has always been technically demanding and costly. Due to the importance of these parameters new techniques have been developed, among them a diagnostic technique known as the C-vector Method, which uses the wind stress and the geostrophic balance as forcing functions to infer these quantities.

Using this technique, the three dimensional vorticity field was computed for the California current system during the Coastal Transition Zone (CTZ) program (17-26 March, 1987). Hydrographic (CTD) and wind data sets were used, assuming a "quasi-geostrophic" system. Also computed was the vertical vorticity of the C-vector, known as the Ψ function, which has a direct relationship with the vertical velocity, making it possible to infer upward or downward motion in coastal waters.

A satisfying correlation was found between surface temperature fields, satellite imagery, and vertical motions inferred from the Ψ function. The C-vector has therefore been shown to be a very reliable method of diagnosing vorticity and vertical circulation.

TABLE OF CONTENTS

LIST OF TABLES

LIST OF FIGURES

I. INTRODUCTION

A. PURPOSE

Direct measurement of ocean currents with sufficient spacial and temporal coverage to be useful is technically demanding and costly. In shallow water, current meters may be suspended from an anchored ship in order to measure currents at several depths simultaneously. However, this procedure only gives information about the currents at a single geographic location. Also, an anchored ship does not remain stationary, but rather moves in relation to the anchor. This is a source of error for the measured current that increases with the length of the anchor line. Another, more practical method is to suspend current meters from a moored buoy. A number of such buoys moored in a pattern in the ocean will provide information about the three dimensional distribution of currents as a function of time. However, because of the expense, difficulties at sea, and the complicated nature of the currents, it is not possible to obtain observations over as much of the ocean as we would like. Thus, the geostrophic method is the primary method to determine currents.

The geostrophic method calculates the currents indirectly from the density distribution in the ocean; it is easier to measure temperature and salinity than to measure currents directly. In fact, most of our knowledge of the ocean circulation below the surface has been obtained in this way. The geostrophic method is also useful in strong currents for which it is difficult to moor recording current meters. This method still has

1

some disadvantages, such as the lack of vertical motion information (Pond and Pickard, 1983).

This work deals with the development of a new system for diagnosing the three-dimensional ageostrophic circulation in the Coastal Transition Zone (CTZ) using hydrographic and wind data sets. In this system, the flow contains two parts: geostrophic circulation and ageostrophic circulation. First, the geostrophic currents are obtained directly from the hydrographic data using traditional methods. Then, the ageostrophic circulation is assumed to be forced by the geostrophic currents (a phenomenon called geostrophic forcing) and by the surface wind stress.

B. THE CALIFORNIA CURRENT SYSTEM

1. Water Masses

There are four water masses in the California current system. Each has its own characteristic temperature, salinity, dissolved oxygen, and nutrients.

a. Pacific Subarctic Water

Following Simpson (1984), this is formed from the Oyashio and Kuroshio extension and carried eastward to the North America continent as part of the Subarctic Current and West Wind Drift. This flow collides with the continent near 48N. Part of it separates and is diverted south into the California current with water that is relatively low in temperature and salinity, but high in oxygen and phosphate.

Although this water mass mixes with the California Current and increases its temperature as it moves southward, it gives the offshore California Current its low

2

salinity and high dissolved oxygen near the surface.

b. *North Pacific Central Water*

Formed in the central Pacific between depths of 100 to 800m, the North Pacific Central is the least saline of the central water masses of the Pacific Ocean. This warm, salty water is relatively low in dissolved oxygen and nutrients, and enters the California System from the west.

c. *Upwelled Waters*

Found within 50km of the coast, this water is relatively cold, salty, and high in nutrient content and oxygen. Upwelled water is the result of the Ekman transport of surface waters away from the coast at times of equatorward winds along the coast.

d. *Equatorial Pacific Water*

Formed in the eastern tropical Pacific below a strong thermocline with waters of high temperature, salinity and nutrients, but low dissolved oxygen, Equatorial Pacific water enters the California Undercurrent from the south (Simpson, 1984).

2. Current System

The California Current System consists of the California Current and the California Undercurrent.

The California Currents lie between 0 and 200m depth. Offshore, the flow takes place equatorward during the whole year. Near the coast there is a fall-winter reversal, creating the California Countercurrent (Simpson, 1984).

TABLE 1.1.	RELATIVE COMPARISON OF WATER MASSES OF THE CALIFORNIA CURRENT SYSTEM (L = Low; H = High) (Simpson, 1984)				
		T	S	O_2	Nutrients
	Surface Water Masses (0-200m)				
a.	Pacific Subarctic	L	L	H	H
b.	N. Pacific Central	H	H	L	L
c.	Coastal Upwelled	L	H	L	H
	Subsurface Water Masses (200-500m)				
d.	Equatorial Pacific	H	H	L	H

The California Undercurrent, with its core at about 300m depth, originates in the eastern equatorial Pacific and runs poleward throughout the year. This poleward flow has been observed at different levels in different seasons (Huyer et al., 1989).

In the winter season there is a broad northward surface current, named the Davidson Current. It is seen between October and March, with the strongest mean flow in January or February at a speed of 20-30 cm/sec. North of Pt. Conception the Davidson Current is wider than the shelf, but the strongest flow is over the inner shelf against the coast. The current is forced by the southeasterly winds in winter, which cause downwelling at the coast due to the Ekman transport. This combines with increased coastal runoff during the rainy season and sets up an offshore density gradient that causes the northward geostrophic current (Huyer et al., 1989).

4

Also, there are inshore surface currents during the upwelling season in southern and central California. These currents seem to be inshore of the upwelling jet that flows south. The poleward flow is evident most of the year in the Southern California Bight. In that area it appears to form the inshore side of a large cyclonic eddy that fills the Bight. Further north, the poleward surface current can appear whenever the equatorward winds relax. It is much narrower here, 10-20km compared to up to 100km in the Bight. Velocities reach about 30 cm/s. A similar current is off central Oregon in mid and late summer. It is believed that these countercurrents are driven by an along-shore pressure gradient that balances the equatorward wind stress. That is why they are most intense when the winds relax (Huyer et al., 1989).

3. Wind Forcing

a. Wind Driven Circulation

The wind driven circulation affects only the upper few hundred meters. Therefore, it is considered predominately a horizontal circulation in contrast with the thermohaline circulation.

b. Coastal Upwelling

Coastal upwelling occurs along the entire west coast of the North American continent, and is primarily due to Ekman transport of surface waters offshore forced by the alongshore equatorward winds .

This upwelling is forced by atmospheric circulation around the North Pacific High which varies seasonally in both strength and position. The High migrates from its most southerly position at 28°N, 130°W in February, to its most northerly

5

TABLE 1.2. SUMMARY OF THE POLEWARD FLOW NEAR NORTHERN AND SOUTHERN BOUNDARIES OF THE U.S. WEST COAST (Hickey, 1989)

WASHINGTON SHELF/SLOPE VS. OREGON SHELF/SLOPE			
	Washington Shelf	Washington Slope	Oregon Shelf/Slope
Spring/Summer	Equatorward at all depths (spring). Considerable vertical shear and flow reversals over upper 20m.	Poleward (below 100m). Sub-surface maximum at shelf break. Vertical shear maximum.	Equatorward (down to 400m) due to strong equatorward winds here vice Washington.
Fall/Winter	Poleward (except late winter). Increases from mid-to outer-shelf. Equatorward (late winter due to Columbia River plume).	Poleward Sub-surface minimum at ~400m.	Poleward but less so than Washington. Decreases from mid to outer shelf. Equatorward vertical shear. Some flow reversals with depth.
SOUTHERN CALIFORNIA BIGHT SHELF VS. SLOPE			
	Shelf	Eastern Santa Monica Basin Slope	Western Santa Monica Basin Slope
Spring/Summer	Equatorward except at 30m and 60m during August (for narrow shelf in southern part of bight).	Poleward from 40m ot 100m everywhere except off San Onofre in spring at 40m. Sub-surface maximum.	Poleward Sub-surface maximum. Vertical shear maximum like Washington slope.
Fall/Winter	Equatorward strongest during these seasons.	Poleward everywhere except off San Onofre at 40m in early fall. Sub-surface maximum.	Equatorward (after October at 40m and 100m)

6
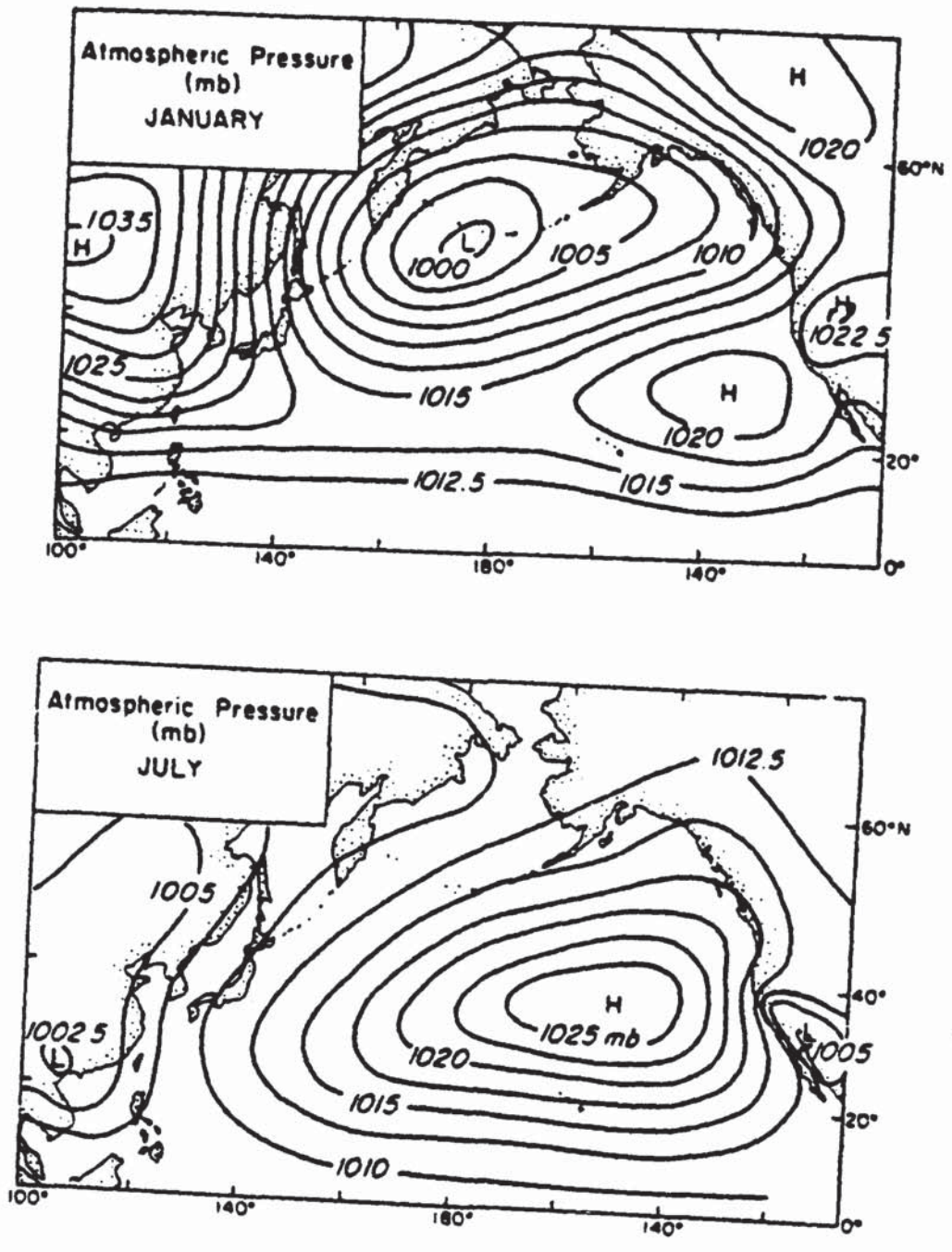
Figure 1.1. Long-Term mean atmospheric pressure at sea level for January and July (Anon, 1961).

7
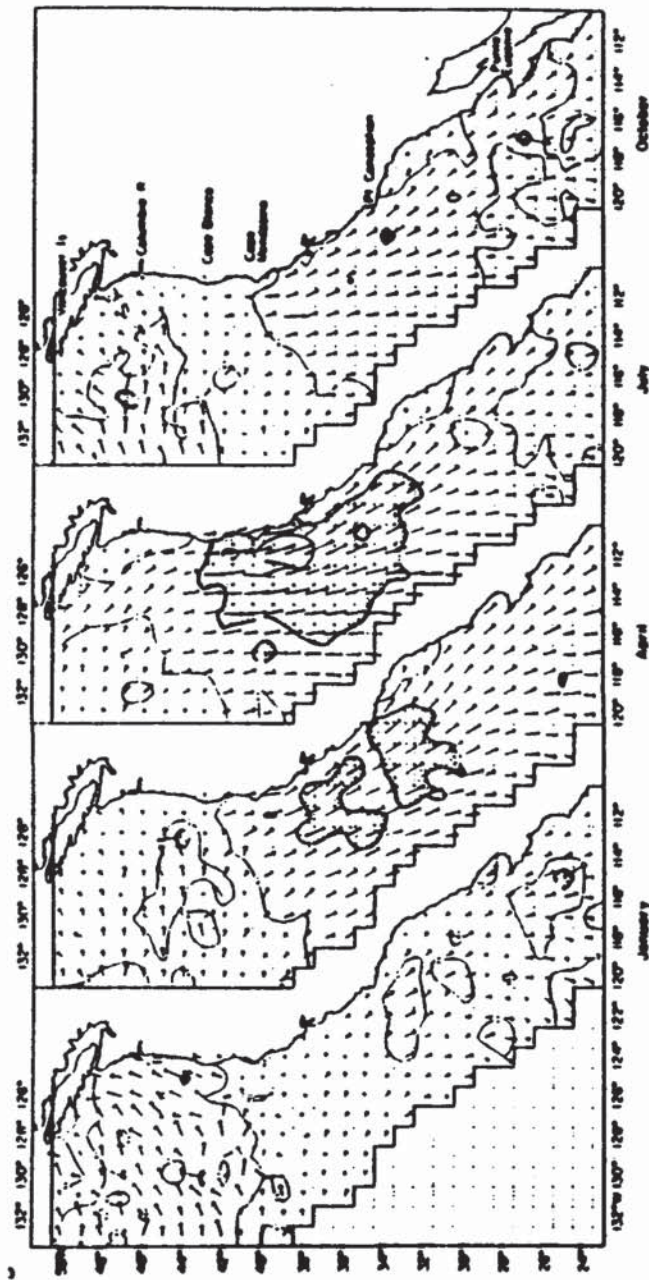
Figure 1.2. Mean wind stress 1854-1972. Contours are constant magnitudes of 0.5, 1.0, and 1.5 dynes cm^2; in shaded areas the wind stress exceeds 1.0 (Nelson, 1977).

8

position at 38°N, 150°W in August, and back again; the maximum pressure increases from winter (1020mb) to summer (1025mb) as shown in Figure 1.1. The atmospheric pressure over the extreme western United States is much higher in winter (~1020mb), when the surface is cold, than it is in summer (~1015mb), when the surface is warm. This thermal effect on pressure is particularly marked in California's central valley, where the Thermal Low reaches 1005mb in July. The offshore pressure gradient along the west coast is strongest in summer. The strength of the pressure gradient across coastal waters varies with position along the coast, with season, and obviously with day to day variations in the weather.

As shown in Figure 1.2, the region of maximum equatorward wind stress migrates northward from 25°N in January to 39°N in July, as expected from the pressure distribution shown in Figure 1.1. The strongest equatorward winds are observed in July off northern California, where the center of the High is closest to the Thermal Low. South of about 40°N, winds are equatorward all year round. North of this latitude, the wind stress is northward (e.g., unfavorable for coastal upwelling) in winter.

The alongshore wind stress, τ, causes a net offshore transport in the surface Ekman layer, τ/f, which in turn equals the amount of water that upwells along the coast. The Coriolis parameter, f, increases from $0.6 \times 10^{-4} s^{-1}$ at 24°N to $1.1 \times 10^{-4} s^{-1}$ at about 50°N; thus favorable winds of the same magnitude will result in nearly twice as much upwelling off southern Baja California as off northern Washington. Short-term fluctuations with periods of several days in the wind stress can cause upwelling, even when the mean wind stress for a given month is not favorable.

9

Open ocean upwelling can occur away from the coastal boundary if there is a positive curl in the wind stress field, i.e., if there is net divergence in the Ekman transport field. For example, if offshore winds are more strongly southward than coastal winds, there is stronger seaward Ekman transport offshore than near the coast, and there must be upwelling away from the coast as well as along the coast (Figure 1.3). Gradients in the actual wind field are likely to be very much stronger near shore, particularly near large headlands such as Cape Mendocino, and along steep coastal mountain ranges (Huyer, 1983).
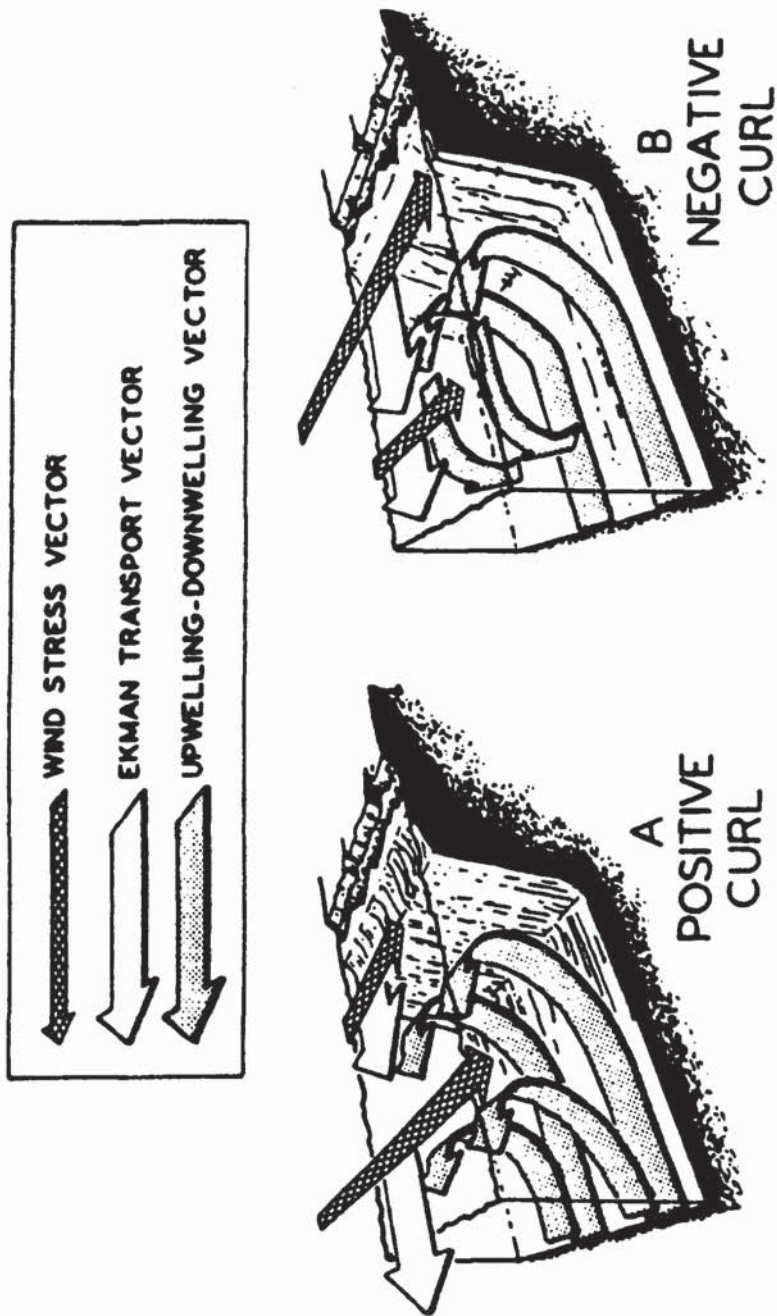
Figure 1.3. Relationship of along-shore winds and coastal upwelling and of wind stress curl and divergence/convergence of surface Ekman transport offshore (Nelson, 1977).

11

II. DATA

Hydrographic (CTD) data used in this study was collected from a cruise off central California during 17 - 26 March 1987 as part of the ONR Coastal Transition Zone (CTZ) Program. The CTZ program studied the spring summer transition in the California coast. The spring transition is defined as the event that causes the passage from the typical winter regime with level isopycnals and no mean vertical shear to the typical spring/summer regime with sloping isopycnals and a mean southward surface current and a strong mean vertical shear (Huyer et al., 1979). It was observed to occur in mid-March during the CTZ in 1987.

A. Coastal Transition Zone Program

The CTZ program was designed to understand the dynamics and implications of structures known as "filaments." Filaments are cold features in surface temperature, typically less than 100 km wide but hundreds of kilometers long which extend offshore from near the coast. Typically, they are accompanied by high concentrations of chlorophyll.

Eastern boundary currents have been characterized as eddy-rich and strongly time-dependant with spatially structured variability in the flow field. Bernstein et al., (1977) demonstrated that the complex structures visible in satellite infrared (IR) imagery could be matched to comparable variability measured throughout traditional in-situ means.

12

Satellite images revealed long tongues or filaments of cold, high-chlorophyll water extending from the coastal zone out to 200 km from shore. These were associated with:

1. strong, narrow seaward currents (surface drifters suggested upwelled waters directed offshore);

2. continuation of a strong shoreline coastal jet flowing generally southward along the upwelling front; and

3. pairs of oppositely rotating eddies.

Four cruises were made during February/June 1987. Buoys, ships, satellites, aircrafts and several instruments were used to collect diverse variables and data (Brink and Cowles, 1991).

B. Hydrographic Data

The hydrographic data was collected from a cruise off central California during 17-26 March 1987 as part of a study of the CTZ project, and was reported by Jessen et al. (1989). The study area was from Pt Reyes, California to Pt. St. George, Oregon from the coast to 150 km offshore.

1. Planned Sampling Grid

The planned sample grid shown in Figure 2.1 consists of two shoreline sections 150 and 90 km offshore, a discontinuous shoreline section 60 km offshore, and four across-shore sections. The across-shore sections divided the sampling grid into three separate modules (A,B, and C).

13

2.   Actual Sampling Grid

The actual sampling grid differed from the original due to weather and time constraints. A total of 96 CTD casts (Figure 2.2) to 500 m depth and 55 XBT drops (Figure 2.3) were made during this cruise.

Additionally, maps of hourly averaged wind vectors, surface temperature, salinity, and dynamic height relative to 500 db are presented in Figue 2.4-2.7, respectively.

3.   Data Acquisition and Calibration

Hydrographic data was acquired using a Neil Brown Mark III-B CTD and Sippican T-4 XBTs. A General Oceanic Rosette Sampler was attached to the CTD and equipped with twelve 5 liter Niskin bottles for in-situ water sampling. The CTD sampling rate was 32 Hz, but the acquisition software employed a latch filter which limited the number of data points collected during each cast to 4,308. On the 500 m casts this resulted in the acquisition of 8 or 9 data points per meter of water. CTD data was acquired only on the downcast with a winch speed of approximately 30 m/min to 150 m then 60 m/min to 500m. The data was acquired using an HP200 computer and stored on 3.5 inch diskettes. Upon return, the data was then transferred to a nine track tape and processed on an IBM 3033 mainframe computer. In addition to the CTD and XBT data, an underway data acquisition loop recorded 30-second averages of sea surface temperature and salinity, sea surface skin temperature, wind speed and direction, air temperature, and dew point temperature. The sensors used to acquire this data included Seabird temperature and conductivity sensors for the sea surface temperature and salinity, a

14
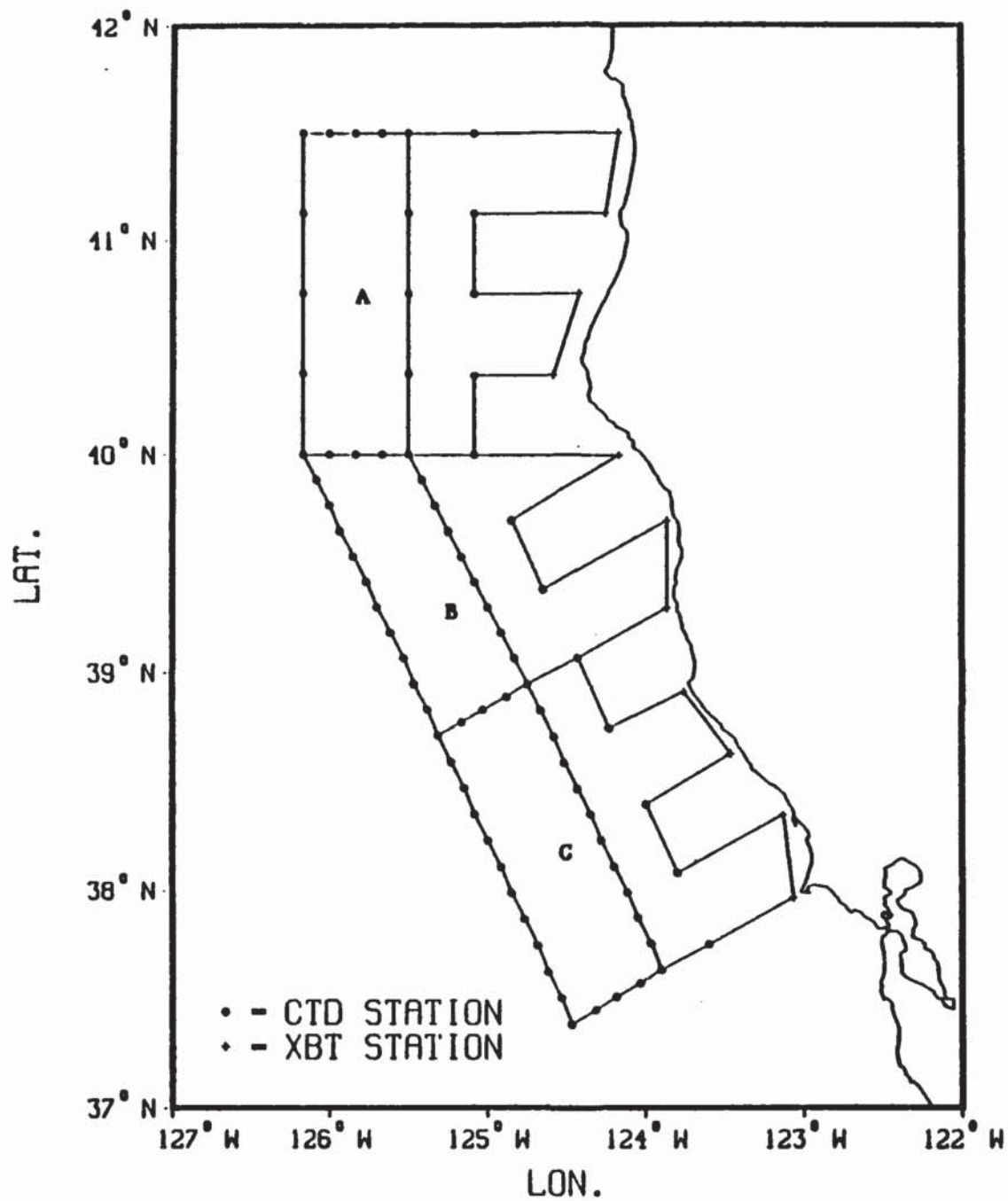
Figure 2.1. Planned CTD and XBT station locations for the Coastal Transition Zone (Jessen, et al., 1989).

15
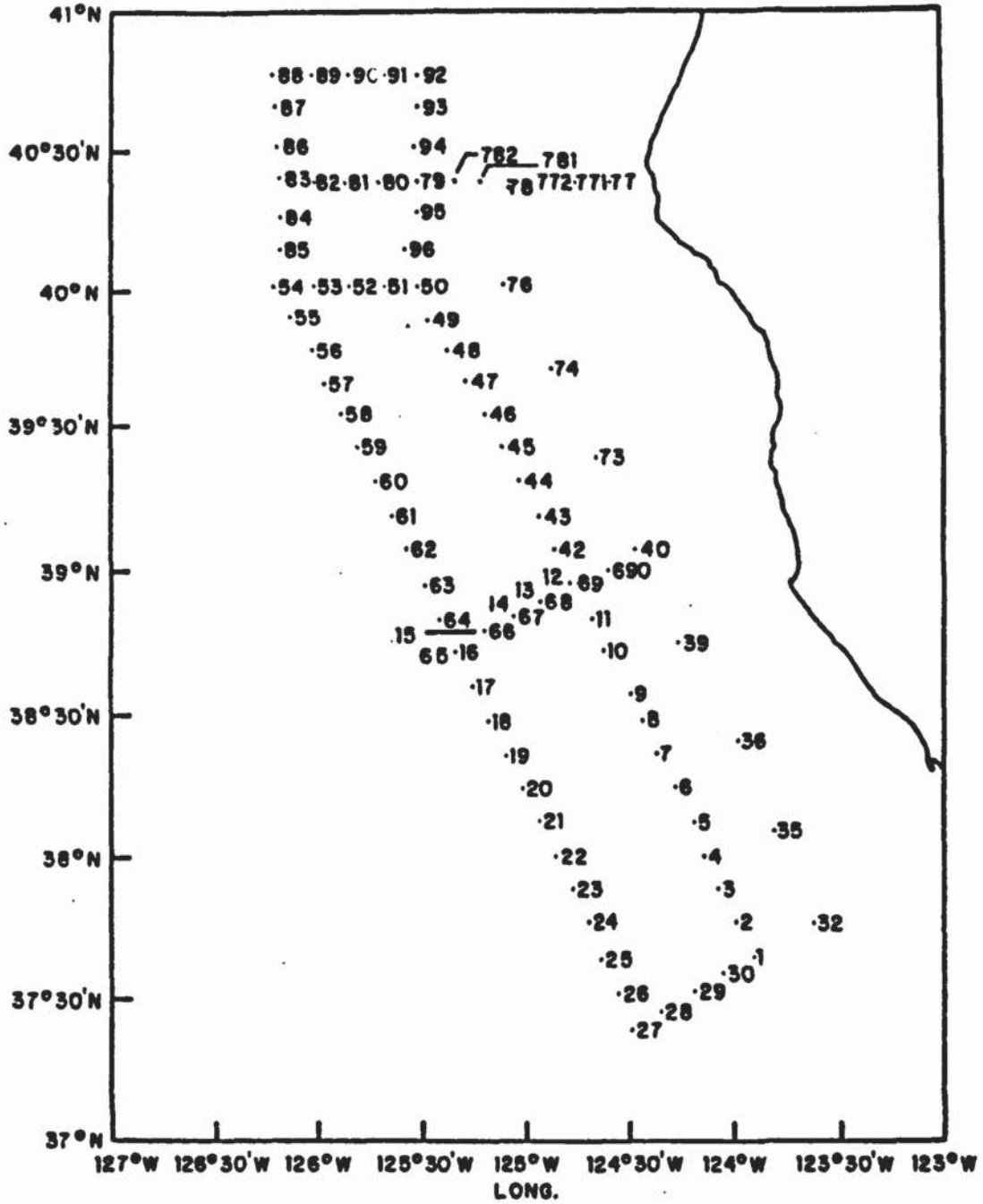
Figure 2.2. Actual CTD station numbers and locations for Cruise CTZ1 during March 17-26, 1987 (Jessen, et al., 1989).

16
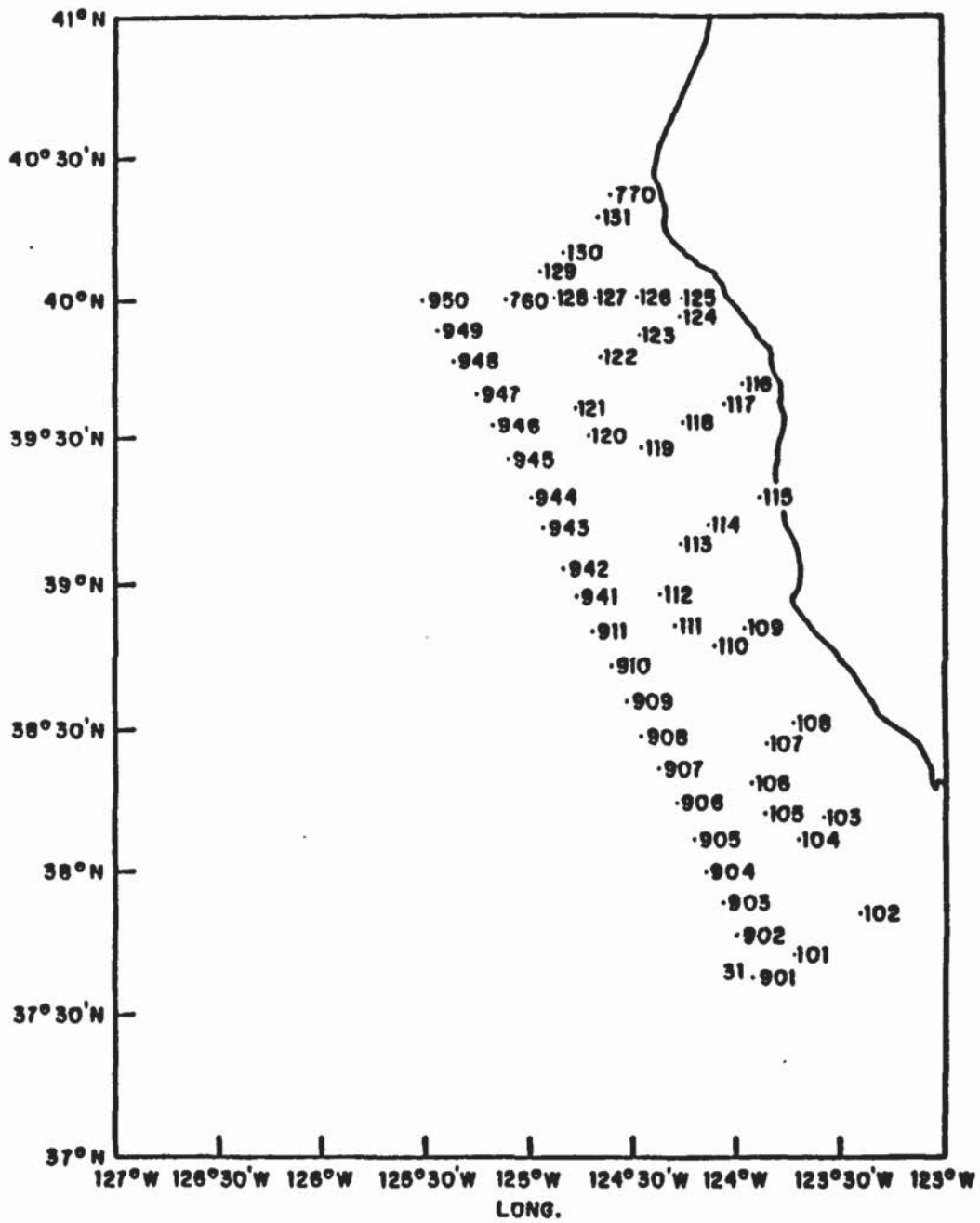
Figure 2.3. Actual XBT station numbers and locations for Cruise CTZ1 during March 17-26, 1987. (Jessen, et al., 1989)

17
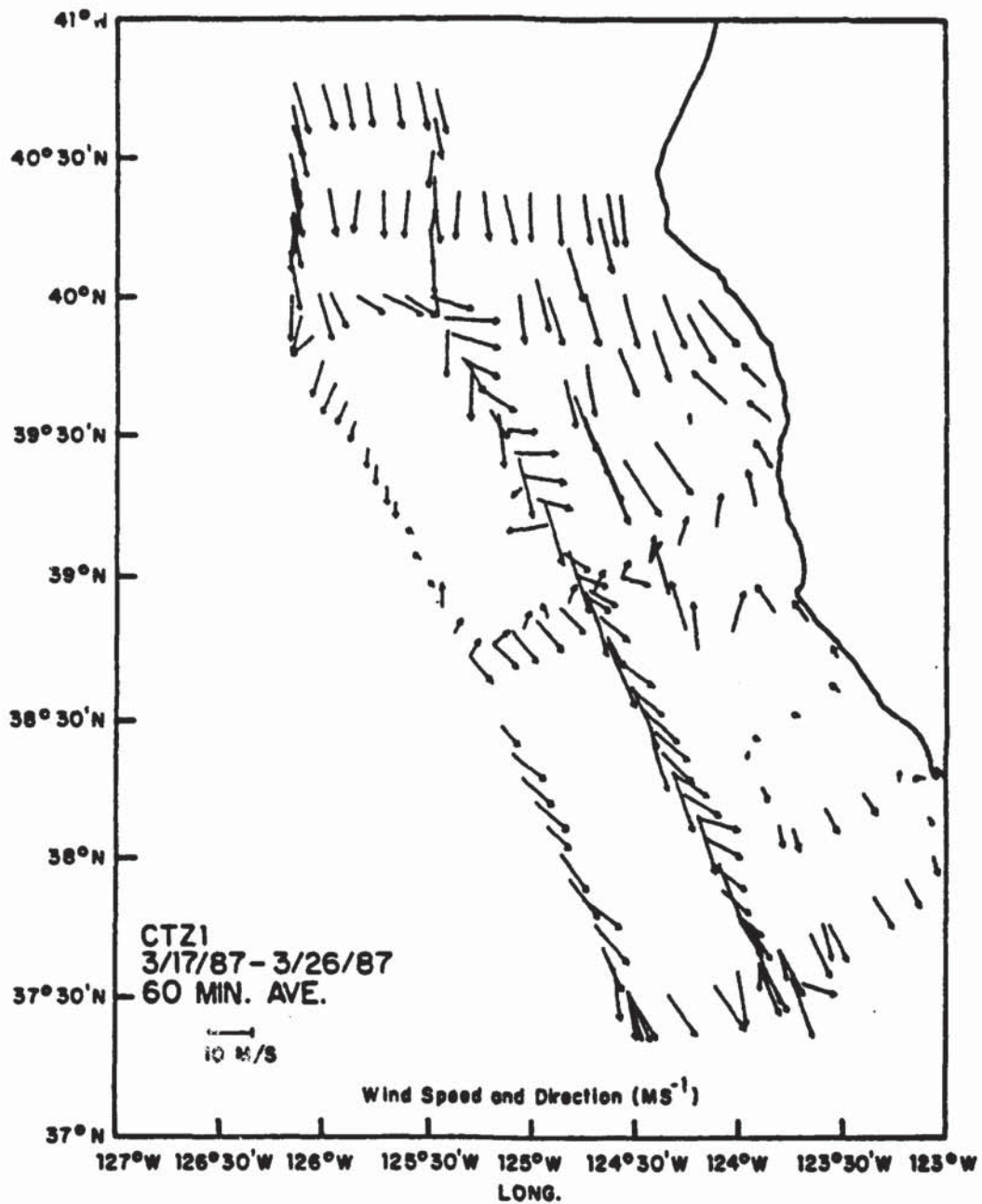
Figure 2.4. Hourly average of wind speed and direction measured at 10m height on March 87. (Jessen, et al., 1989)
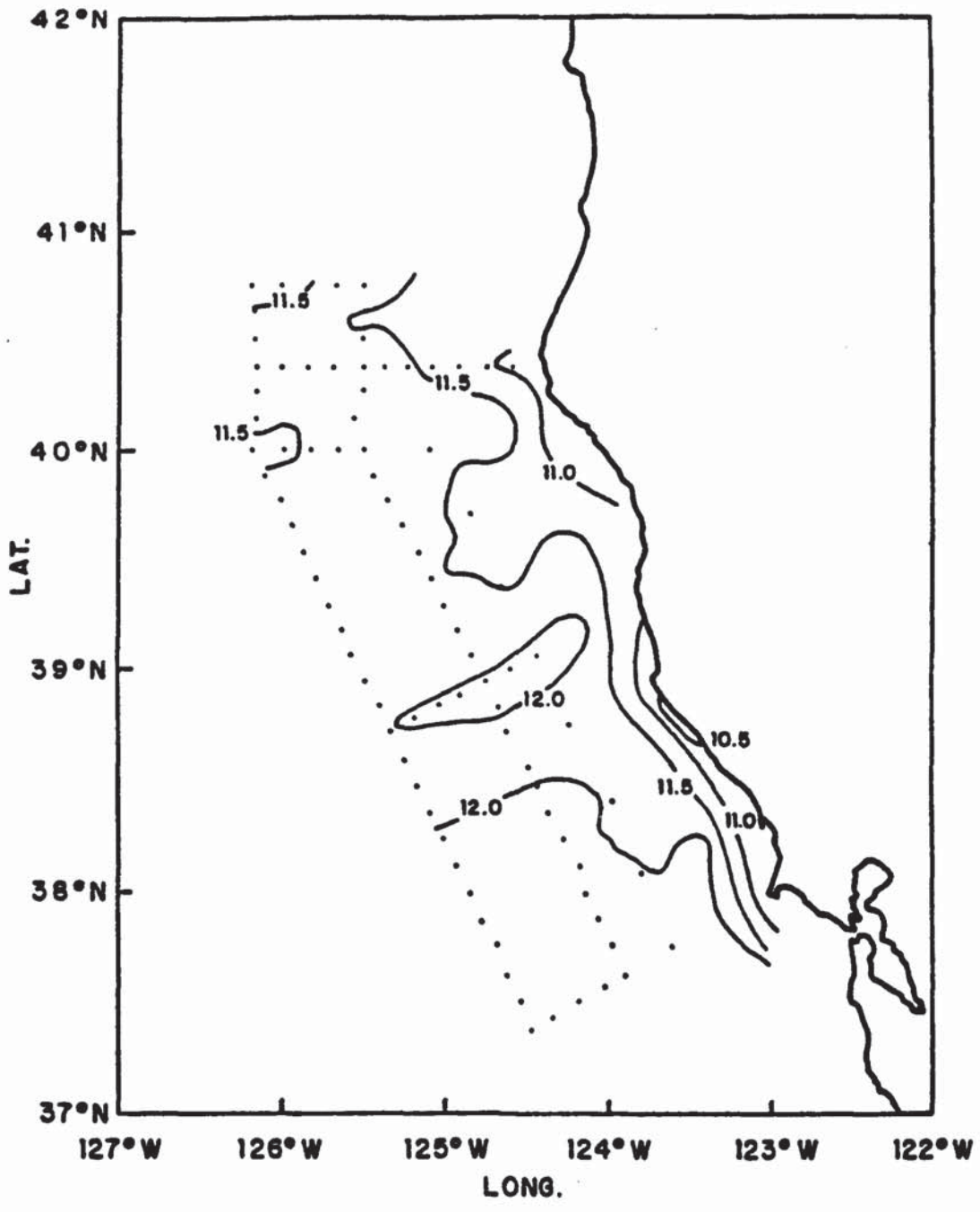
Figure 2.5. Map of surface temperature during Cruise CTZ1, March 17-26, 1987. (Jessen, et al., 1989)
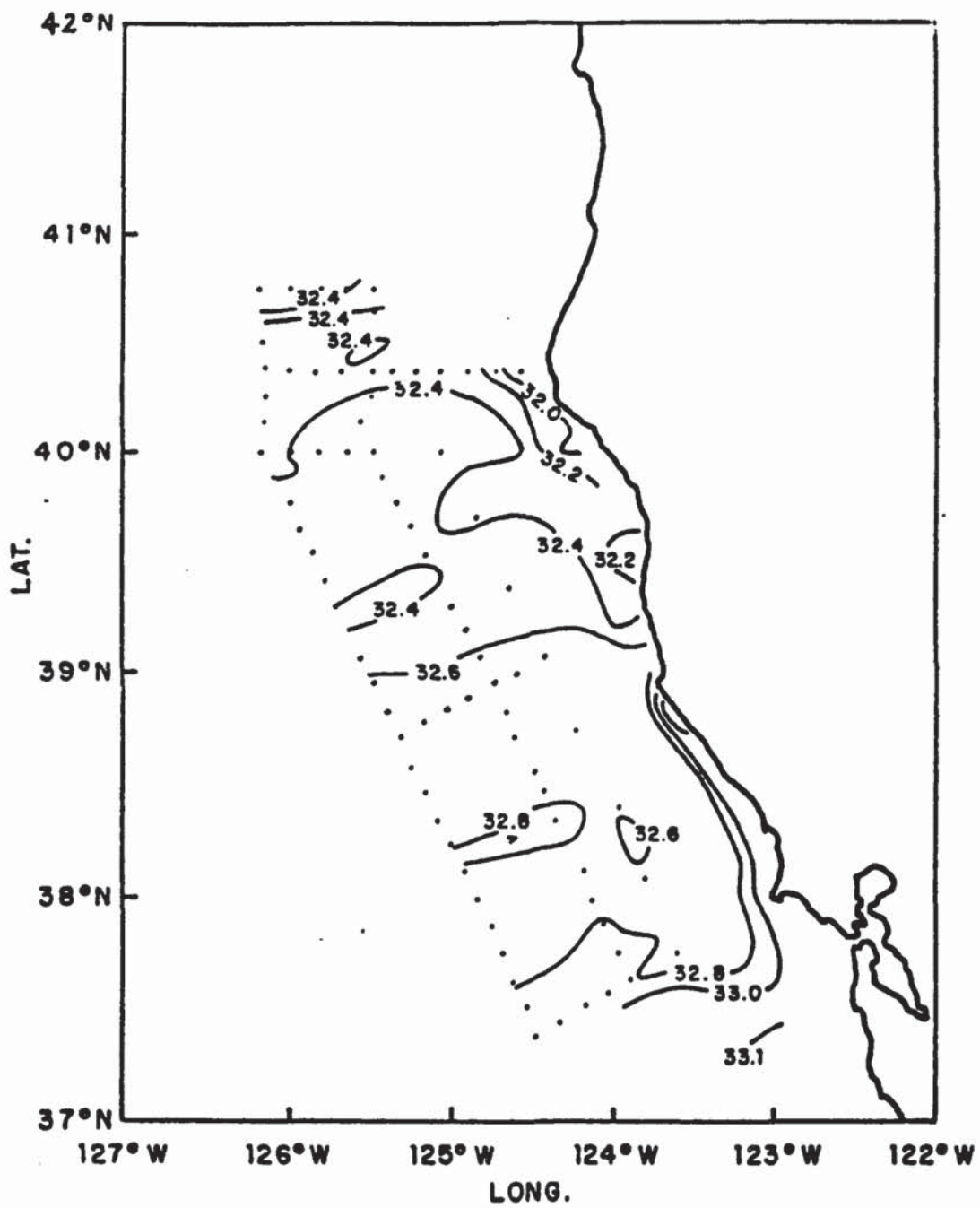
Figure 2.6. Map of surface salinity during Cruise CTZ1, March 17-26, 1987.

20
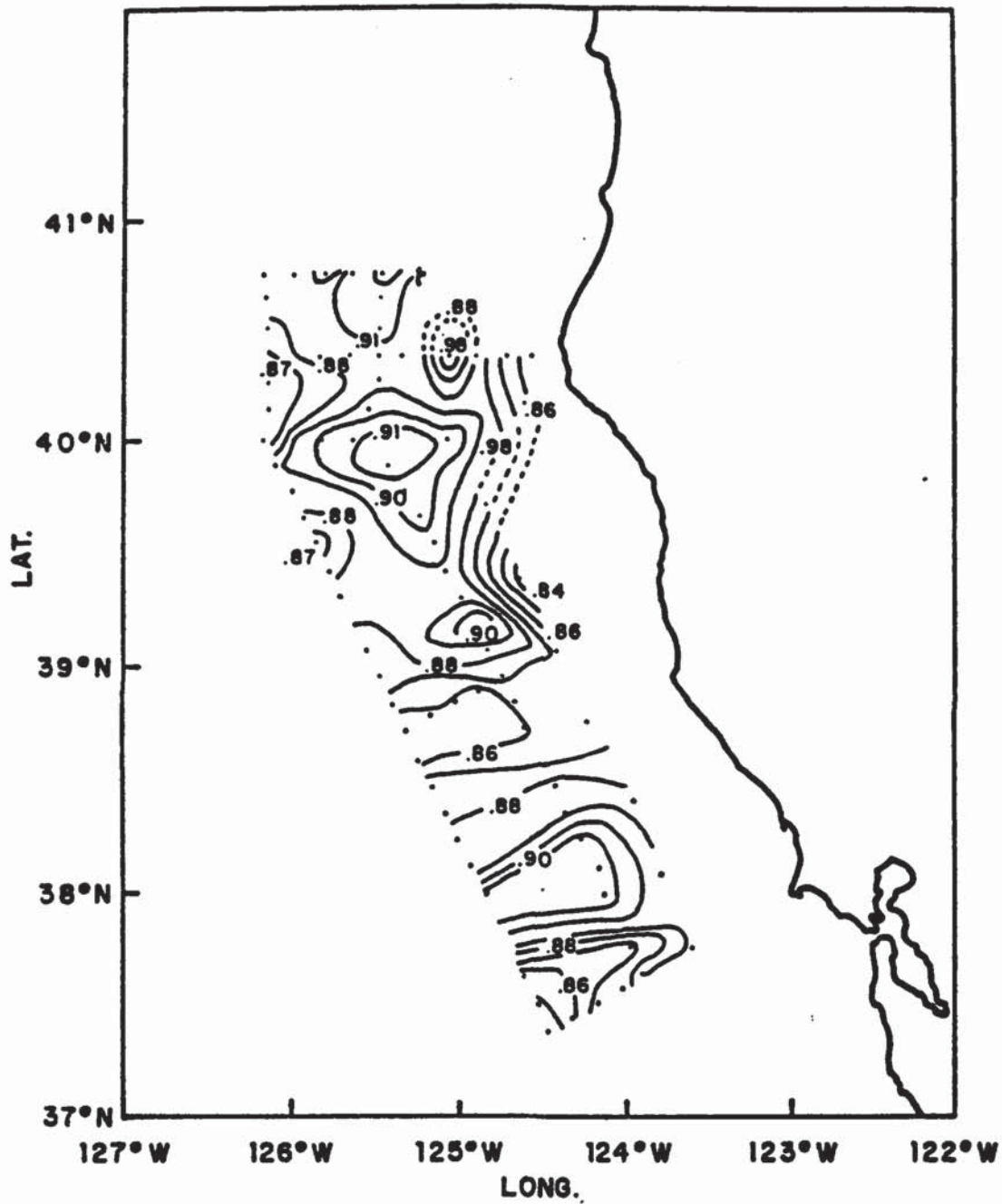
Figure 2.7. Dynamic height at the surface relative to 500 dB during Cruise CTZ1 in March 1987. (Jessen et al., 1989)

21

Rosemount 100-ohm platinum resistance thermometer for the sea surface skin temperature, a Young anemometer for the wind speed and direction, and a General Eastern dewpoint sensor for the air and dewpoint temperatures. The underway data was acquired on an HP9816 computer and recorded on 3.5 inch diskettes. Like the CTD data, the underway data was transferred to a nine track tape upon return and processed on the IBM mainframe. The temperature, conductivity, and pressure sensors on the CTD and the temperature and conductivity sensors of the underway sampling system were calibrated shortly before the cruise. The pressure calibration was carried out using a Chandler Engineering dead weight tester as a standard. The temperature calibration was done using a Seabird temperature sensor as a standard. The conductivity calibration was carried out using a Guildline Model 8400 Autosal as a standard.

A total of 61 water samples were taken at 8 CTD stations for post-cruise calibration. The pressure, conductivity and temperature were noted as each sample was taken. These numbers, after applying the pre-cruise calibration coefficients, were used to calculate salinity and the results compared with the water sample salinities calculated using the Guildline Model 8400 Autosal in the laboratory.

4. Data Processing

After the raw CTD data was transferred to the IBM 3033 mainframe computer at the Naval Postgraduate School, temperature and conductivity corrections were applied to produce profiles of corrected pressure, temperature, and conductivity. Salinity was calculated from these corrected values according to the algorithm of Lewis and Perkin

(1981). Severe spiking due to system malfunctions was eliminated from the salinity signal with a search for vertical salinity gradients greater than 1.0 PSU/m. Points that were determined to be bad were replaced by the values computed from the linear interpolation. Time lag spikes were eliminated by discarding salinity data in regions where the vertical temperature gradient exceeded $0.2°$ C/m and replacing the discarded data with linearly interpolated values. Finally, the data was averaged within 1 m intervals and visually examined for any remaining outlier missed during processing. If found, these points were replaced with linearly interpolated values (Jessen et al., 1989).

III. C-VECTOR METHOD

As mentioned before, ocean currents are the result of the combined effects of thermohaline motion and of wind-driven motion. In both cases, the induced motion usually continues far beyond the place where it was initiated. It should be appreciated that while the wind primarily causes horizontal motion, there may also be vertical motion such as the upwelling and downwelling both in the open ocean and near the coast. Similarly, while the thermohaline effects primarily give rising and sinking motions (vertical), then by the continuity, horizontal motion will be induced (inflow or outflow).

Hydrographic data of coastal oceans were traditionally used to determine dynamical features in only two fields: dynamic topography relative to a certain depth, and geostrophic currents by assuming a certain level of no motion. Some information is lost when using these methods.

In reality, the ocean flow is not in absolute geostrophic balance. It contains two types of circulations, the geostrophic current and the ageostrophic current. The former is obtained from the hydrographic data sets with the usual technique (geostrophic balance), and the ageostrophic current is induced by the presence of the geostrophic flow and surface winds. Hence, the three-dimensional circulation which is both geostrophic and ageostrophic can also be calculated by the hydrographic and surface wind data sets (Chu, 1992).

24

In regions where the temperature and salinity gradients are strong, the usual procedure to calculate only geostrophic currents gives possible serious errors.

To determine the three dimensional flow, a new "tool" is presented since neither the geostrophic current nor dynamical height can supply enough information about the three-dimensional flow field for the coastal currents.

A.   BASIC THEORIES

In Meteorology many papers were published for diagnosing the vertical motions in the atmosphere. One of them is the Q-vector method. Based on the "Quasigeostrophic Theory," the quasigeostrophic ω equation was first presented by Eliassen (1962) and Hoskins (1978). To fill gaps in Hoskins's theory, Xu (1992) proposed a C-vector concept for the atmospheric mesoscale moist frontogenesis. The C-vector concept has been adapted to physical oceanography (Chu, 1992) for diagnosing three-dimensional ageostrophic flow fields. The geostrophic currents (U_g, V_g) are computed as,

$$f\frac{\partial U_g}{\partial z} = \frac{g}{\rho_0}\frac{\partial \rho}{\partial y} = -\frac{\partial b}{\partial y} \qquad (3.1a)$$

$$f\frac{\partial V_g}{\partial z} = -\frac{g}{\rho_0}\frac{\partial \rho}{\partial x} = \frac{\partial b}{\partial x} \qquad (3.1b)$$

where ρ_0 is the characteristic sea water density, ρ is the density deviation from ρ_0, $\rho_0 + \rho$ is the observed density field, and $b = -g\rho/\rho_0$ is the buoyancy force.

25

However, these geostrophic currents are not the complete currents. The basic equations for the complete three dimensional currents are:

$$\left(\frac{\partial}{\partial t} + \vec{V}\cdot\nabla\right)u - f(v - V_g) = \frac{\partial Y^x}{\partial z} \tag{3.2a}$$

$$\left(\frac{\partial}{\partial t} + \vec{V}\cdot\nabla\right)v + f(u - U_g) = \frac{\partial Y^y}{\partial z} \tag{3.2b}$$

$$\left(\frac{\partial}{\partial t} + \vec{V}\cdot\nabla\right)b + N^2 w = 0 \tag{3.2c}$$

$$\frac{\partial u}{\partial x} + \frac{\partial v}{\partial y} + \frac{\partial w}{\partial z} = 0 \tag{3.2d}$$

where ∇, $\vec{v} = (u,v,w)$, f is the Coriolis parameter, N is the Brunt-Vaisala frequency, and (Y^x, Y^y): turbulent momentum flux caused by the surface wind stress (τ^x, τ^y). The three-dimensional flow (V) can be broken down into geostrophic (V_g) and ageostrophic (V_a) components.

$$Y^x\big|_{z=0} = \frac{\tau^x}{\rho_0} \quad , \quad Y^y\big|_{z=0} = \frac{\tau^y}{\rho_0} \tag{3.3}$$

$$\vec{V} = \vec{V}_g + \vec{V}_a \tag{3.4}$$

Then, after the decomposition, the equations (3.2a)-(3.2d) (basic equations) should

26

have the following structure:

$$\mathcal{B}(\vec{V}_a) = \mathcal{R}(\vec{V}_g, \rho, Y^x, Y^y) \tag{3.5}$$

where $\mathcal{B}$, $\mathcal{R}$ are differential operators.

Thus, we can use this equation (3.5) with the hydrographic data ($\underline{Y}$, ρ) and surface wind data, to calculate the three-dimensional ageostrophic circulation, if the real forms of these operators are acquired.

B. QUASI-GEOSTROPHIC SYSTEM

In the quasi-geostrophic system, we have

$$\frac{\partial}{\partial t} + \vec{V} \cdot \nabla = \frac{\partial}{\partial t} + \vec{V}_g \cdot \nabla \tag{3.6}$$

The basic equations for the coastal water (3.2a)- (3.2d) on an f-plane become

$$-fv_a = \frac{\partial Y^x}{\partial z} - (\frac{\partial}{\partial t} + \vec{V}_g \cdot \nabla) U_g \tag{3.7a}$$

$$fu_a = \frac{\partial Y^y}{\partial z} - (\frac{\partial}{\partial t} + \vec{V}_g \cdot \nabla) V_g \tag{3.7b}$$

$$N^2 w_a = - (\frac{\partial}{\partial t} + \vec{V}_g \cdot \nabla) b \tag{3.7c}$$

$$\frac{\partial u_a}{\partial x} + \frac{\partial v_a}{\partial y} + \frac{\partial w_a}{\partial z} = 0 \tag{3.7d}$$

27
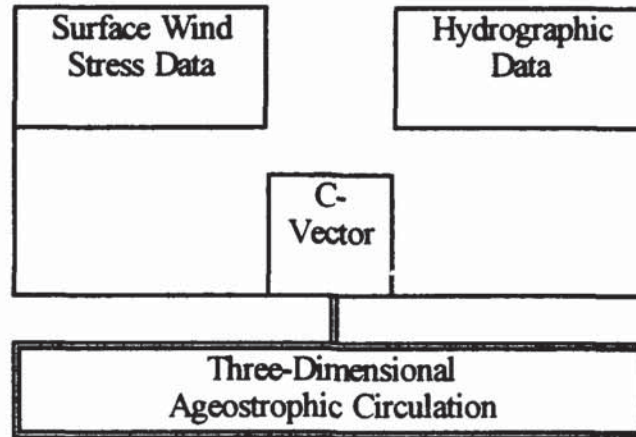
Figure 3.1. Schematic diagram for the computation of ageostrophic circulation(Chu, 1992).

Applying the cross-derivative technique on the ageostrophic pseudo-vorticity equations,

$$-\frac{\partial}{\partial z}\,(f^2 v_a) \;+\; \frac{\partial}{\partial y}\,(N^2 w_a) \;=\; 2C_1 \qquad\qquad (3.8a)$$

$$\frac{\partial}{\partial z}\,(f^2 u_a) \;-\; \frac{\partial}{\partial x}\,(N^2 w_a) \;=\; 2C_2 \qquad\qquad (3.8b)$$

$$\frac{\partial}{\partial x}\,(f^2 v_a) \;-\; \frac{\partial}{\partial y}\,(f^2 u_a) \;=\; 2C_3 \qquad\qquad (3.8c)$$

Rearranging these equations, we get the components of the C-Vector,

$$C_1 \equiv -f\,\Big(\frac{\partial U_g}{\partial y}\frac{\partial V_g}{\partial z} - \frac{\partial V_g}{\partial y}\frac{\partial U_g}{\partial z}\Big) + \frac{f}{2}\frac{\partial^2 Y^x}{\partial z^2} \qquad\qquad (3.9a)$$

28

$$C_2 \equiv -f \left(\frac{\partial U_g}{\partial z} \frac{\partial V_g}{\partial x} - \frac{\partial V_g}{\partial z} \frac{\partial U_g}{\partial x} \right) + \frac{f}{2} \frac{\partial^2 Y^y}{\partial z^2} \qquad (3.9b)$$

$$C_3 \equiv -f \left(\frac{\partial U_g}{\partial x} \frac{\partial V_g}{\partial y} - \frac{\partial V_g}{\partial x} \frac{\partial U_g}{\partial y} \right) - \frac{f}{2} \frac{\partial}{\partial z} \left(\frac{\partial Y^x}{\partial x} + \frac{\partial Y^y}{\partial y} \right) \qquad (3.9c)$$

Clearly we can see that the C-Vector, $C = (C_1, C_2, C_3)$, is computed from the geostrophic currents (U_g, V_g) (obtained from the hydrographic data set), and the wind data (Y^x, Y^y).

Figure 3.1 shows the diagnostic model for the three-dimensional ageostrophic circulation.

C. PHYSICAL MEANING OF C-VECTOR

1. Ageostrophic Vortex Line

The following nondimensional form for flows with f (coriolis parameter) and N (Brunt-Vaisala frequency) as constants, gives the mathematical connection between the C-vector and the ageostrophic pseudo vorticity equations (3.7a-c).

$$\nabla \times \vec{V}_a = 2 R_0 \vec{C} \qquad (3.10)$$

$$\nabla \cdot \vec{V}_a = 0 \qquad (3.11)$$

$R_0 \equiv U/(fL)$ is the Rossby number and $H/L = W/U = f/N$ is chosen for the scaling where H is the charactistic vertical length, L is the characteristic horizontal length, W is the characteristic vertical velocity, and U is the characteristic horizontal velocity.

Since the ageostrophic vorticity is proportional to the C-vector, a C-vector

29

streamline can be viewed as an ageostrophic vortex line (Figure 3.2).
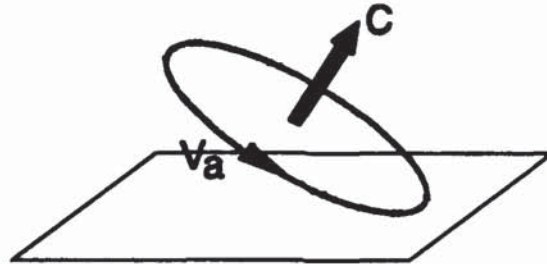
Figure 3.2. Ageostrophic circulation induced by C-Vector in three-dimensional space (Xu, 1992).

2. **Vertical Motion Induced by the Vertical Vorticity of C-Vector**

The vertical velocity equation is obtained from

$$\nabla^2 w_a = -2R_0\, \vec{k}\cdot\nabla\times\vec{C} \qquad\qquad (3.12)$$

which indicates that the vertical velocity is caused by the vertical vorticity of the C-Vector (Figure 3.3.).

3. **Nondivergence of C-Vector**

To have nondivergence, the horizontal divergence (convergence) should be balanced by the vertical convergence (divergence), the summation of differentiations of (3.9a) with respect to x, of (3.9b) with respect to y, and of (3.9c) with respect to z, leads

30
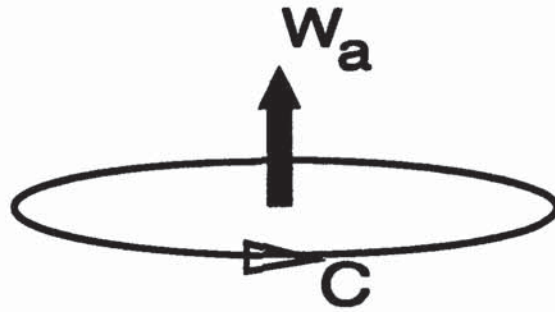
Figure 3.3. The vertical vorticity W_a induced by horizontal rotation (vorticity) of C-Vector (Xu, 1992).

to

$$\nabla \cdot \vec{C} = 0 \qquad (3.13)$$

which demonstrates that the C-vector is nondivergent. Additionally, (3.8c) shows that the vertical vorticity of the ageostrophic flow can be deduced from the vertical component of the C-vector (Figure 3.4)

Figure 3.4. The vertical vorticity of ageostrophic flow is inferred from the vertical component of the C-Vector (Xu, 1992).
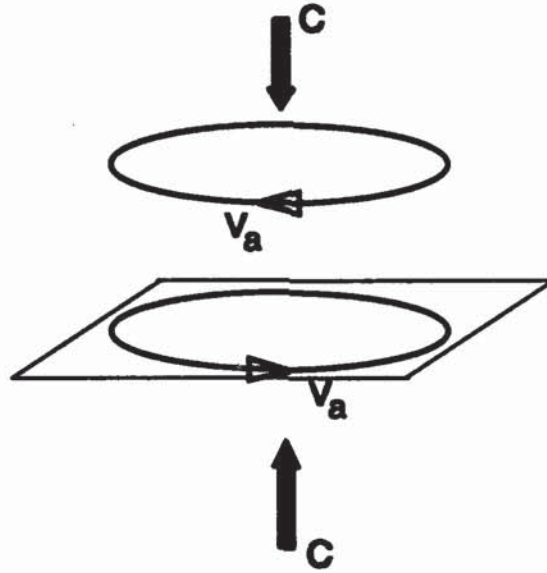
D.   Ψ Function

As defined before in equation 3.12 there is a direct relation between the vertical velocity and the vertical vorticity of the C-vector, which it can be rewritten as:

$$\nabla^2 w_a = -2R_0\, \Psi \tag{3.14}$$

where

$$\Psi = \vec{k}\cdot\nabla\times\vec{C} \tag{3.15}$$

This Ψ function is very important in the determination of the vertical motion of the flow because both should have the same sign i.e., if Ψ is positive it will have upward motion, a downward motion when Ψ was negative.

32

E. C'-Vector

The C'-Vector defined in the following relation as:

$C' \equiv$ C-VECTOR + 3-DIMENSIONAL GEOSTROPHIC VORTICITY

$C' \equiv (C_x, C_y, C_z)$

It is also derived from the C-vector to give:

$$C_x \equiv \frac{C_1}{f^2} - \frac{\partial v_g}{\partial z} \qquad (3.16a)$$

$$C_y \equiv \frac{C_2}{f^2} + \frac{1}{2} \frac{\partial u_g}{\partial y} \qquad (3.16b)$$

$$C_z \equiv \frac{C_3}{f^2} + \frac{1}{2} \left(\frac{\partial v_g}{\partial x} - \frac{\partial u_g}{\partial y} \right) \qquad (3.16c)$$

This means that this vector $C' \equiv (C_x, C_y, C_z)$, is another and very useful way to determine the 3-dimensional vorticity for the total flow.

IV. THREE DIMENSIONAL PSEUDO-VORTICITY FIELD

The averaged data was extracted using the IBM mainframe computer at the Naval Postgraduate School using the fortran program "EXTRACT" written by Paul Jessen. This program extracts data from a file on the mass storage system and writes it to a file on the user's reader disk for easy access.

A.   Interpolation Using The Weighting Function

Since the extracted data was not regularly distributed and evenly spaced, it was necessary to put it in a form that makes future calculations easy. Hence, an interpolation was performed, creating a new distribution of the data on a new grid (figure 4.1). This interpolation was done using the so-called "weighting function" technique.

This technique was developed in order to achieve an optimal interpolation on data that has samples (CTD casts as an example) that are relatively coarsely distributed. This analysis technique was developed by Doswell (1977) and Maddox (1980), who also based it in a Barnes (1964/1973) scheme (filtering properties of the objective analysis). As explained by Tintoré et al. (1991), the Barnes scheme has two analyses. The first one, f_1, defines the macroscale, a low pass filter which smooths the observed data, the second one, f_2, another low pass filter with a cut-off near the smaller resolvable scale, then the mesoscale analysis is defined as the normalized difference between these two low-pass filters (a band-pass filter). Finally, the total field is obtained with the sum of these two scales (macroscale and mesoscale). At the same time, each analysis consists of two steps

34

explained using the following formulas.

　　a.　*First Step*

$$f^0(i,j) = \frac{\displaystyle\sum_{n=1}^{N} W_n(i,j)\, f_n}{\displaystyle\sum_{n=1}^{N} W_n(i,j)} \qquad\qquad (4.1)$$

and

$$W_n(i,j) = \exp\left[\frac{-d_n(i,j)^2}{4C}\right] \qquad\qquad (4.2)$$

Where $f^0(i,j)$ are grid values initially computed from the total N of data observed; f_n are data observed; $W_n(i,j)$ is a weight function; $d_n(i,j)$ is the separation distance between the grid point (i,j) and the nth station; and C is an analysis parameter.

　　b.　*Second Step "The First Guess"*

$$f(i,j) = f^0(i,j) + \frac{\displaystyle\sum_{n=1}^{N} W_n \cdot (i,j)\, \Delta f_n}{\displaystyle\sum_{n=1}^{N} W_n \cdot (i,j)} \qquad\qquad (4.3)$$

35

$$\Delta f_n = f_n - f_n^0 \qquad\qquad (4.4)$$

$$W_n^\bullet(i,j) = \exp\left[\frac{-d_n(i,j)^2}{4CG}\right] \qquad 0 < G < 1 \quad (4.5)$$

where f_n^0 is the first guess evaluated at each station; and G is another analysis parameter.

The analysis parameters C and G are chosen either as a result of previous knowledge of structures in the field or based upon theoretical constraints such as characteristic scale and deformation radius.

B. Grid Presentation

The extracted data was subdivided into two areas, in order to facilitate the interpolation work.

Area 1 coincides with section A in the planned grid Figure 2.1. It is formed from 27 stations (CTD casts). After performing the interpolation, Area 1 has 49 grid points (x=7,y=7), as shown in Figure 4.1. In this area, the X-axis is zonal (positive eastward), and Y-axis is meridial (positive northward).

Area 2 is formed with 56 stations corresponding to sections B and C of planned grid Figure 2.1. After the interpolation, Area 2 has 225 grid points (x=9,y=25). For this area the Y-axis coincides with the shoreline direction, and X-axis with the cross-shore. The Z axis is in the vertical direction. The maximum depth in this study is 500m.

36

The vertical resolution is 10m, giving a total of 50 grid points in the Z direction. In summary, Area 1 is formed by (x=7,y=7,z=50), and area 2 by (x=9,y=25,z=50).

C. Geostrophic Velocity

The method to compute the geostrophic velocity was performed on the interpolated data (grid point). This method was written based on the *thermal wind equation* where the horizontal density differences between the stations are used to compute the baroclinic shear (assuming a level of no motion of 500 m). Then the shear is vertically integrated to give the geostrophic velocity relative to 500 m.

To explain this method better we will assume we want to calculate the geostrophic velocity between stations A and B, with density profiles $\rho_a(z)$ and $\rho_b(z)$ respectively, following these steps:

a. Compute an average value of the Coriolis parameter, f, for the two stations.

$$f = \frac{f_a + f_b}{2} \qquad (4.6)$$

b. For k = 1 to NPTS-1, compute a horizontal gradient at level k + 1/2

$$\frac{\partial \rho}{\partial x} = \frac{[\rho_b(k) + \rho_b(k+1) - \rho_a(k) - \rho_a(k+1)]}{2\Delta x} \qquad (4.7)$$

where NPTS is the number of grid points in z direction and Δx is the distance between the two stations.

c. Compute the baroclinic shear, from the thermal wind equation

37

$$\frac{\partial v}{\partial z} = -\frac{g}{f\rho_0}\frac{\partial \rho}{\partial x} \qquad (4.8)$$

at level k + 1/2, where g = 9.81 m/s^2 and ρ_0 = 1026 kg/m^3.

d. Assuming a level of no motion at the lowest depth (500m) set V(NPTS) = 0, and then integrate the baroclinic shear upwards in z to compute V at level k.

$$V(k) = V(k+1) + \frac{\partial V}{\partial z}(k)\,[z(k)-z(k+1)] \qquad (4.9)$$

Now the question should be, how do we know if both the interpolated method and the geostrophic computation (based in the thermal wind equation) are correct? The answer is shown by the correspondence found between plots made using the program PLOTSEC, also written by Paul Jessen, for the geostrophic velocity computed by the GEOVEL program (with hydrographic data), and the plots generated by the subroutine CONTOURS for the geostrophic velocity computed using the thermal wind method (interpolated data). Figures 4.2.a-b, 4.3.a-b, 4.4.a-b, 4.5.a-b, 4.6.a-b, show these plots for Area 1, and Figures 4.7.a-b and 4.8.a-b for Area 2.

It is important to note that the boundaries of the plots do not coincide exactly since one is for real station positions, and the other is the grid position. Another important note is that the grid points are evenly spaced and perfectly aligned, but the stations are neither evenly spaced nor perfectly aligned. Despite these differences, they show a good correlation.

D. Wind Stress

The bulk equation that relates the stress τ to the wind speed u has the form

$$\tau = C_D \rho u^2 \qquad (4.10)$$

where C_D is the *drag coefficient* (dimensionless) and depends on the roughness of the surface.

The drag coefficient C_D for the ocean increases with the wind speed, and it was calculated for the California Current System from Large and Pond (1981) using

$$C_D = 1.14x10^{-3} \qquad (4.11)$$

for $u < 10$ m/s and

$$10^{-3}C_D = 0.49 + 0.065u \qquad (4.12)$$

for $u > 10$ m/s.

Noting that the wind stress only affects the upper layers of the ocean, the so-called mixed-layer depth (ML) for this study was based on the data and 65m was assumed. Furthermore, it was assumed that the wind stress is maximum at the ocean surface, decaying linearly to zero at the base of the ML.

E. C-Vector

We can now compute the C-vector by applying the equations presented in Chapter III and generate a series of plotted fields for presentation and analysis in the next chapter.
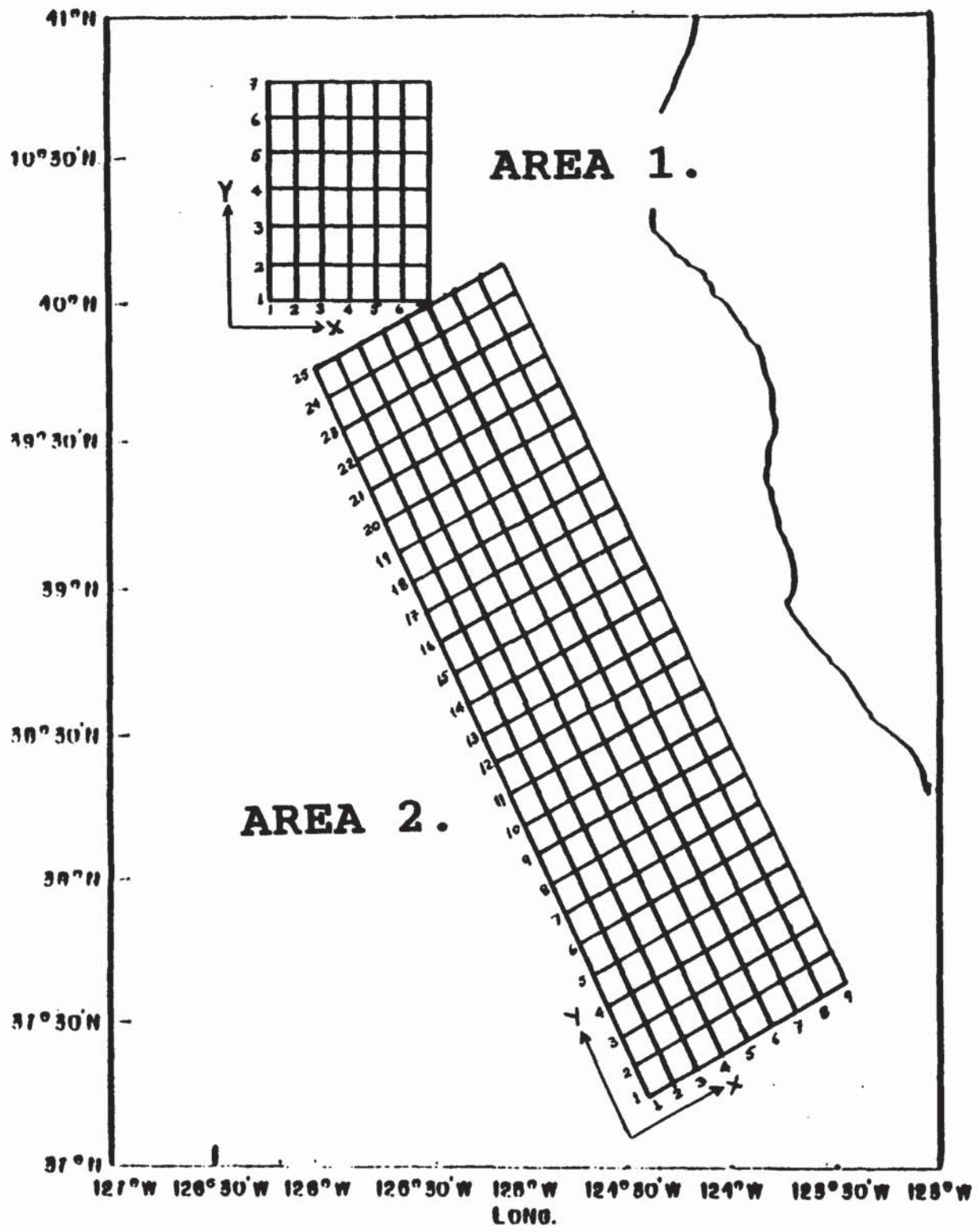
39

Figure 4.1. Final grid distribution of data after interpolation, using the weighting function technique.
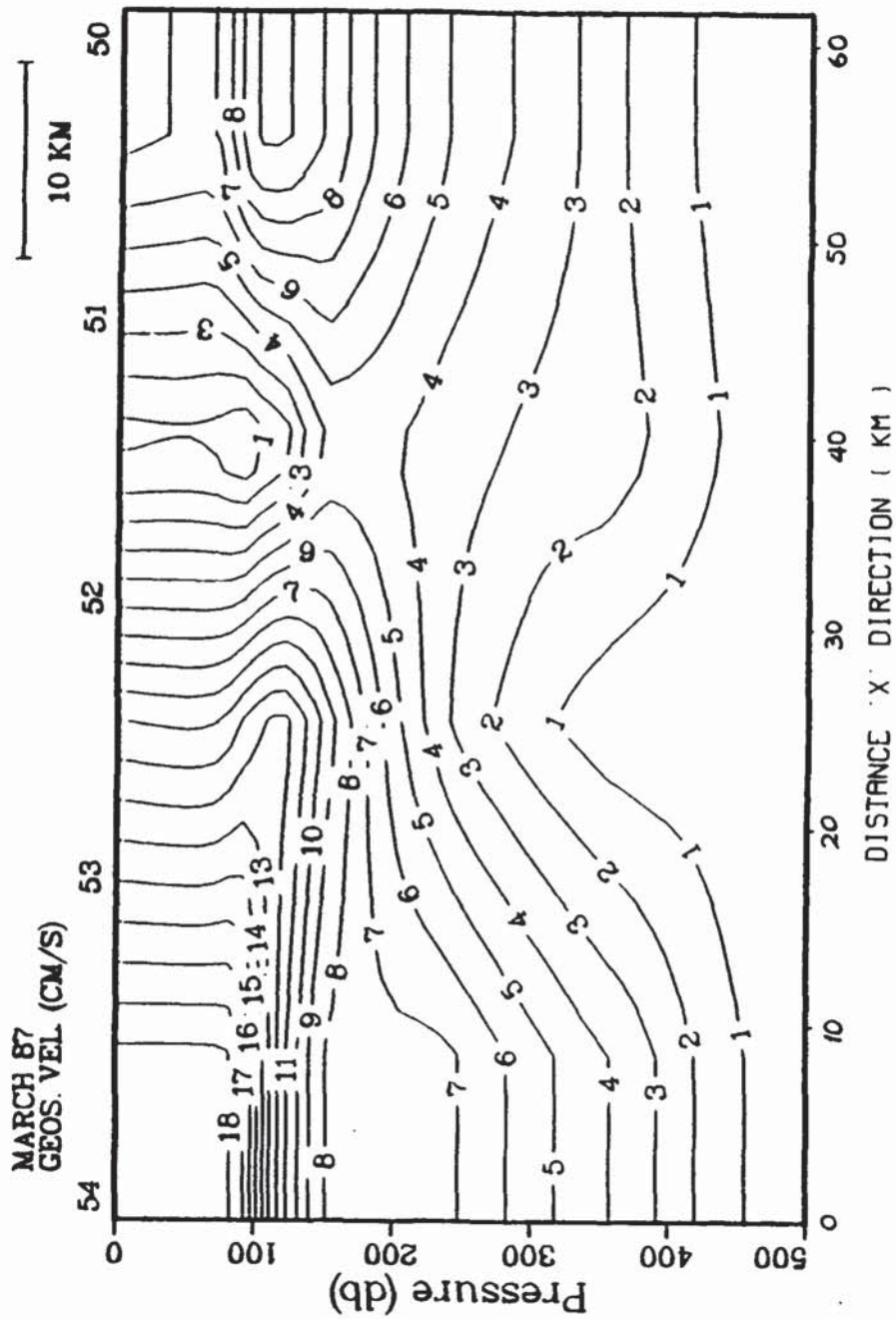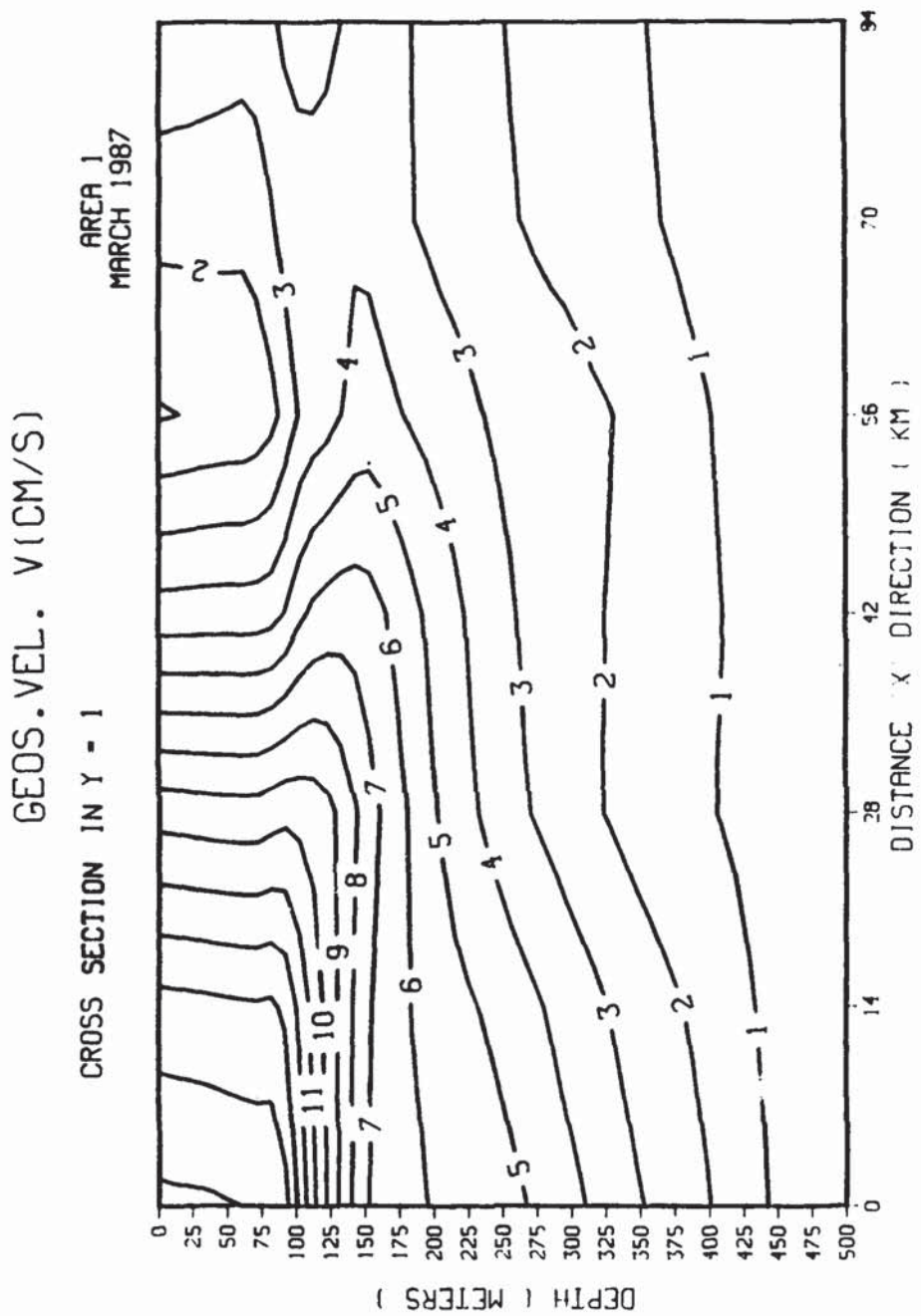
40

Figure 4.2.a. Geostrophic velocity from Area 1, Stations 54-50, computed using GEOVEL with hydrographic data.

41

Figure 4.2.b. Geostrophic velocity from Area 1, Cross-Section y=1, computed using THERMAL WIND method with interpolated data.
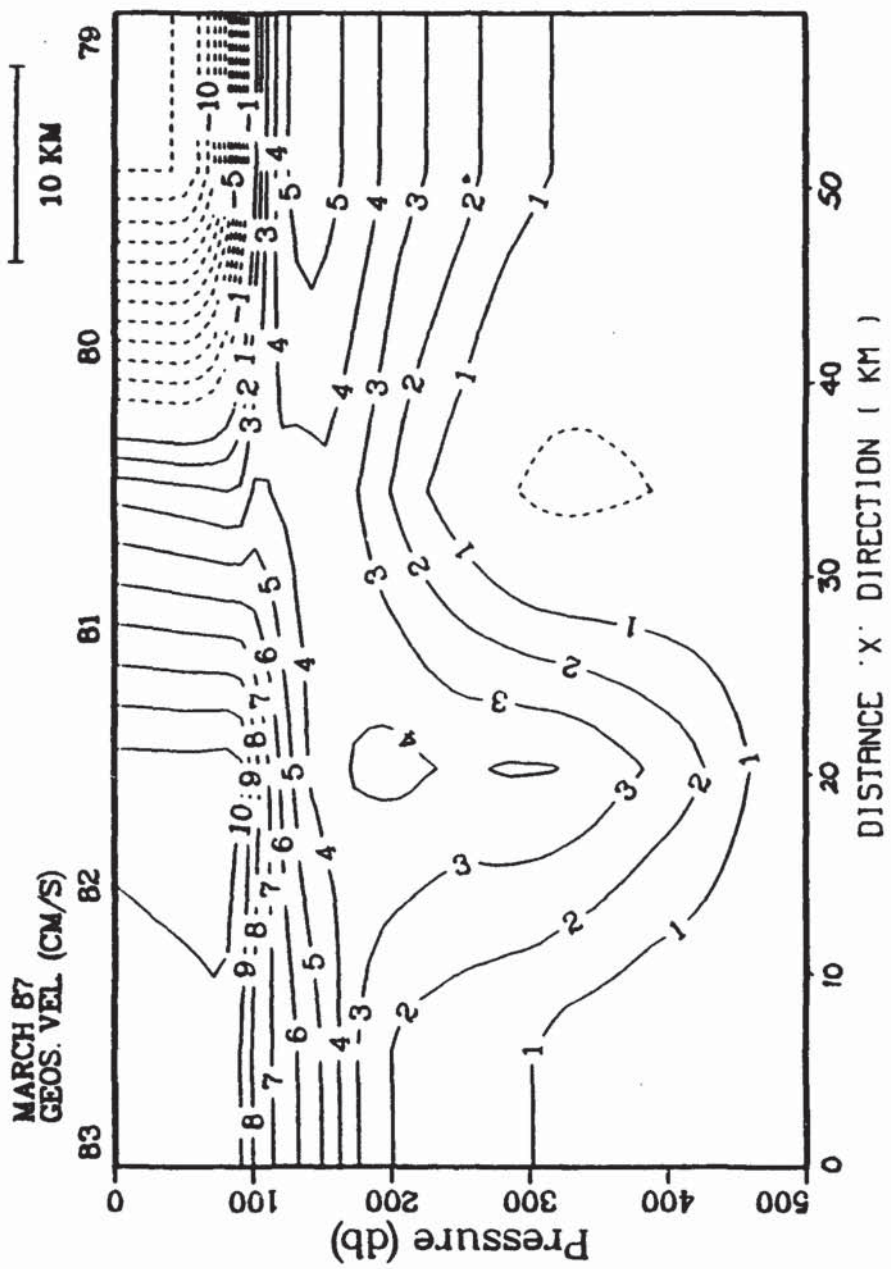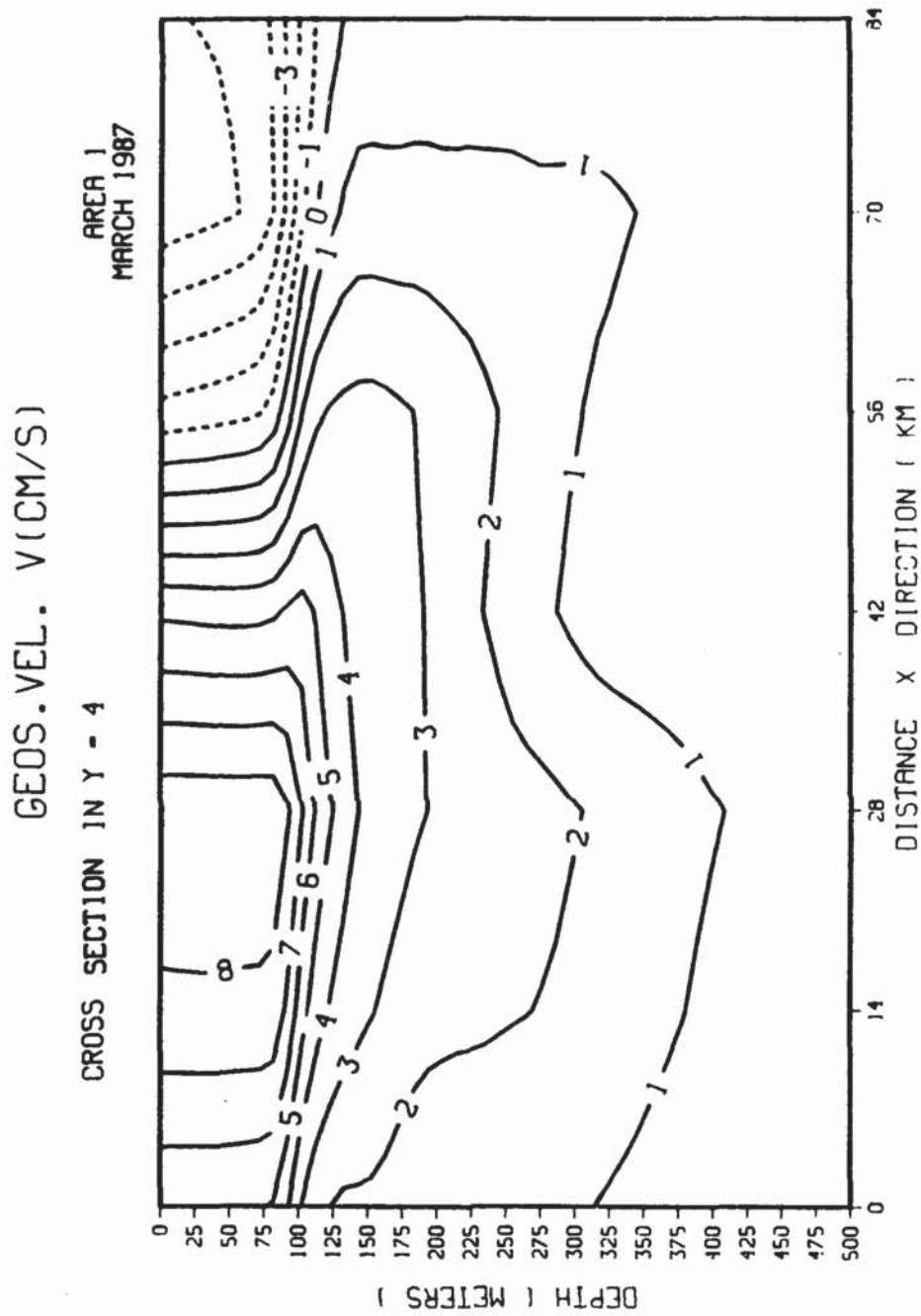
42

Figure 4.3.a. Geostrophic velocity from Area 1, Stations 83-79, computed using GEOVEL with hydrographic data.

Figure 4.3.b. Geostrophic velocity from Cross-Section y=4, Area 1, computed using THERMAL WIND method with interpolated data.
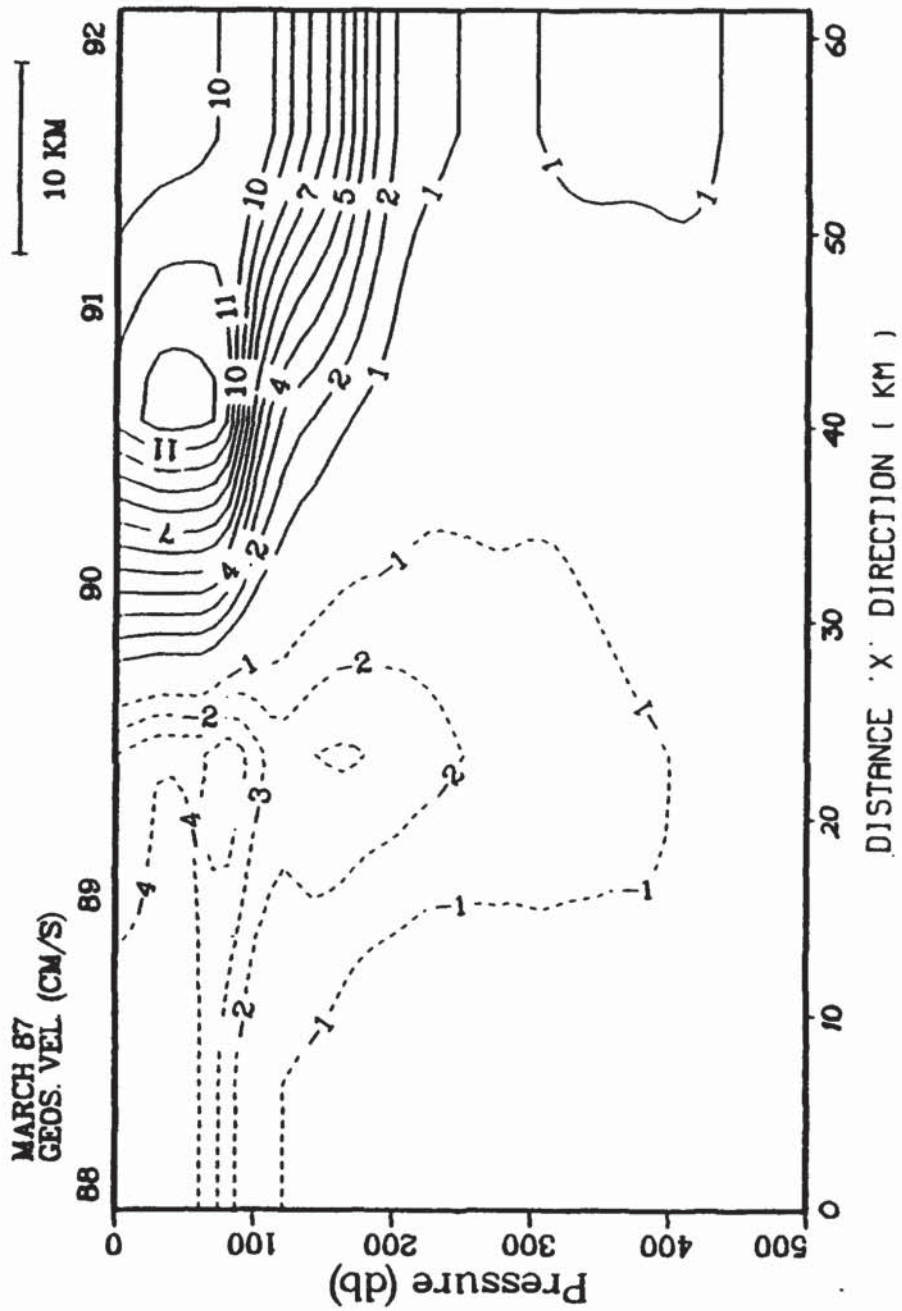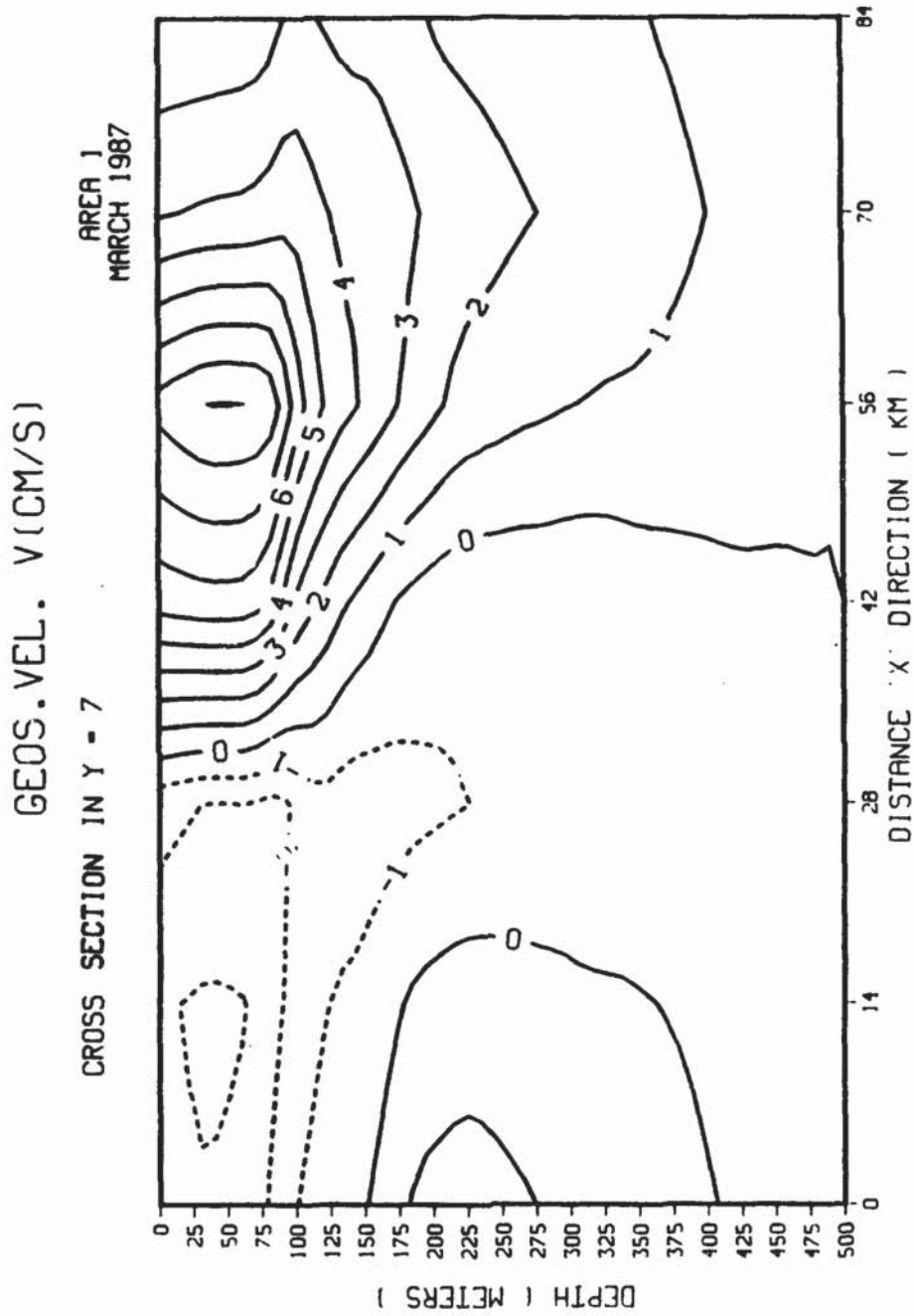
44

Figure 4.4.a. Geostrophic velocity from Area 1, Stations 88-92, computed using GEOVEL with hydrographic data.

45

Figure 4.4.b. Geostrophic velocity from Area 1, Cross-Section y=7, computed using **THERMAL WIND** method with interpolated data.
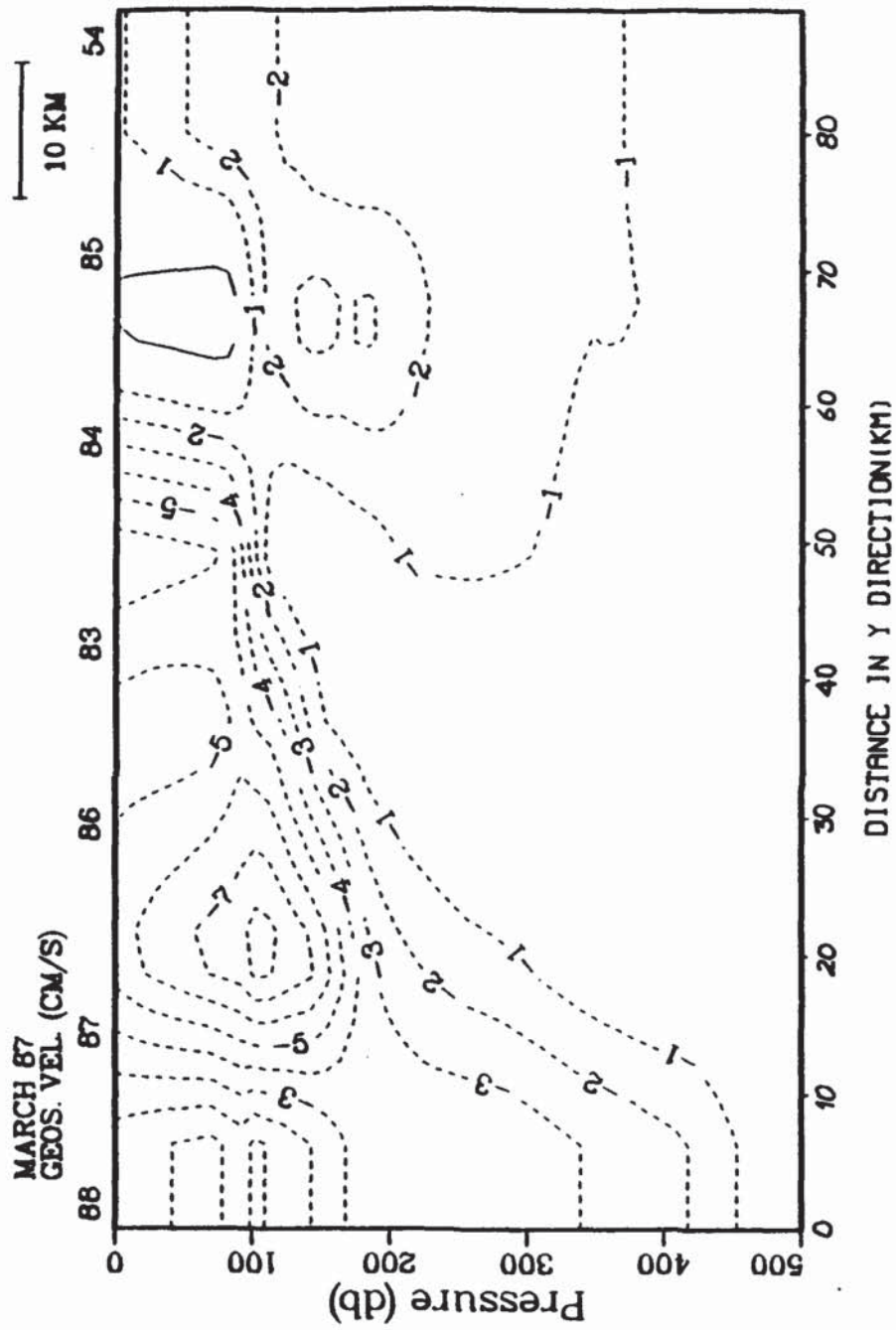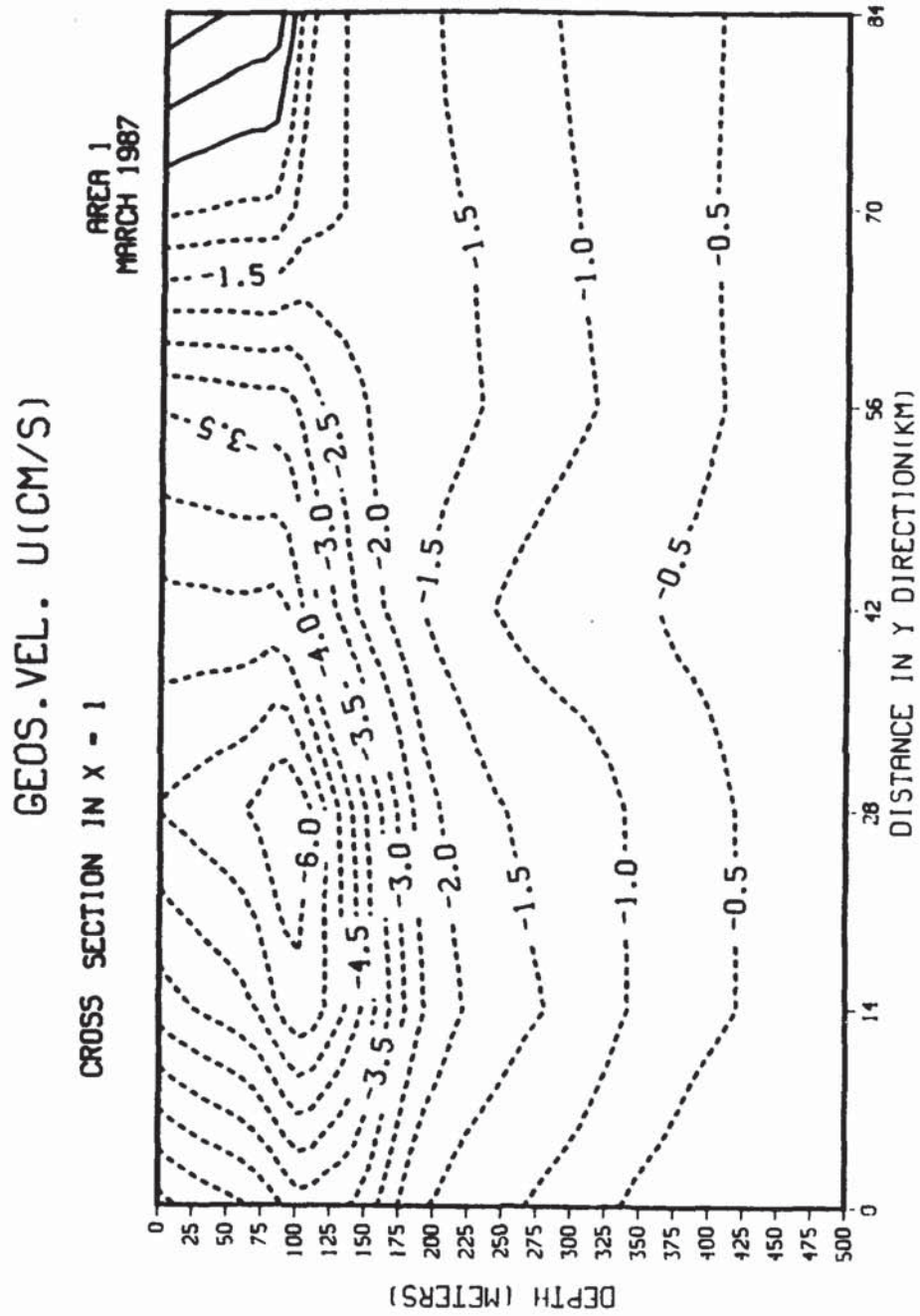
46

Figure 4.5.a. Geostrophic velocity from Area 1, Stations 88-54, computed using GEOVEL with hydrographic data.

47

Figure 4.5.b Geostrophic velocity from Area 1, Cross-Section x=1, computed using THERMAL WIND method with interpolated data.
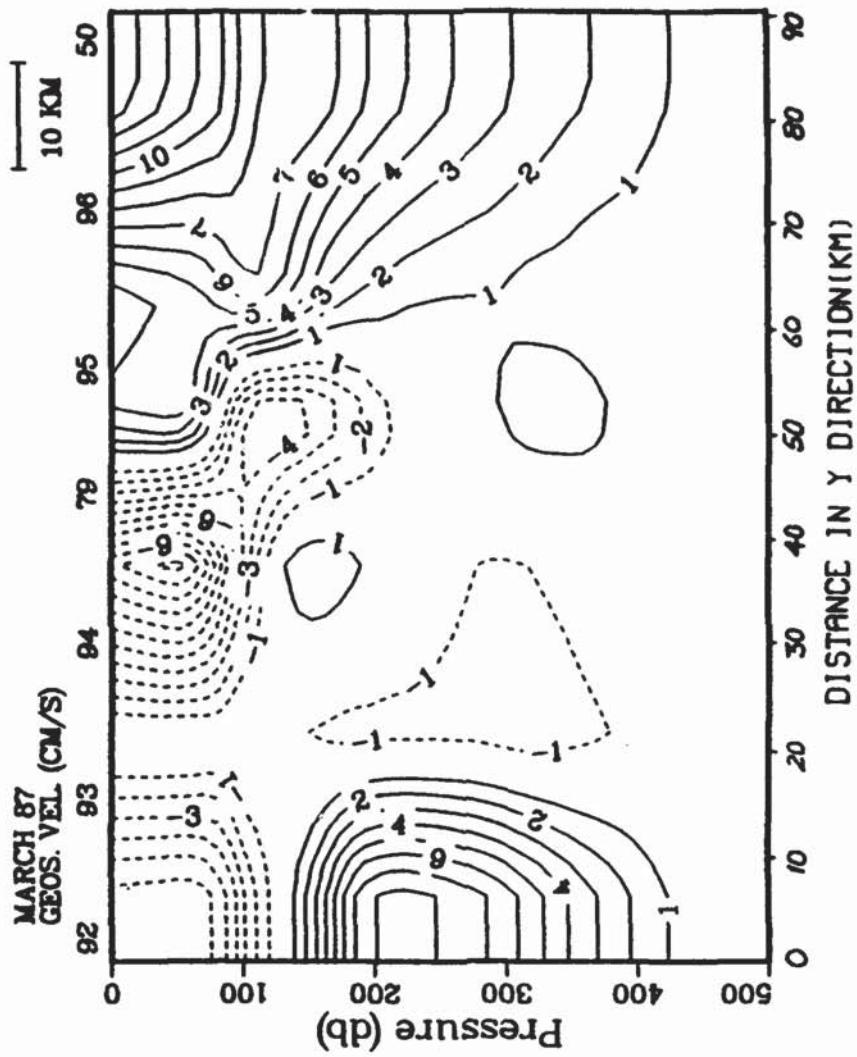
48

Figure 4.6.a. Geostrophic velocity from Area 1, Stations 92-50, computed using GEOVEL with hydrographic data.

49

Figure 4.6.b. Geostrophic velocity from Area 1, Cross-Section x=6, computed using THERMAL WIND method with interpolated data.
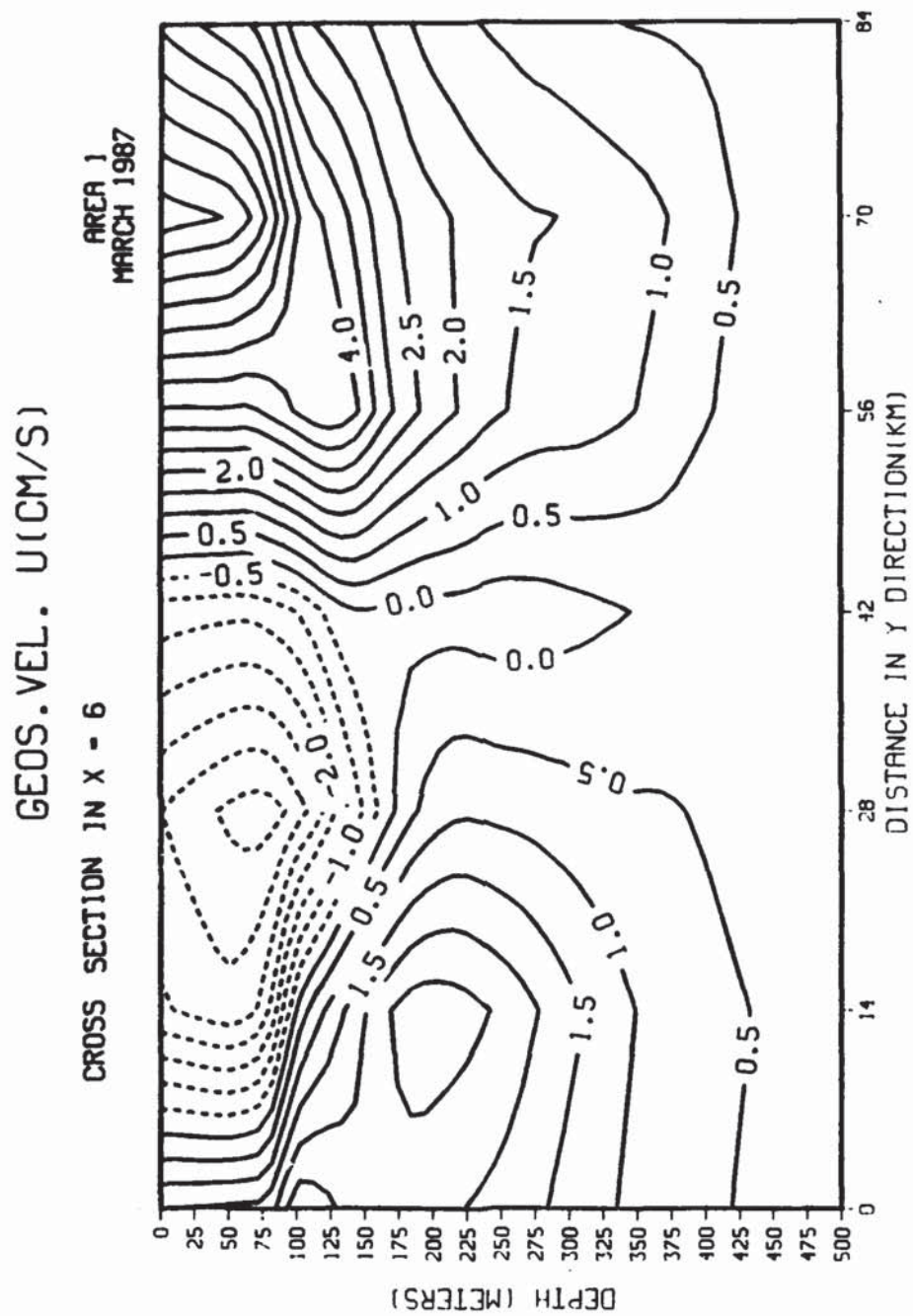
50

Figure 4.7.a. Geostrophic velocity from Area 2, Stations 56-27, computed using GEOVEL with hydrographic data.

51

Figure 4.7.b. Geostrophic velocity from Area 2, Cross-Section x=1, computed using the THERMAL WIND method with interpolated data.

52

Figure 4.8.a. Geostrophic velocity from Area 2, Stations 50-01, computed using GEOVEL with hydrographic data.

Figure 4.8.b. Geostrophic velocity from Area 2, Cross-Section x=6, computed using the THERMAL WIND method with interpolated data.
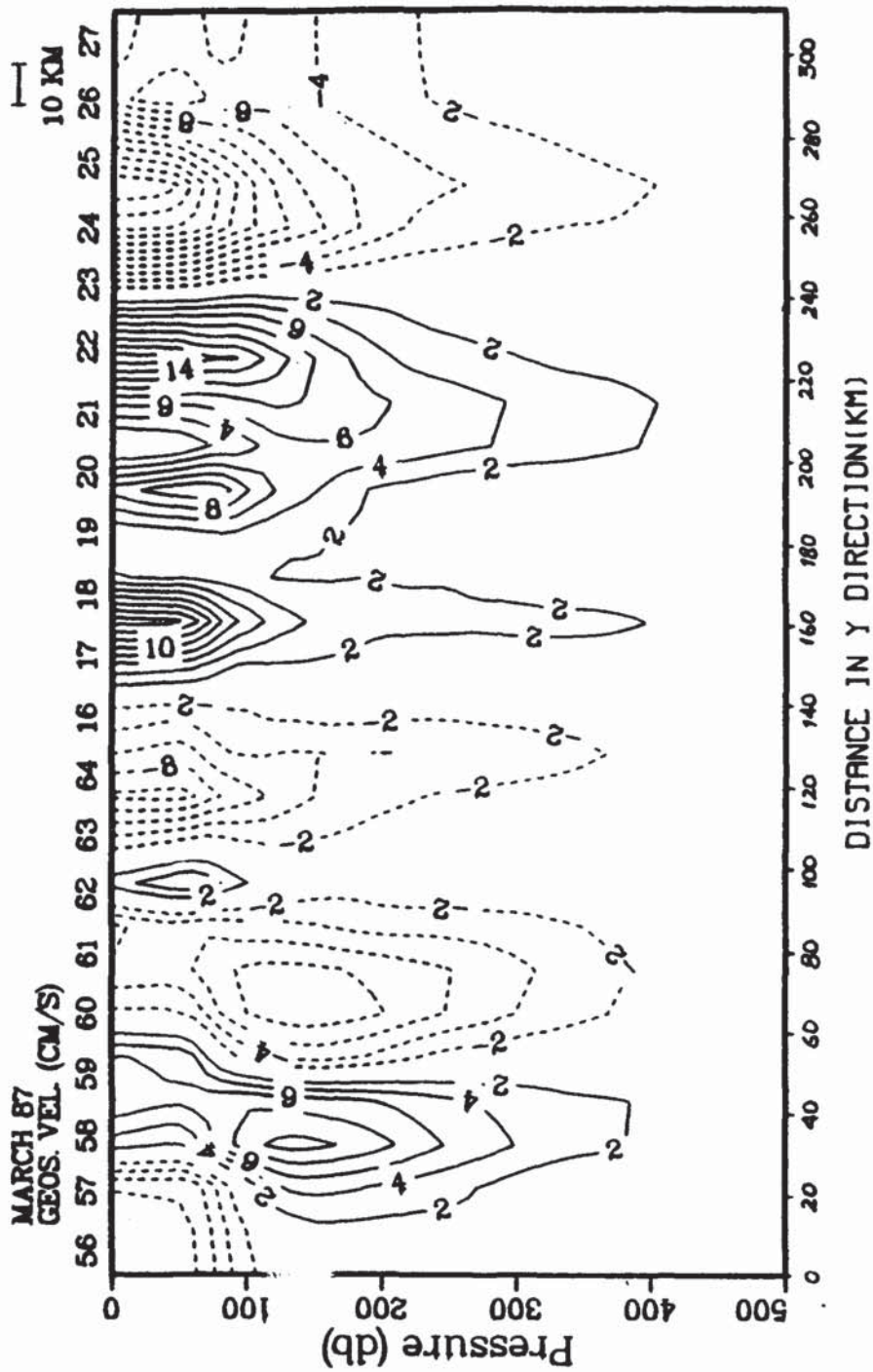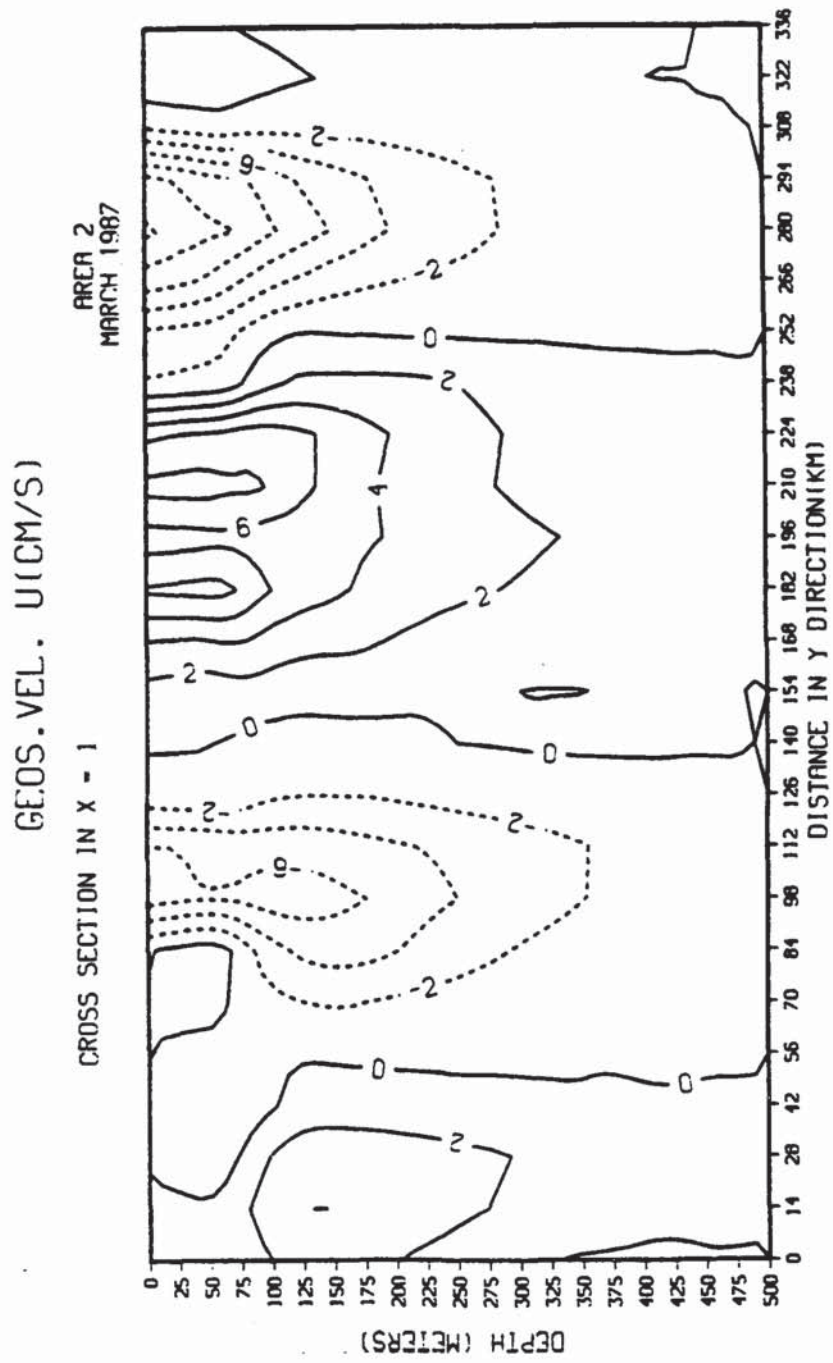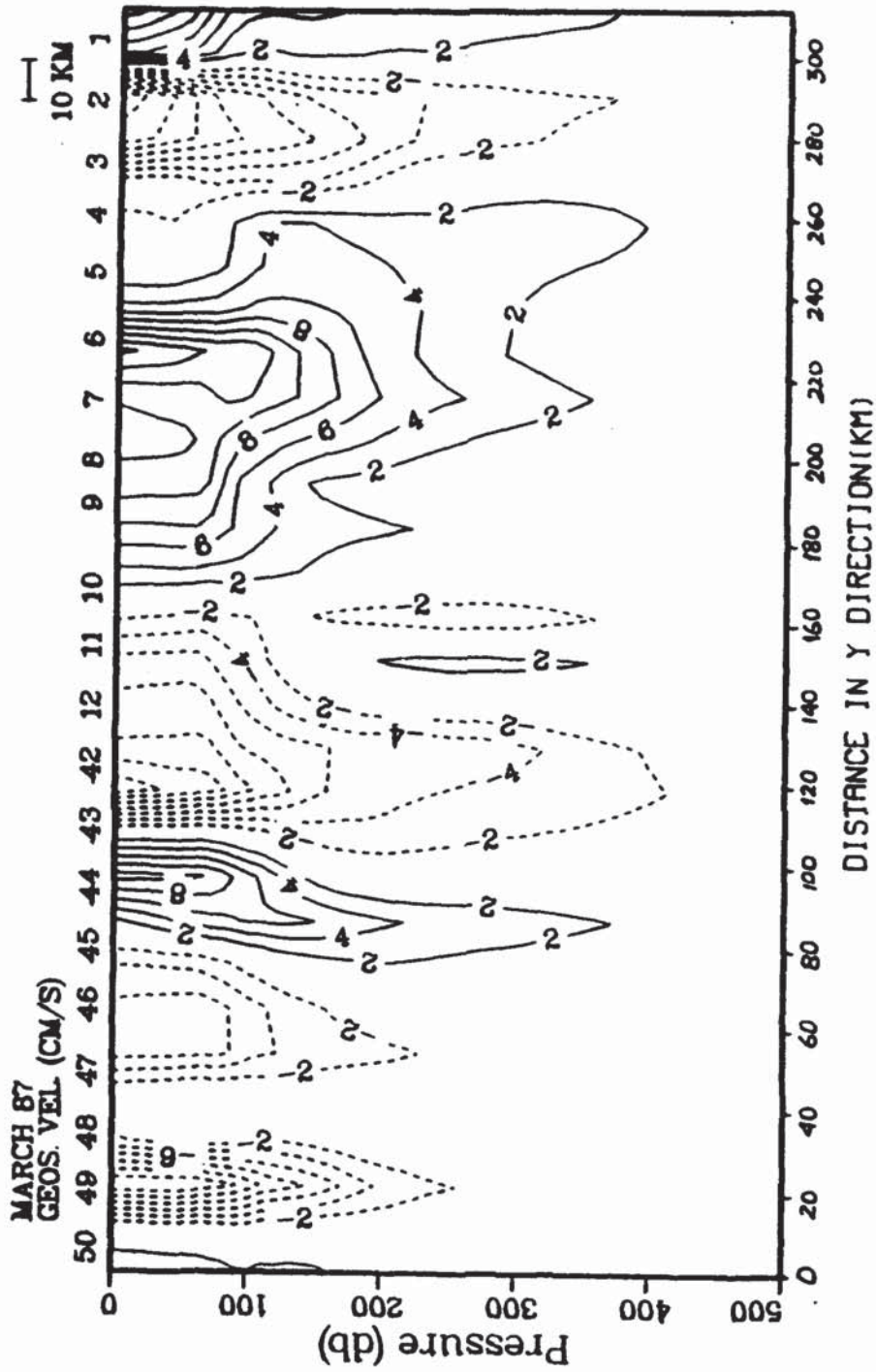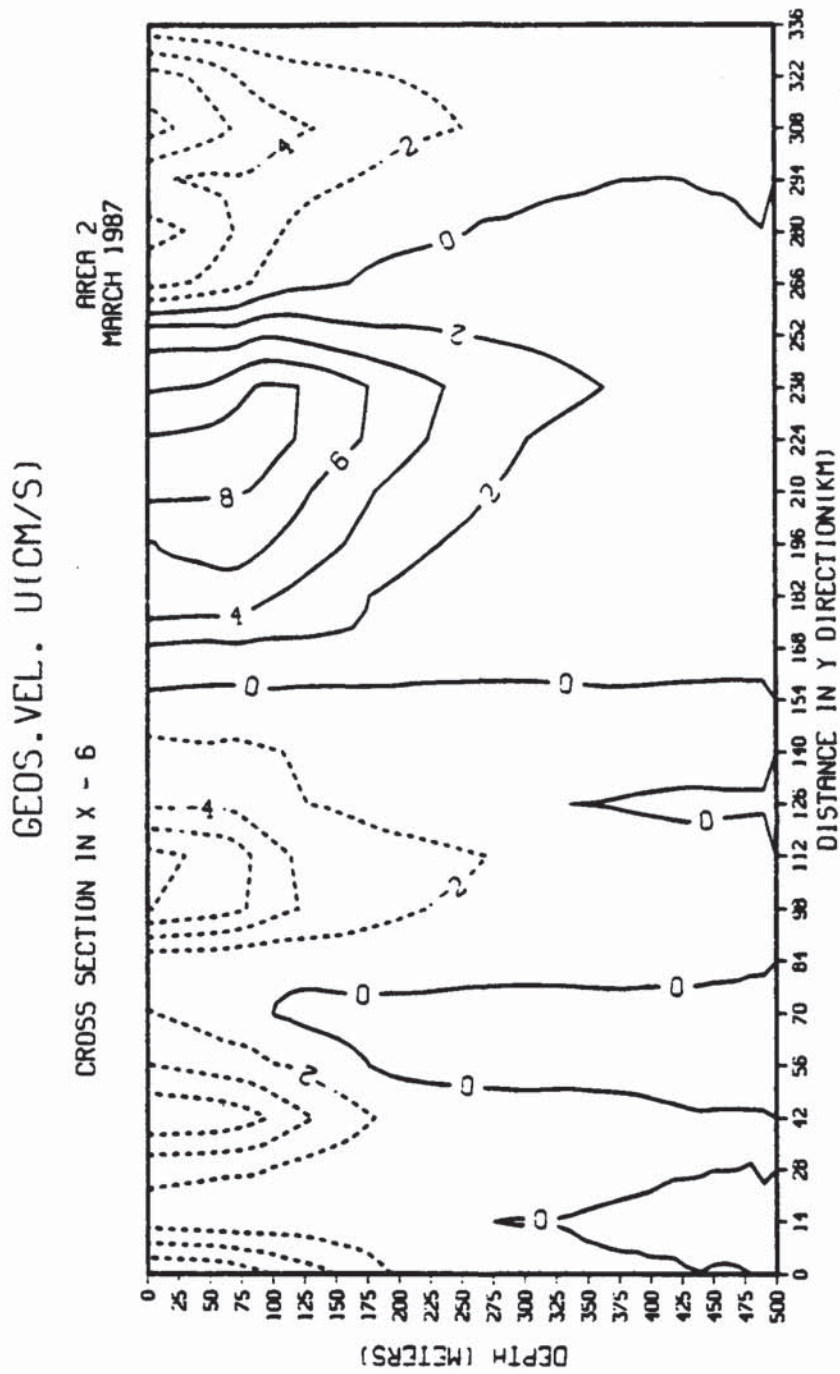
54

V. RESULTS

A. PRESENTATION

1. Pseudo-vorticity Field for the Total Flow

C_x corresponds to the total pseudo-vorticity in the x-direction. There are seven C_x cross-sections in Area-1 (Figures 5.1-5.3) and nine C_x cross-sections in the Area-2 (Figures 5.7-5.9). C_y corresponds to the total pseudo-vorticity in the y-direction. There are seven C_y cross-sections in Area-1 (Figures 5.4-5.6) and twenty five C_y cross-sections in the Area-2 (Figures 5.10-5.15). The depth of all of these cross-sections is 500m, with 10m vertical resolution. The principal characteristics for the analysis are: solid lines for positive and zero pseudo-vorticity (i.e. clock-wise rotation), dashed lines for negative pseudo-vorticity (i.e. counter clock-wise rotation).

2. Ψ Function

The plots of the Ψ function are presented in Figures 5.16-5.18 for Area-1 and in Figures 5.19-5.21 for Area-2. In these horizontal cross-sections the solid lines represent upward motion and the dashed lines downward motion. Zero lines are also represented by solid lines.

B. ANALYSIS

1. Area-1

In all the plots presented for this area significant values of magnitude for ζ, ζ_y and Ψ Function were found from the surface to a depth of 150m, but the level of greatest magnitude seems to be at a depth of 100m.

In Figure 5.17 the Ψ function is plotted at three different depths, 60, 80 and 100m. At the 100m depth, we can see upward motion (solid lines) and downward motion (dashed lines) at sectors listed in Table 5.1.

TABLE 5.1 VERTICAL MOTION FOR Ψ (Area 1)		
X-Coordinates	Y-Coordinates	Vertical Motion
x=1-4	y=1-3	Upward
x=6-7	y=4-7	Upward
x=1-4	y=6-7	Upward
x=1-4	y=4-5	Downward
x=4-7	y=1-3	Downward
x=5	y=6	Downward

This analysis is very similar in that it shows upward motion. Indeed, even in Figure 5.18 the same characteristics are present at the 120m level. Deeper than 120m, the features change, and their intensity decreases and almost disappears at the 160m level. To complete the analysis, each component of the pseudo-vorticity ($\zeta_x\zeta_y$) will be calculated with the Ψ function.

a. C_x and Ψ Function

In Figure 5.1 three vertical cross-sections are presented for C at x=1-3. The pseudo-vorticity field is clearly depicted, positive clock-wise (solid lines) and negative counter clock-wise (dashed lines). The cores of rotation (both positive and negative) are found mainly around the 100m depth. The same depictions are found in Figures 5.2 and 5.3 for C_x and in Figures 5.4-5.6 for C_y. To analyze and compare the pseudo-vorticity fields with the Ψ function, we choose the 100m depth as a base level.

In Figure 5.17 the western boundary that corresponds to x=1 as constant and moves along the y axis from south to north (y=1-7). Compared with Figure 5.1 at x=1 (also at 100m depth), this corresponds to the vertical cross-section of C. As we can see at y=1, a core of positive vorticity is found. Going to the left at y=4 a core of negative vorticity is found. Thus, we expect upward motion in between, going even farther to the left near y=7, a weaker center of positive vorticity is found, giving downward motion to the left of the center of negative and to the right of positive vorticity. Finally, for this section we find upward motion to the left of the core of positive vorticity, which agrees with the Ψ function at this level

In Figure 5.1 at x=2, only two centers are present, negative to the right at y=3 and positive to the left at y=6. As depicted by the arrows upward motion at y=1-3 and y=6-7, and downward motion at the center at y=3-6 are found. At x=3 a similar analysis for x=1 is done, where upward motion is at y=1-3 and y=6-7, downward motion at y=3-6.

In Figure 5.3 the analysis is very similar, but interesting features are found at x=5; at y=1-3 and y=6-7 downward motion is found and upward motion at the center

57

y=3-6. In sections x=6 and x=7 both of the single positive vorticity cores are at the center y=4. Then, upward motion is found to the north from y=4-7 and negative to the south from y=4-7. This analysis agrees with the Ψ function, as anticipated.

b. C_y and Ψ Function

In Figure 5.4 three vertical cross-sections are presented for C_y at y=1-3. The pseudo-vorticity field are clearly depicted, positive clock-wise (solid lines) and negative counter clock-wise (dashed lines), the cores of rotation (both positive and negative) are again found mainly around the 100m depth. The same is true for Figures 5.5 for y=3-5 and 5.6 for y=5-7. To analyze and compare the pseudo-vorticity fields with the Ψ function we choose the 100m depth as a base level.

In Figure 5.17 the south boundary that corresponds to y=1 and moves along the x axis from west to east (x=1-7). Compared with Figure 5.4 at y=1, this corresponds to the vertical cross-section of C_y, as we can see at x=5, a core of positive vorticity is found, and at x=1 a core of negative vorticity. We expect upward motion in between these centers, and downward motion at x=5-7. Now, at y=2, almost the same situation as in y=1 is present giving to upward motion at x=1-4 and downward at x=4-7. At y=3 only two centers are present, positive at x=5 and negative at x=2. Then, as depicted by the arrows we found upward motion in between both centers at x=3-5 and downward to at x=1-3 and x=5-7.

In Figure 5.5 and 5.6 the analysis is very similar. As expected, this analysis agrees with the Ψ function and could be repeated at any level and with any cross section.

58

2. Area-2

The technique to analyze this area is similar to that applied in Area-1. All of the plots presented for this area for C_x, C_y and Ψ Function show activity from the surface until near 150m depth, but the level of greatest activity seems to be around the 80m depth.

In Figure 5.19 the Ψ function is plotted at three different depths, 40, 60 and 80m, where we can see upward motion as solid lines and downward motion depicted by dashed lines. Deeper than 140m (Figure 5.21), the magnitude is not great. Also, we can see that the greatest magnitude is found horizontally to the north and especially to the northwest, with very little to the south and almost nothing at center.

3. Remarks

It is interesting to note some important results on the levels of greatest activity in both areas where the cores of positive and negative vorticity and the areas of maximum upward or downward motion were found to affect the baroclinic zone, areas of strongest gradients on temperature, salinity, and density. This is especially true when compared with areas of upward and downward motion with the density fields. The tilt of the isopycnals suggests vertical motion at this level as shown in Figure 5.22-24, vertical cross-sections equivalents to y=1, y=4 and y=7, respectively, for Area-1 as an example.

Another interesting point is that in Area-2 there was more activity at the north than at the south, and almost nothing at the center. The map of dynamic height (Figure 2.7) shows the strongest features are at north and south and not too much in the center.

59

C. CORRELATION

1. Sea Surface Temperature

Figure 5.25 shows a map of surface temperature which overlapped the grid used for this study. In this map we can see a strong correlation between areas of upwelling and the Ψ function at the 1m depth. As an example, for Area-1 some filaments of cold water are present in different sectors such as x=1-3 and y=1-2, x=1-3 and y=6-7, x=5-7 and y=5-6, all of which are in agreement with the Ψ function at the 1m depth as shown in Figure 5.26. For Area-2 the cold filaments are found at x=6-9 and y=18-22, x=2-9 and y=14-16, x=8-9 and y=5-9, also in agreement with the Ψ function at 1m depth as shown in Figure 5.27.

2. Satellite Imagery

Data obtained from the Advanced Very High Resolution Radiometer (AVHRR or AVHRR/2) instruments carried on the TIROS-N/NOAA series of polar orbiting satellites yield the brightness temperature images for the study region. All AVHRR instruments measure emitted radiation in four wavelength bands, visible (0.6-0.7 μm), near infrared (0.7-1.1 μm), and thermal infrared (3.5-3.9 μm and 10.5-11.5 μm). NOAA-9 AVHRR data was left as black body brightness temperatures from channel 4 (10.5-11.5 μm) and were uncorrected for atmospheric contamination. The satellite data were first calibrated and navigated to earth coordinates. Each image was then co-registered to an identical coordinate map of the study region.

Figure 5.28 also shows important information that correlates our analysis. This satellite photography corresponds to the 27 of March at 2200Z. Clear areas represent

60

upwelling and darker areas represent downwelling. Inferred from the satellite images, an analysis of upward and downward motion in Area-1 is found at sectors is listed in Table 5.2.

TABLE 5.2 CORRELATION BETWEEN SATELLITE IMAGERY AND Ψ (Area 1)			
X-Coordinates	Y-Coordinates	Circulation	Correlation with Ψ
x=1-4	y=1-2	Upward	Yes
x=1-4	y=1-2	Upward	Yes
x=1-3	y=5-7	Upward	Yes
x=1-4	y=2-5	Upward	Yes

As we can see, all of these sectors have good correspondence with the Ψ function in Figure 5.26, although part of this area is obstructed by a patch of thick clouds.

In the same way, Area-2 upward and downward motion was found in the sectors listed in Table 5.3.

61

TABLE 5.3 CORRELATION OF SATELLITE IMAGERY AND Ψ (Area 2)			
X-Coordinates	Y-Coordinates	Circulation	Correlation with Ψ
x=1-7	y=20-25	Upward	Yes
x=7-9	y=20-22	Upward	Yes
x=3-5	y=17-19	Upward	Yes
x=6-8	y=16-17	Upward	Yes
x=2-9	y=13-16	Upward	Yes
x=6-9	y=11-13	Upward	Yes
x=7-8	y=6-11	Upward	Yes
x=2-7	y=4-6	Upward	Yes
x=7-9	y=4-5	Upward	No
x=2-5	y=2-4	Upward	Yes
x=1-2	y=1-2	Upward	Yes
x=3-5	y=1-2	Upward	Yes
x=7-8	y=1-2	Upward	Yes
x=8-9	y=23-25	Downward	Yes
x=1-5	y=16-20	Downward	Yes
x=6-9	y=17-20	Downward	Yes
x=1-2	y=8-12	Downward	Yes
x=4-6	y=5-9	Downward	Yes
x=7-9	y=5-6	Downward	Yes
x=2-5	y=4-5	Downward	Yes
x=4-6	y=3-4	Downward	Yes
x=6-9	y=3	Downward	Yes
x=2-4	y=1	Downward	Yes
x=6	y=1	Downward	Yes

There exists a good correlation between areas of great variability and areas where there is not much variability. It is important to notice that during this time some features may move somewhat. In general, however, the analysis demonstrates consistency between the satellite information and the Ψ function.

62

D. CONCLUSIONS

a) A three dimensional pseudo-vorticity field can be obtained from this new concept C-vector method using only CTD measurements (hydrographic data) and wind data. We can either directly visualize three dimensional circulations from the pseudo-vorticity field, or solve the equations (3.8a,b,c) to get three dimensional flow field.

b) Also using this method we can infer vertical motions especially from the close relation obtained between the vertical velocity with the Ψ function.

c) At this time, the "quasi-geostrophic" system assumed in this study is considered to be a valid approach to the problem, but it does not accurately represent conditions found in the real world. Development of an approach that considers conditions left unaddressed by the quasi-geostrophic assumption will enable even more realistic results to be achieved..
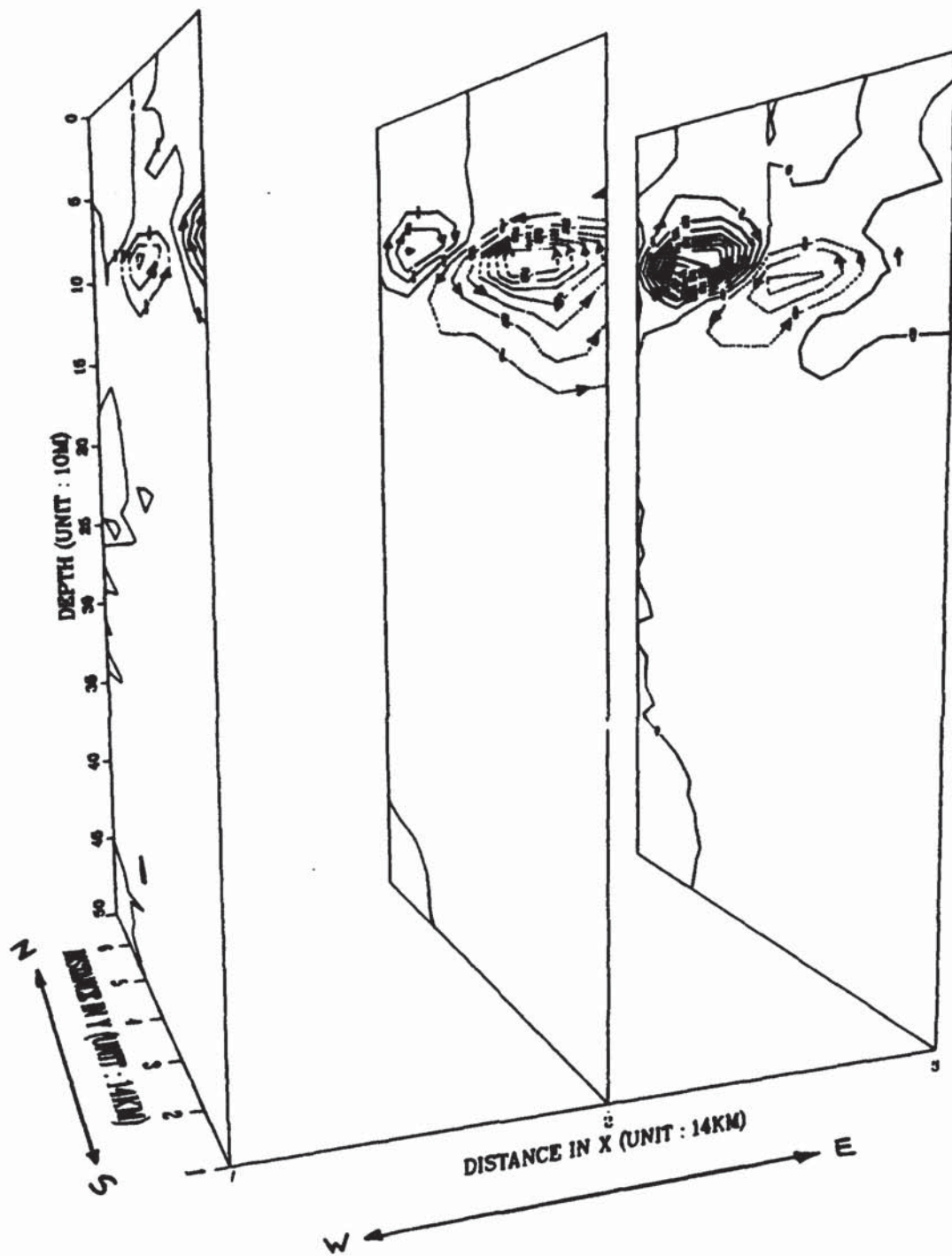
Figure 5.1 C_x Cross-Sections at x=1-3 from Area-1.

64
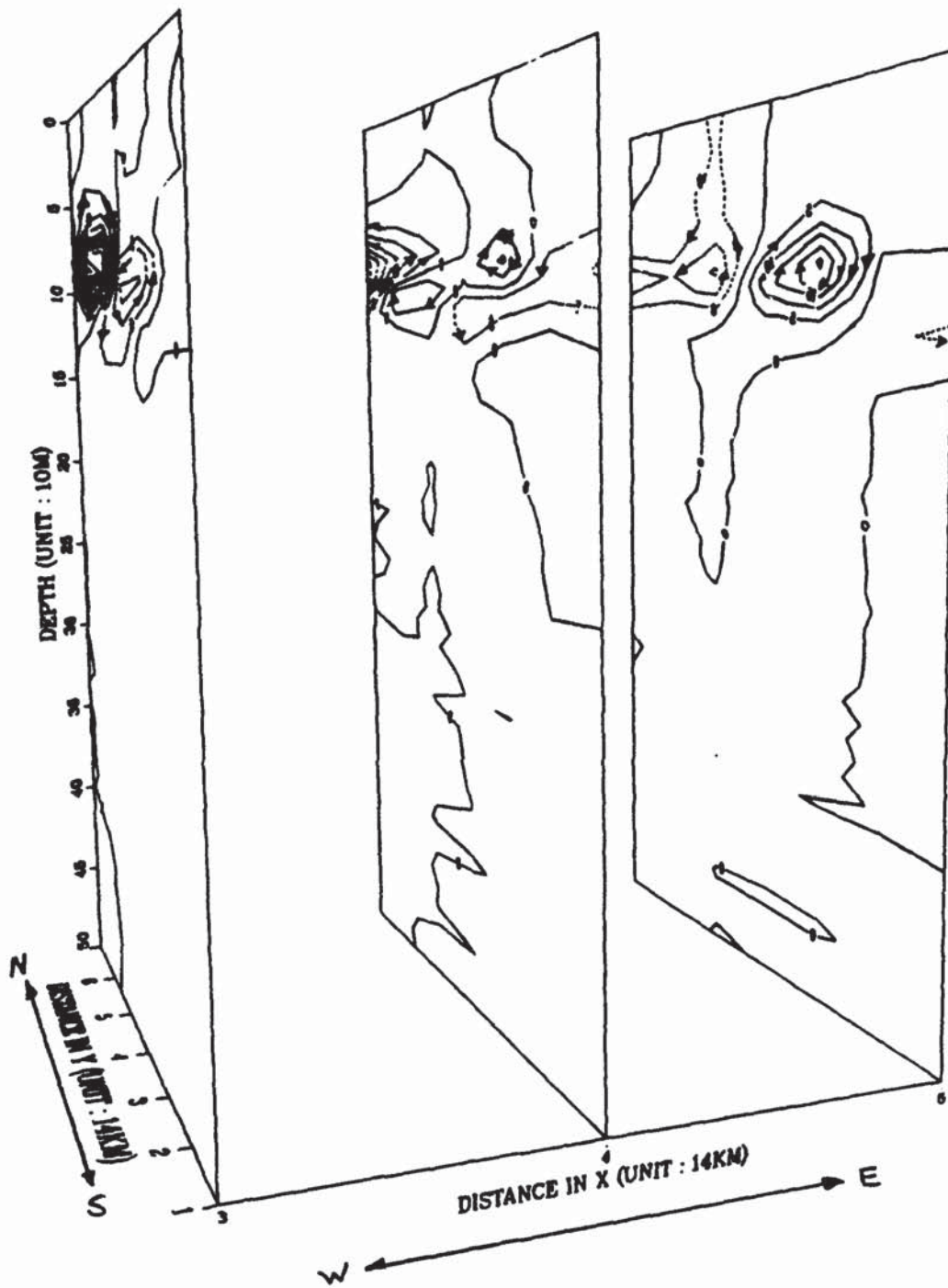
Figure 5.2 C, Cross-Sections at x=3-5 from Area-1.

65
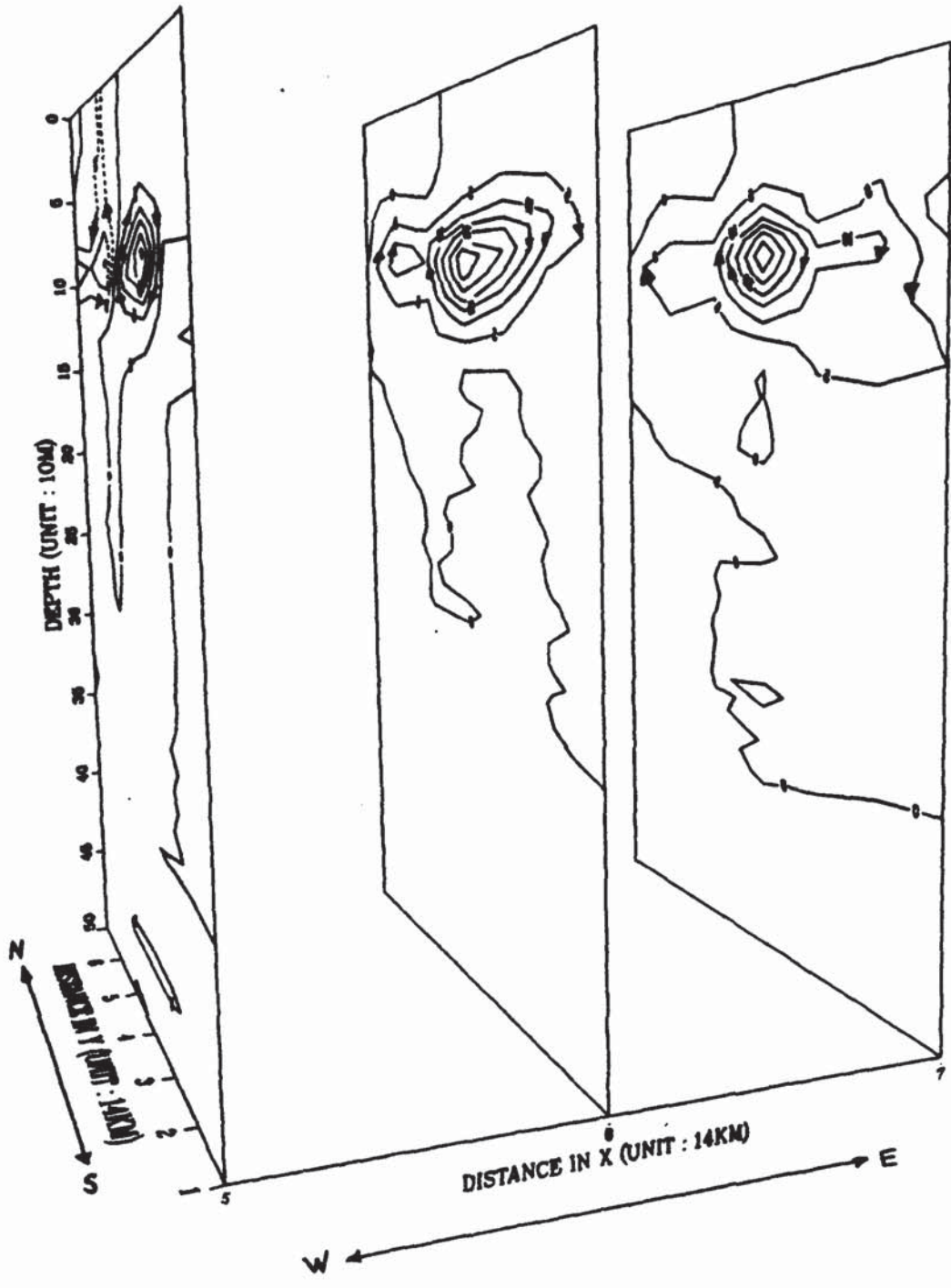
Figure 5.3 C_x Cross-Sections at x=5-7 from Area-1.

66
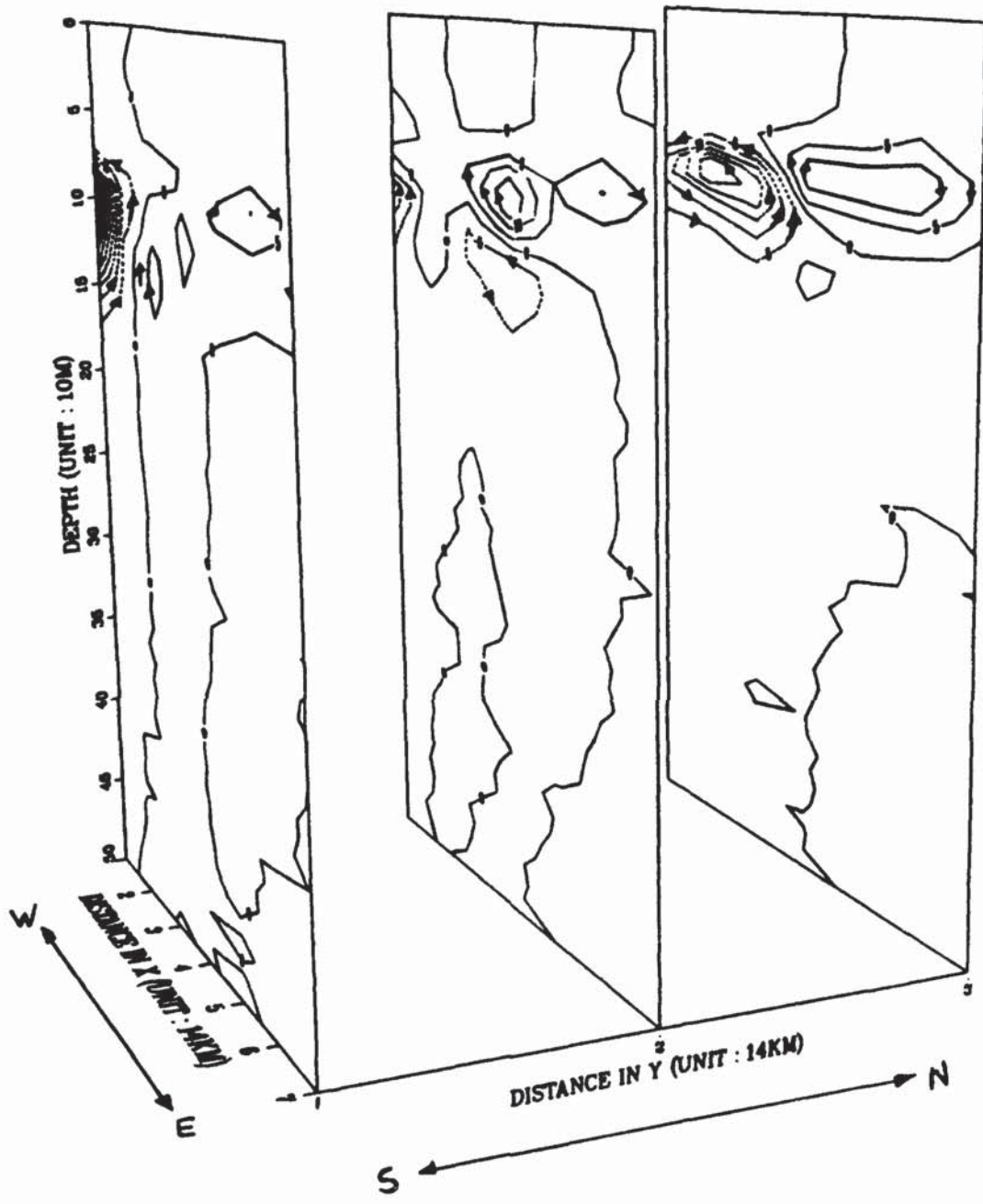
Figure 5.4 C_y Cross-Sections at y=1-3 from Area-1.
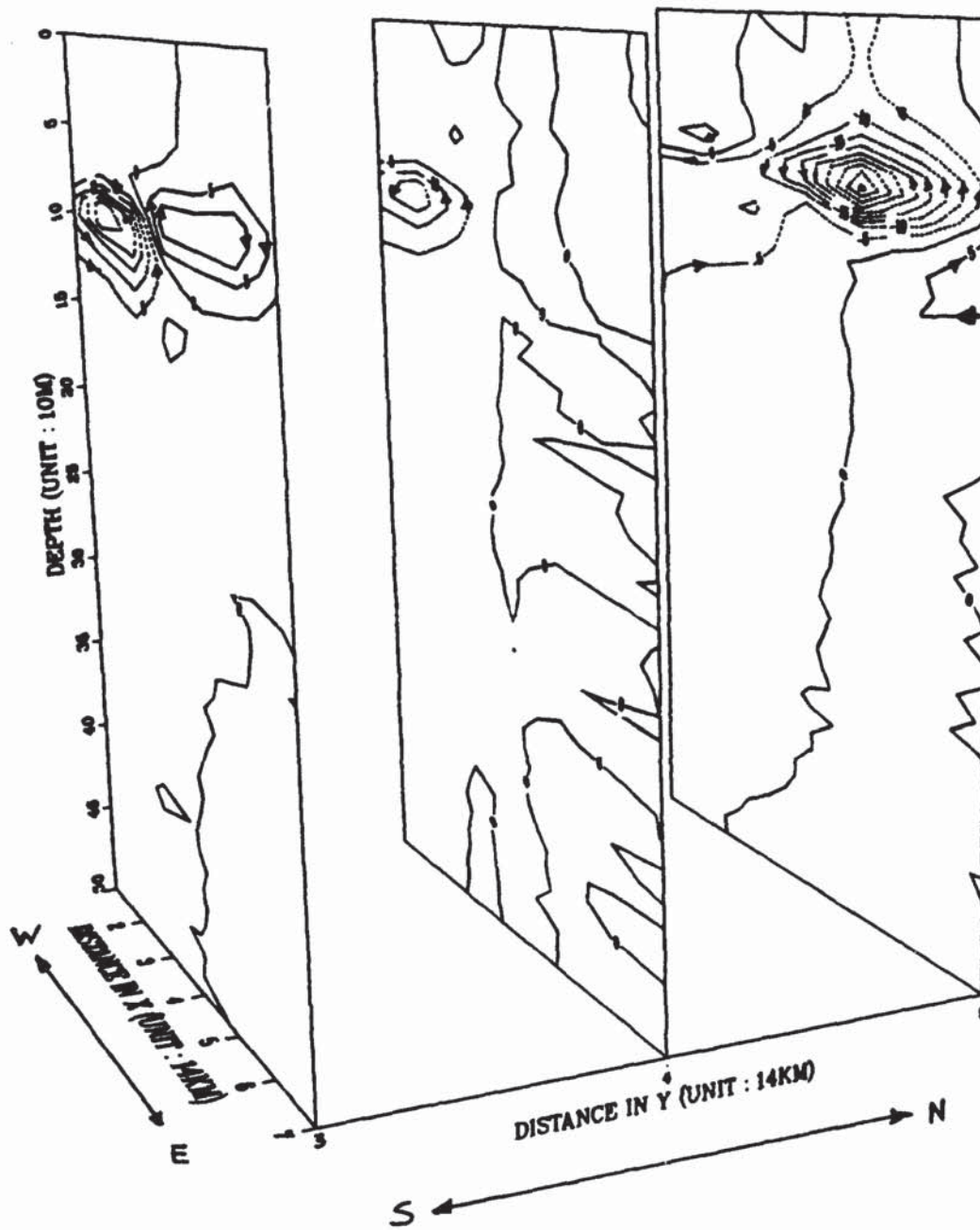
Figure 5.5 C_y Cross-Sections at y=3-5 from Area-1.
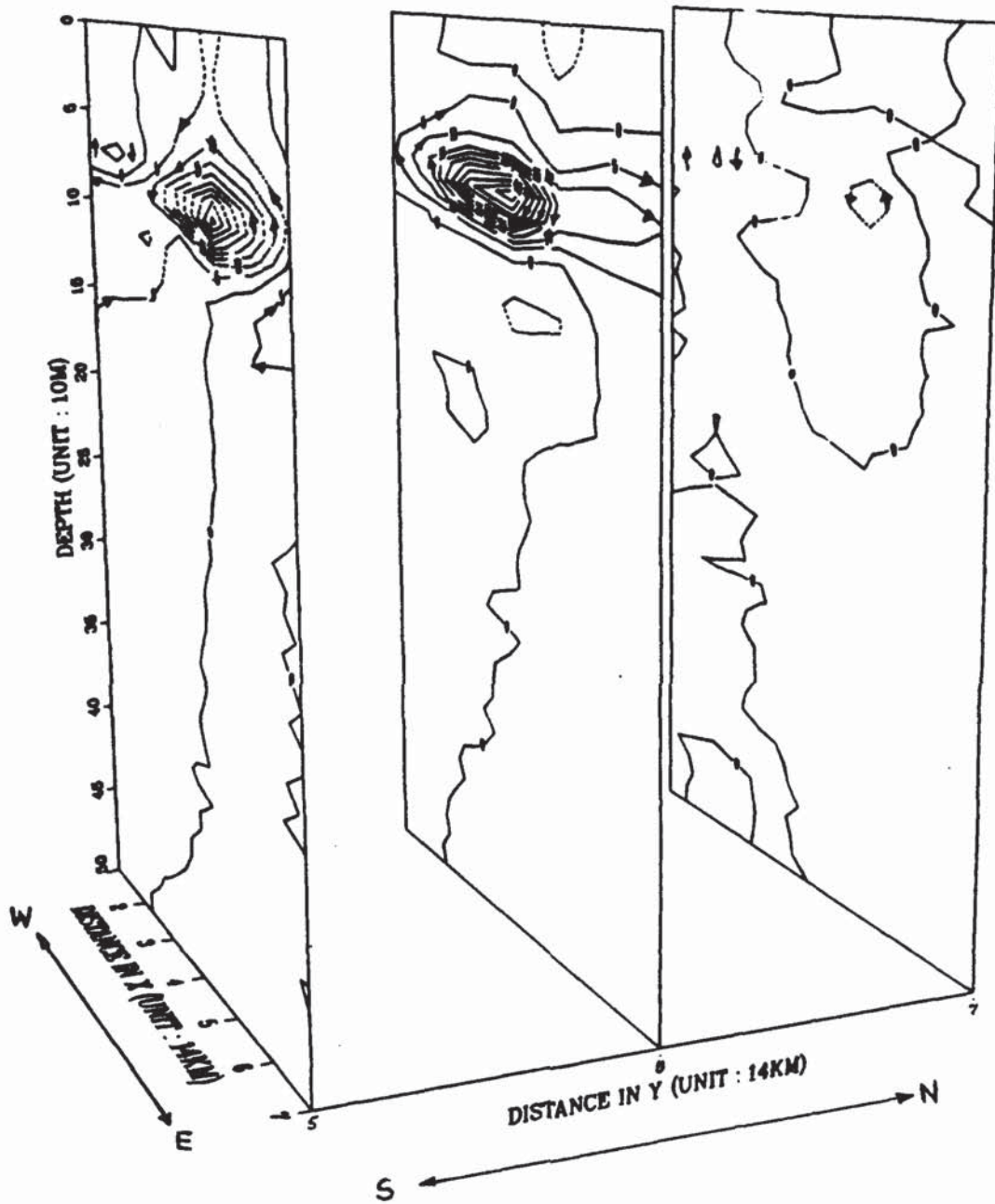
Figure 5.6 C_y Cross-Sections at y=5-7 from Area-1.
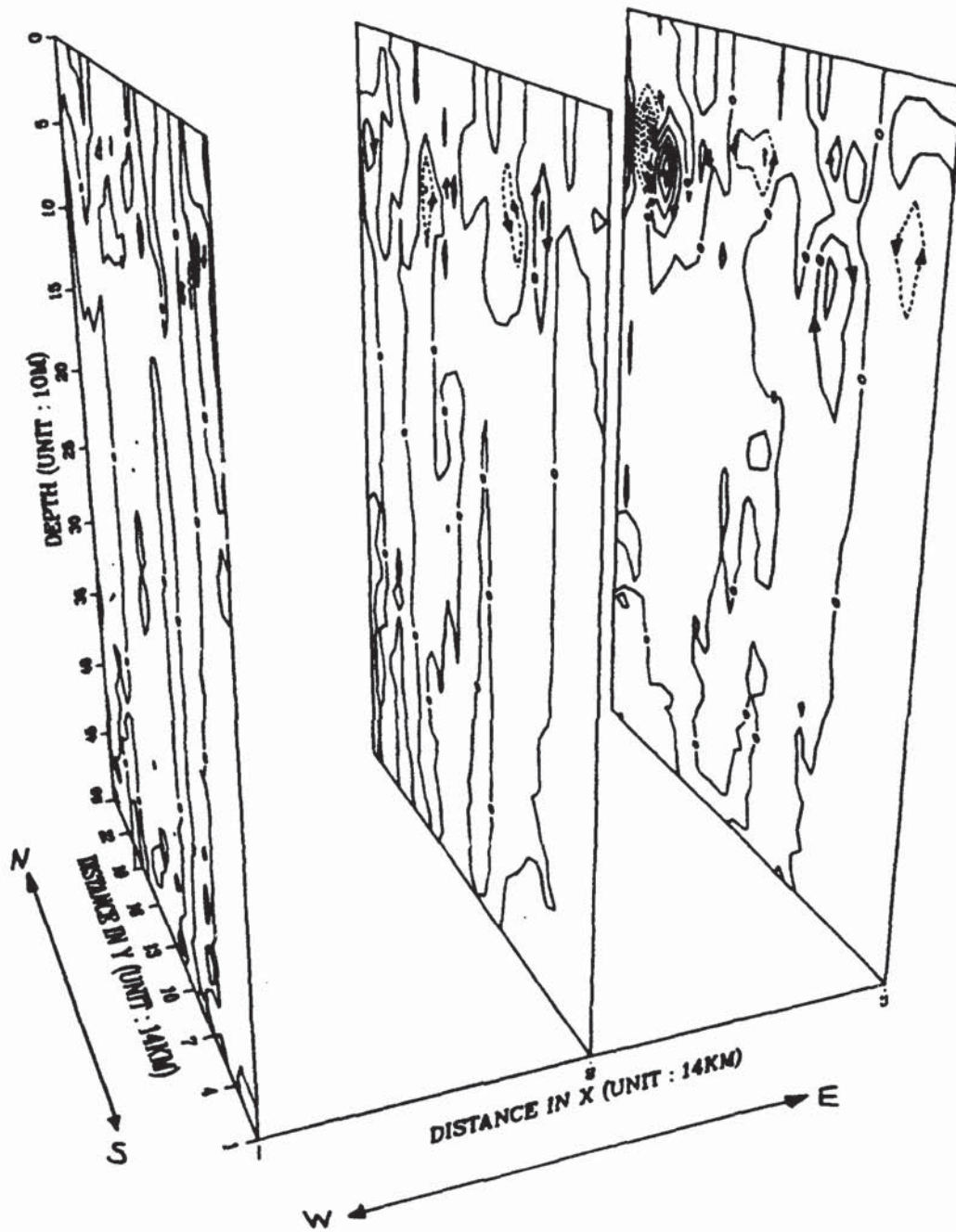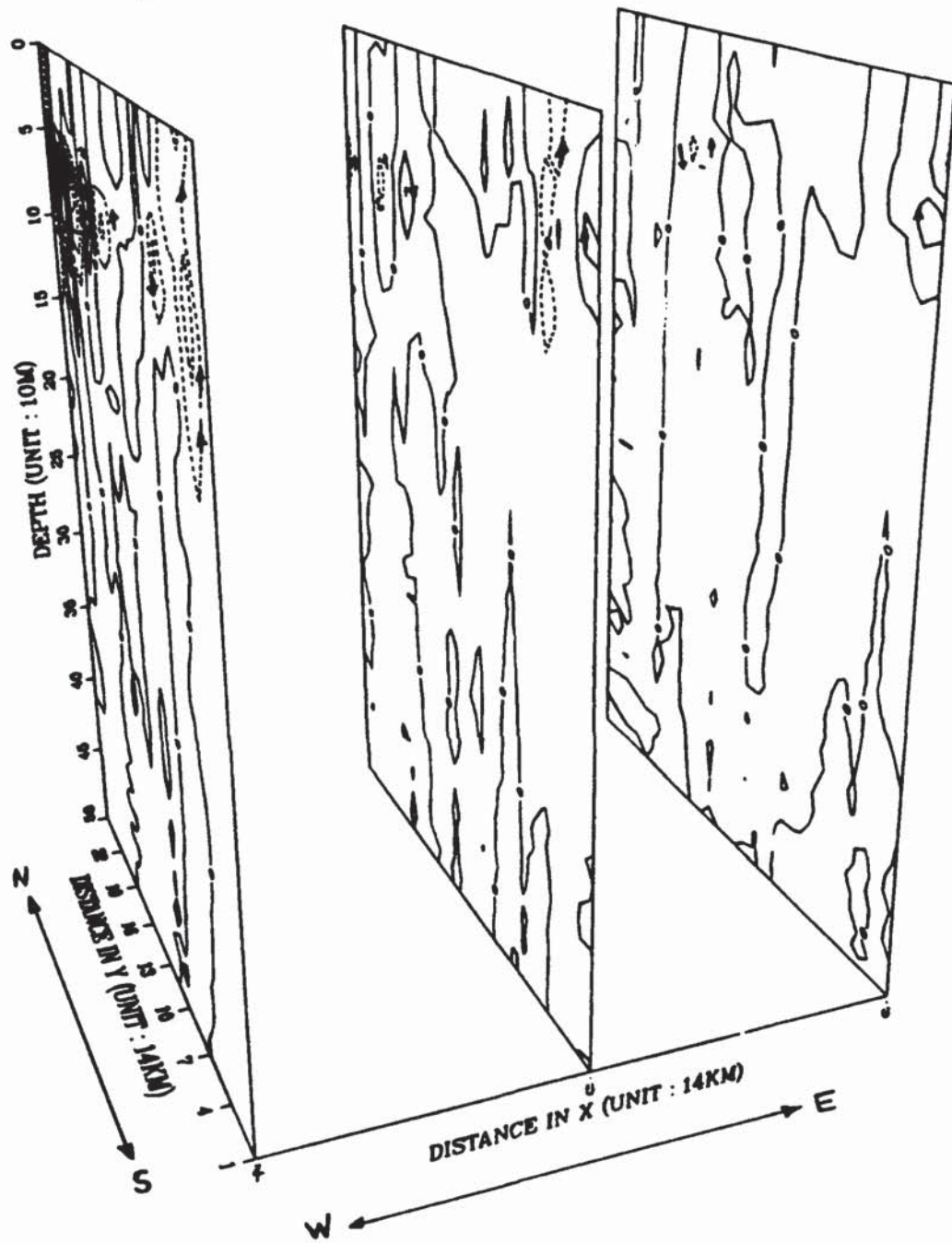
Figure 5.7 C, Cross-Sections at x=1-3 from Area-2.
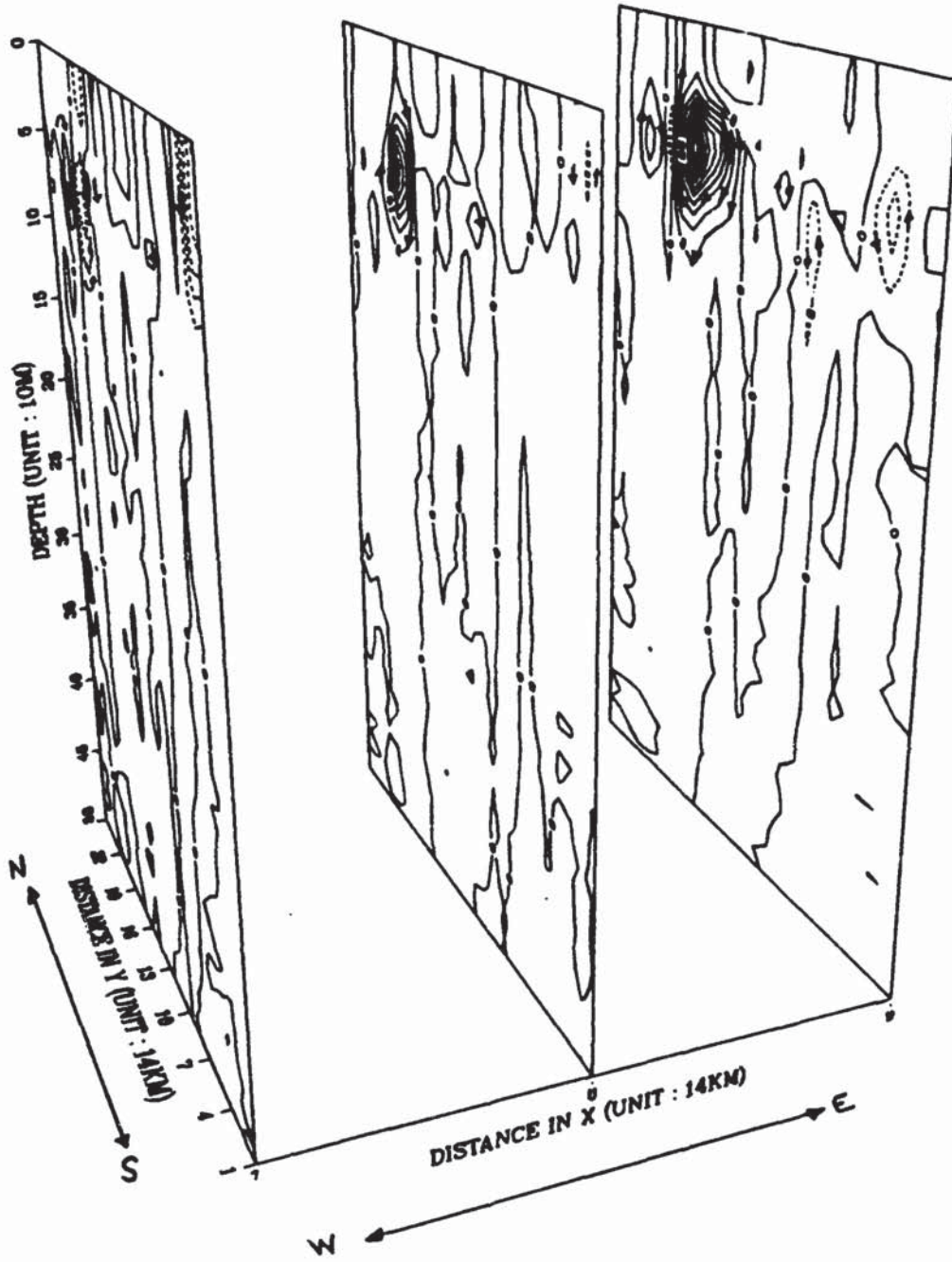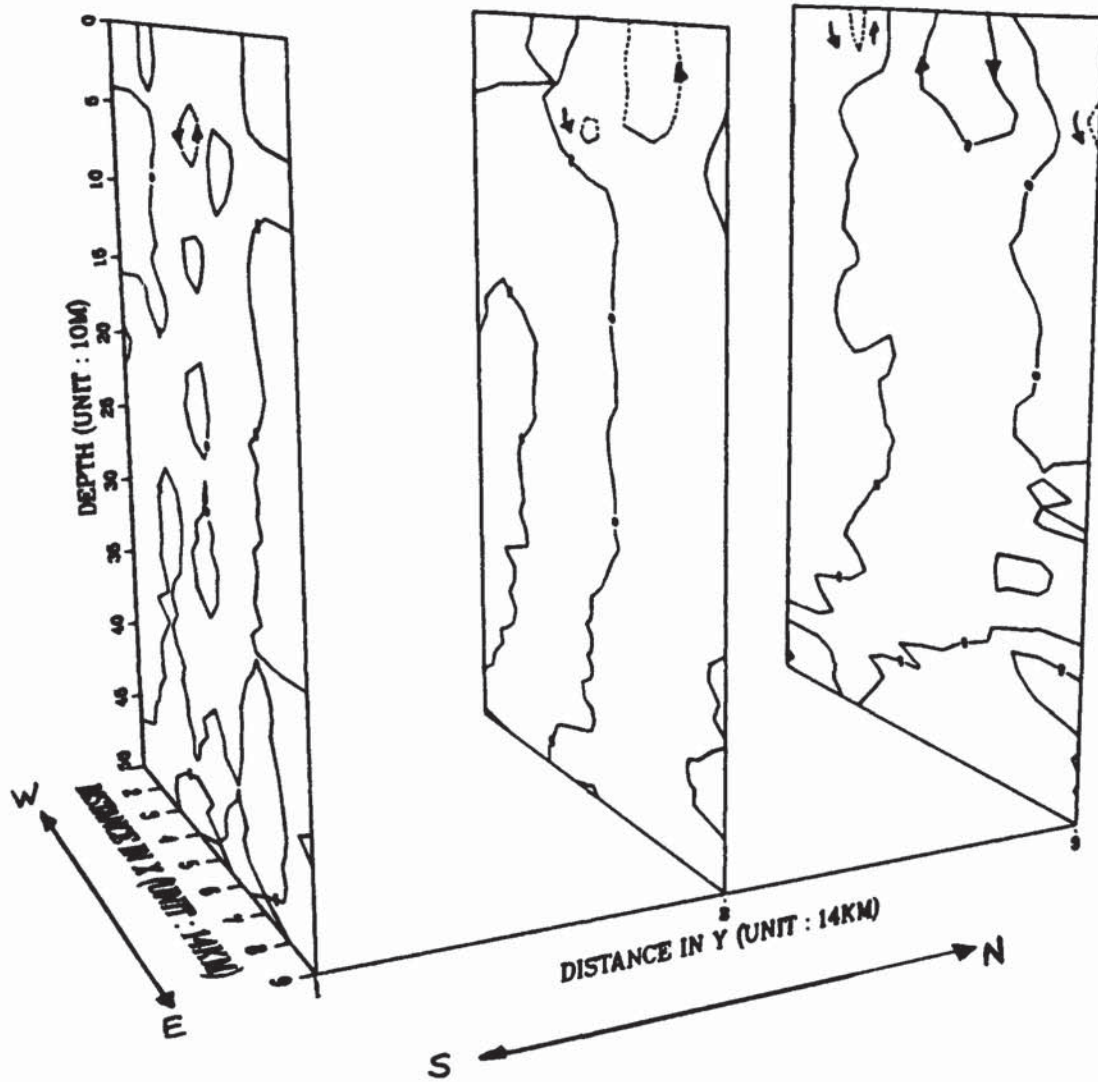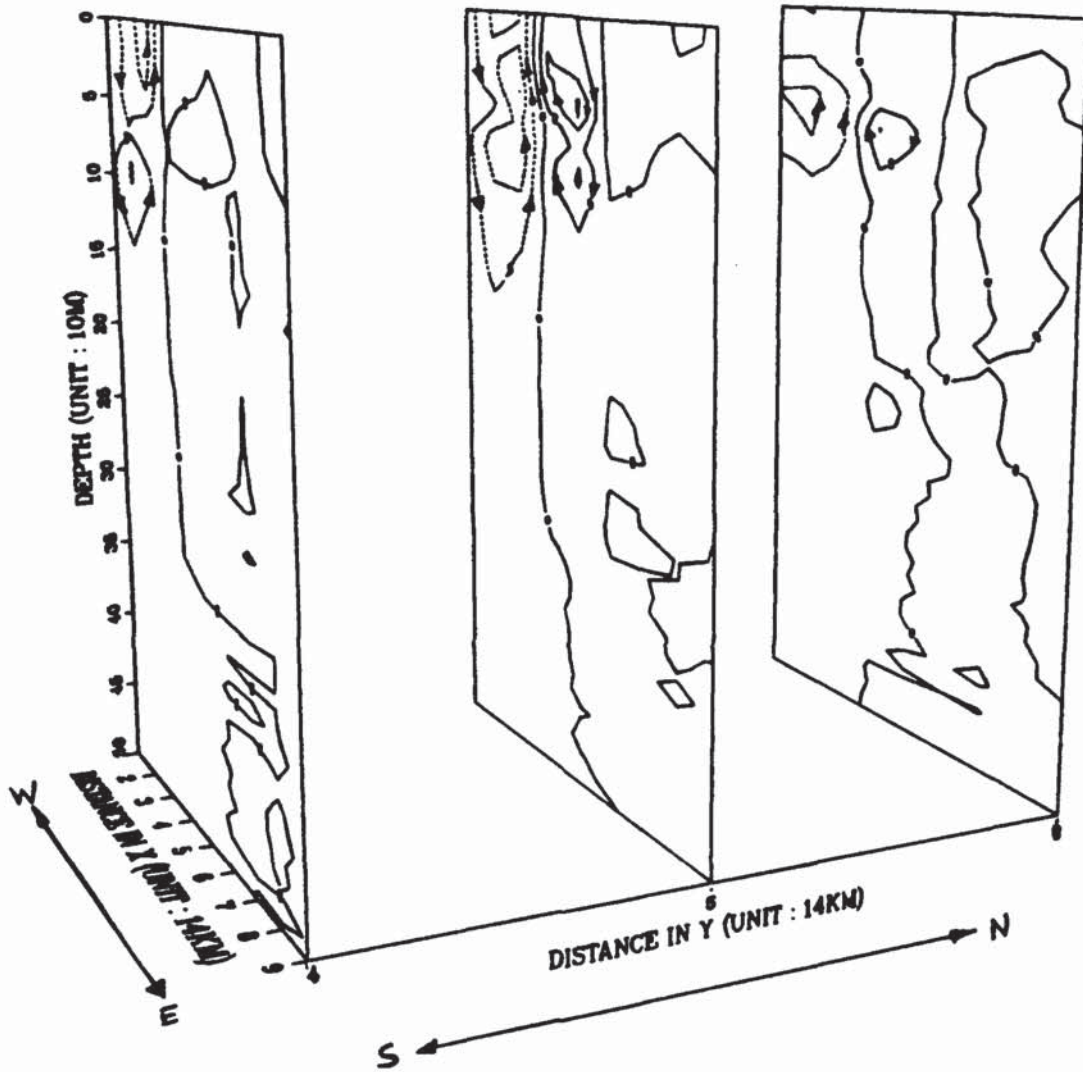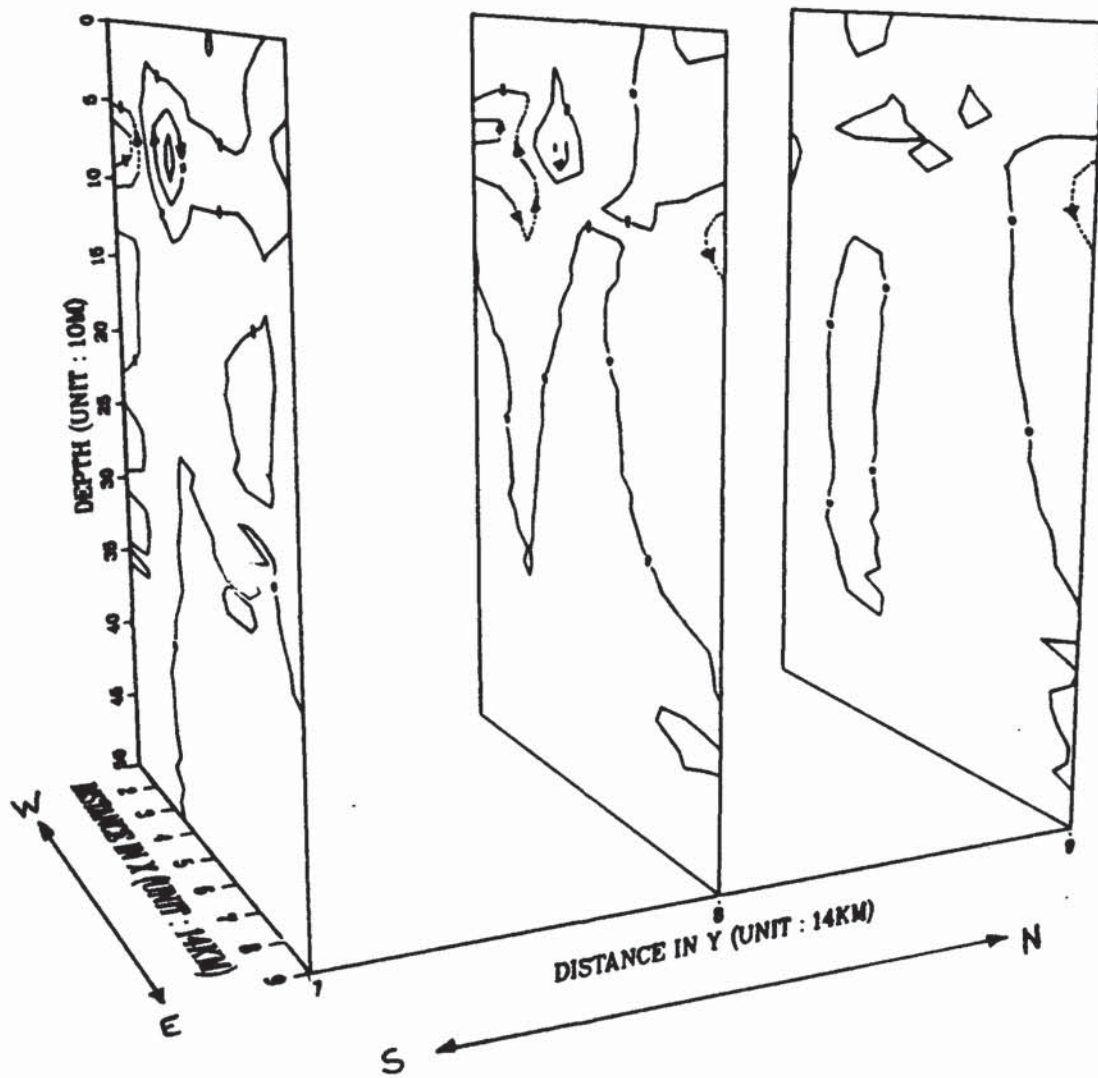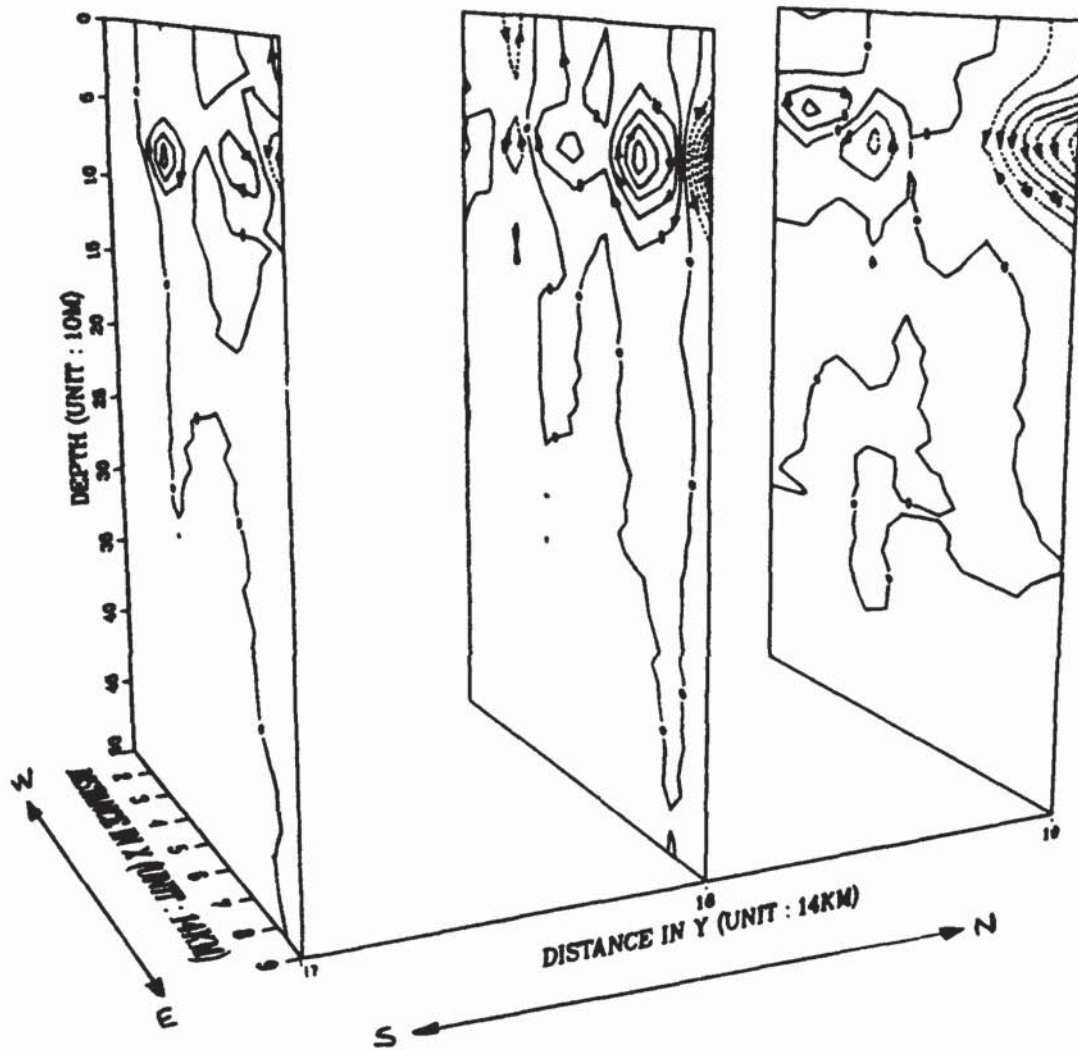
70

Figure 5.8 C, Cross-Sections at x=4-6 from Area-2.

71

Figure 5.9 C_t Cross-Sections at x=7-9 from Area-2.

72

Figure 5.10 C_y Cross-Sections at y=1-3 from Area-2.

73

Figure 5.11 C_y Cross-Sections at y=4-6 from Area-2.

74

Figure 5.12 C_y Cross-Sections at y=7-9 from Area-2.

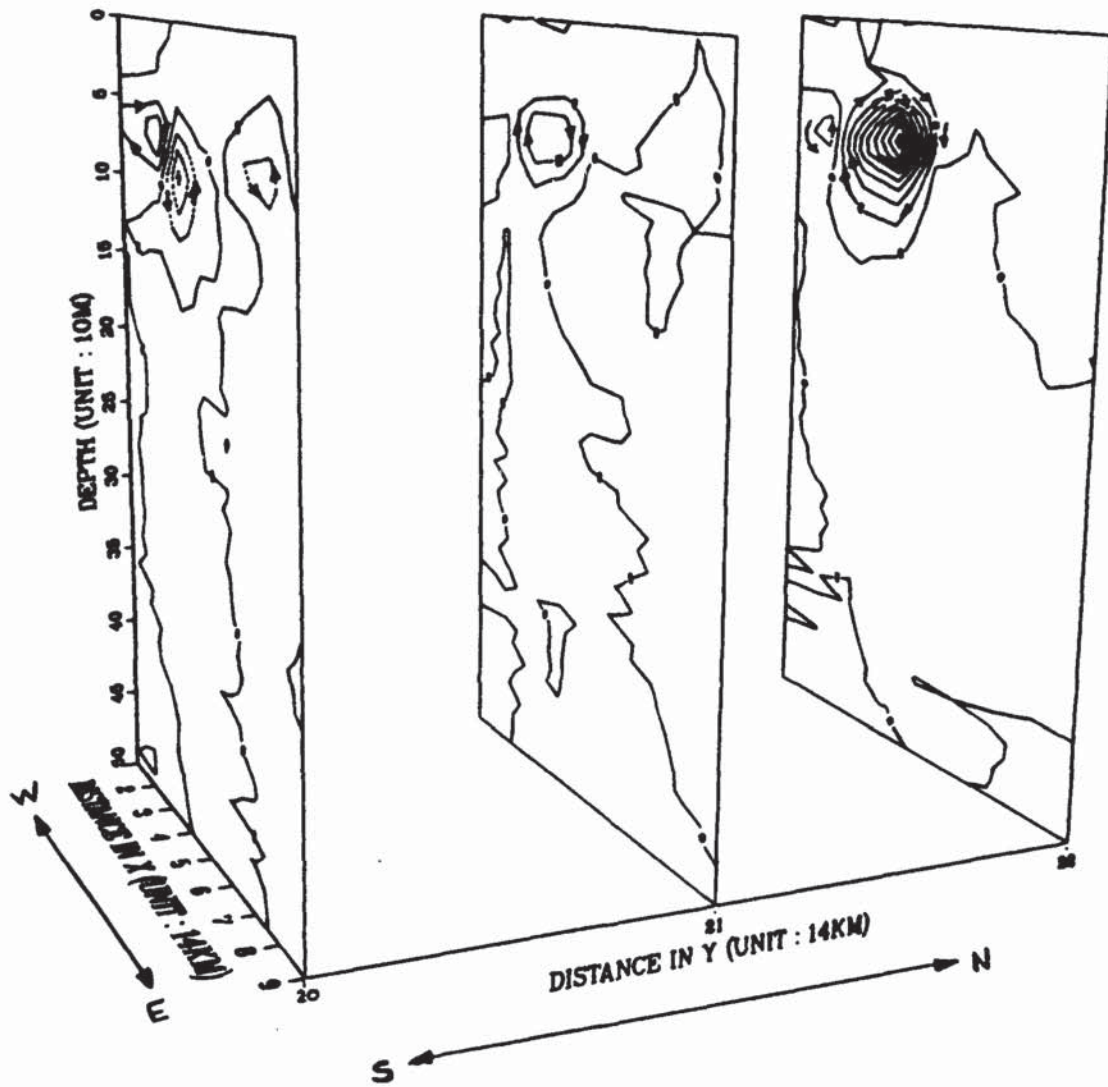Figure 5.13 C_2 Cross-Sections at y=17-19 from Area-2.

76

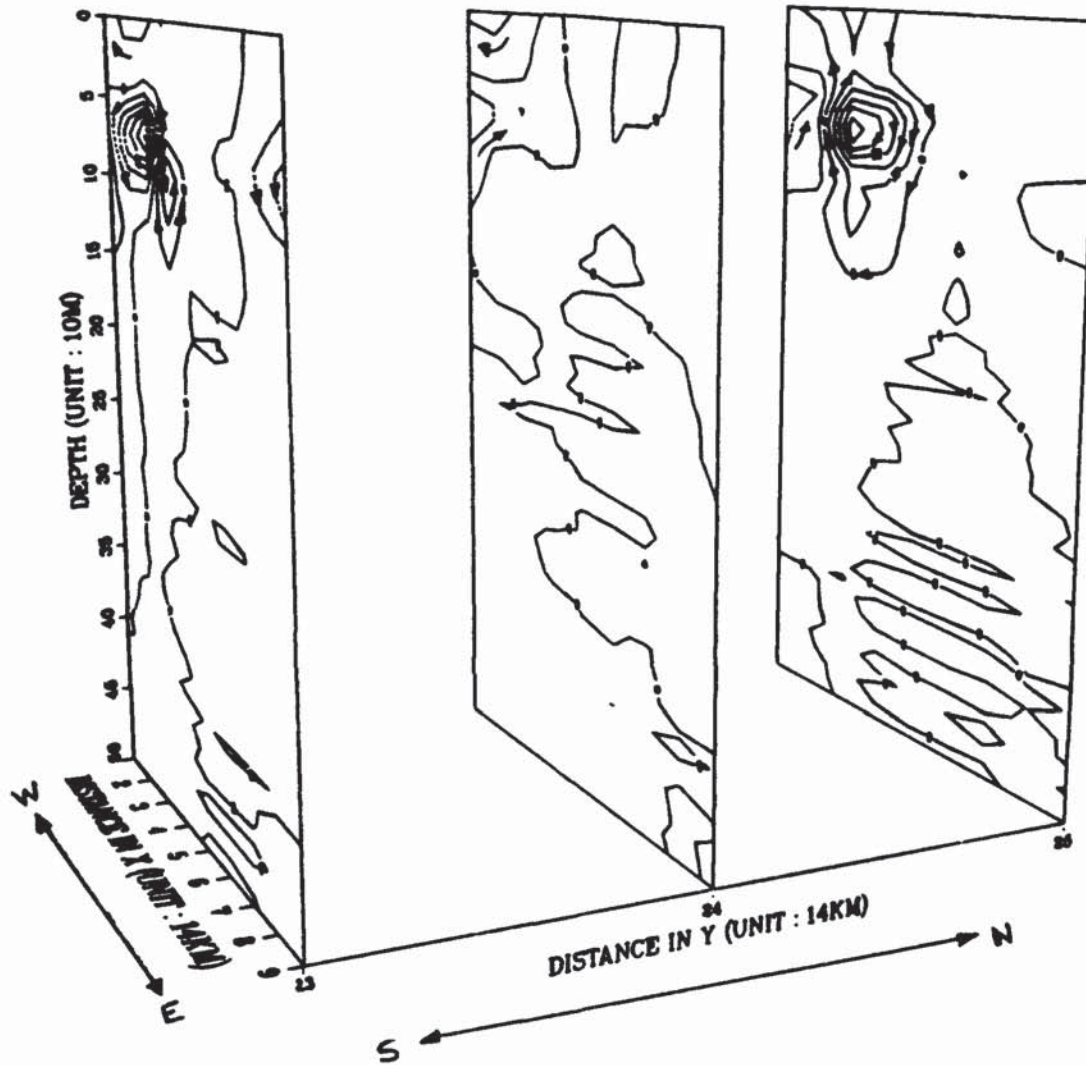Figure 5.14 C_y Cross-Sections at y=20-22 from Area-2.
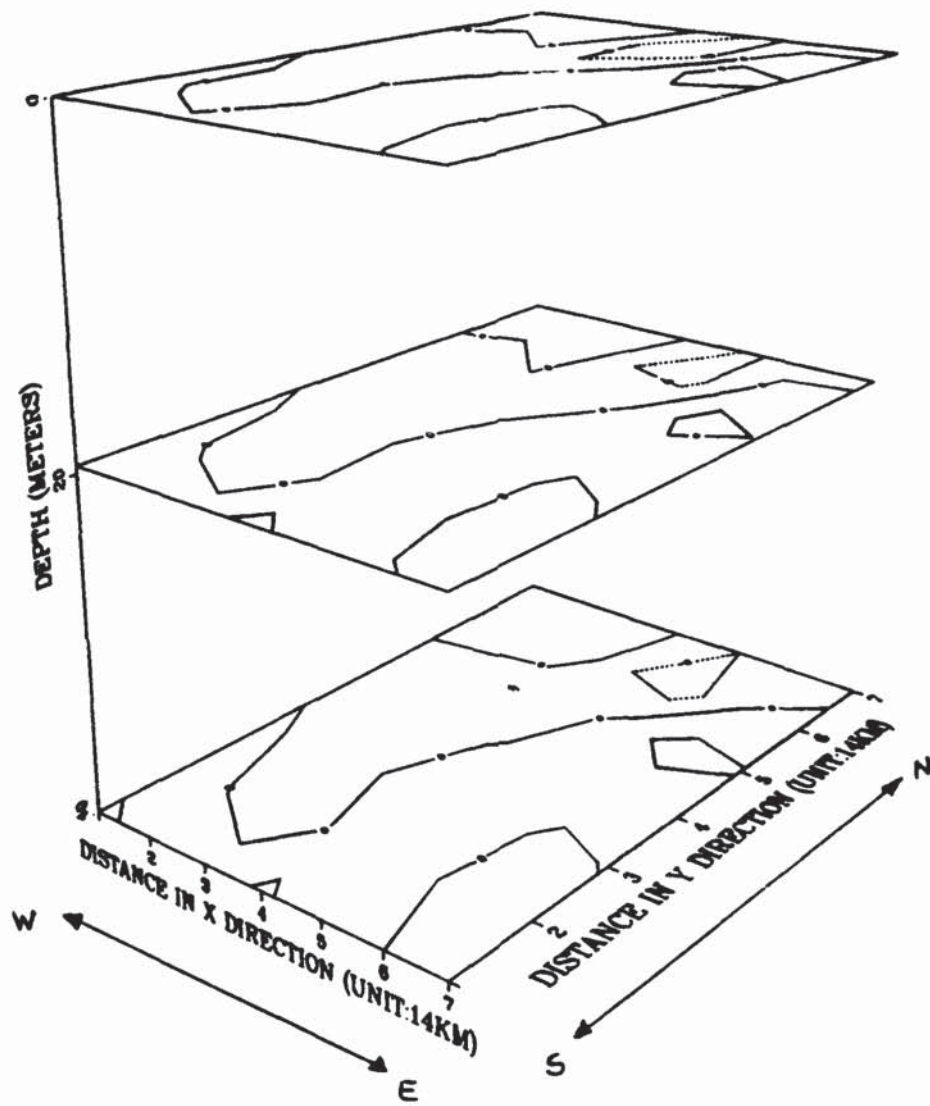
77

Figure 5.15 C_y Cross-Sections at y=23-25 from Area-2.

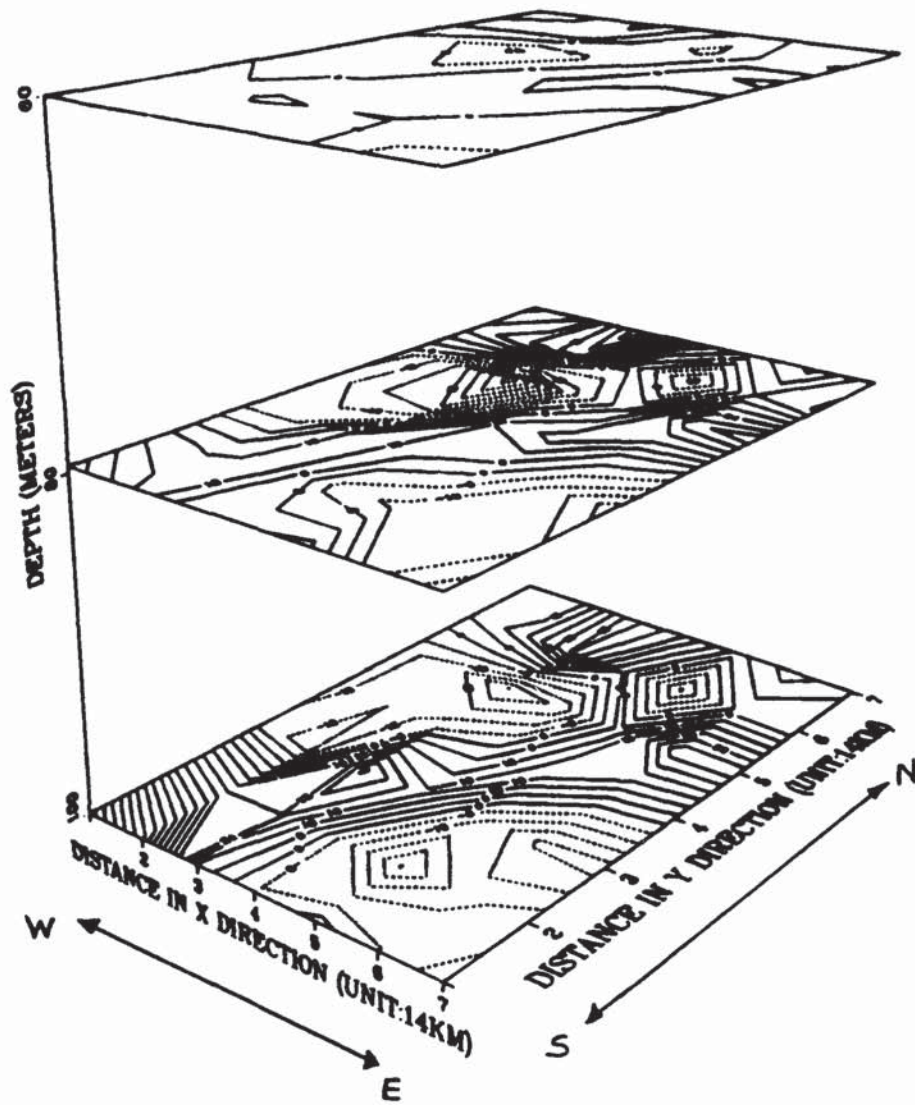Figure 5.16. Ψ at three different depths, 0, 20, 40m Area-1.

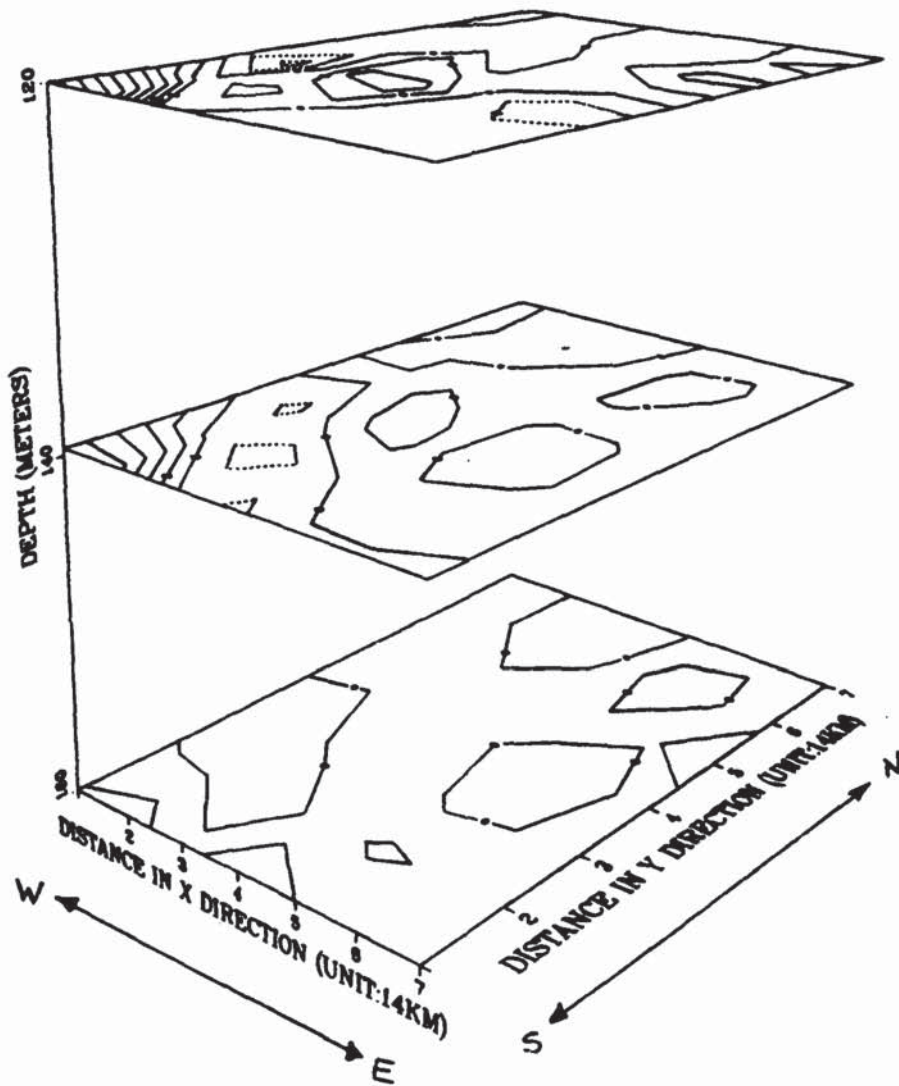Figure 5.17. Ψ at three different depths, 60, 80, 100m Area-1.

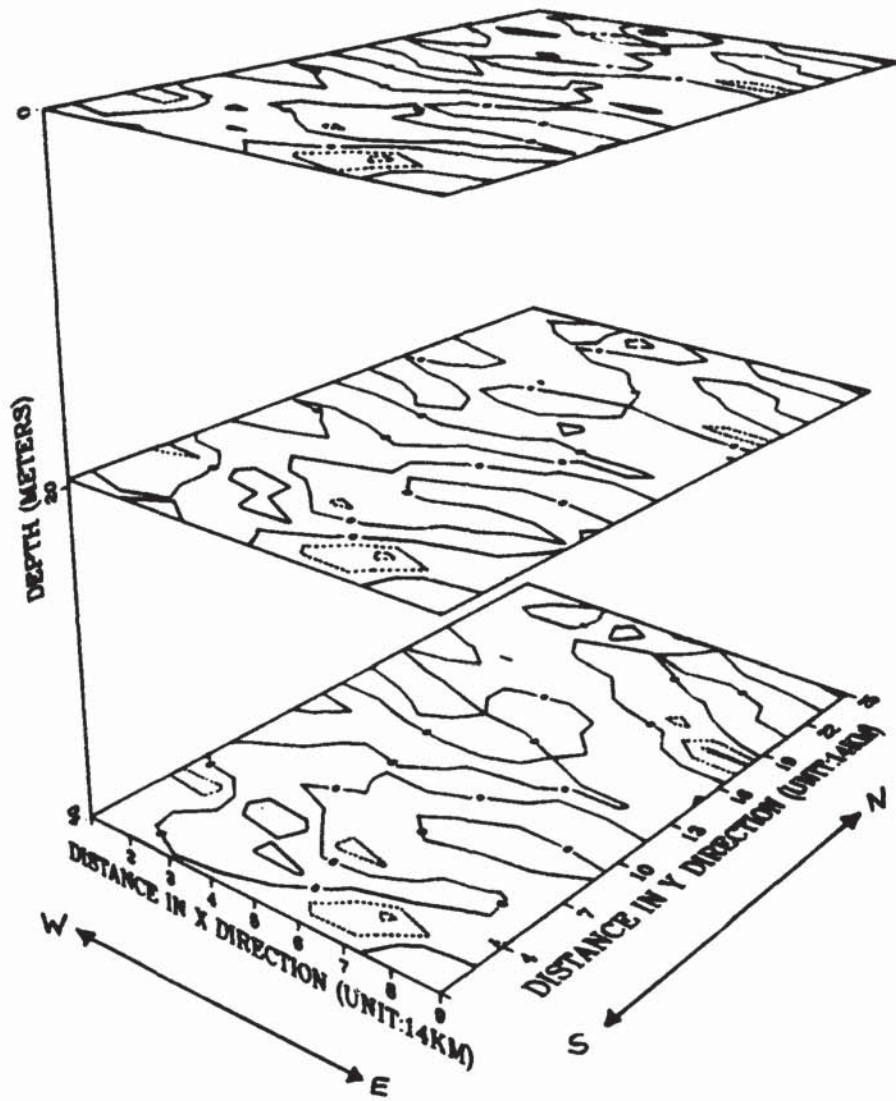Figure 5.18. Ψ at 3 different depths, 120, 140, 160m Area-1.

81

Figure 5.19. Ψ at three different depths, 0, 20, 40m Area-2.
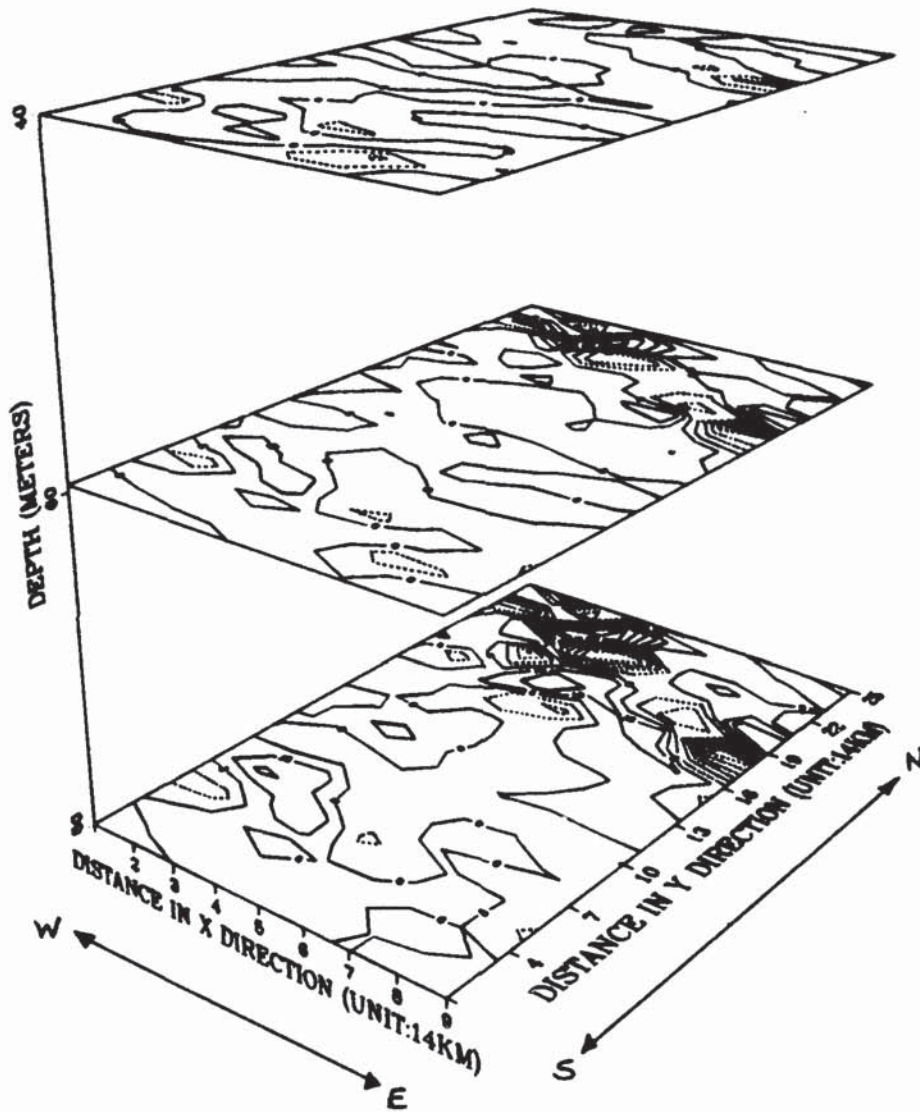
Figure 5.20. Ψ at three different depths, 40, 60, 80m Area-2.
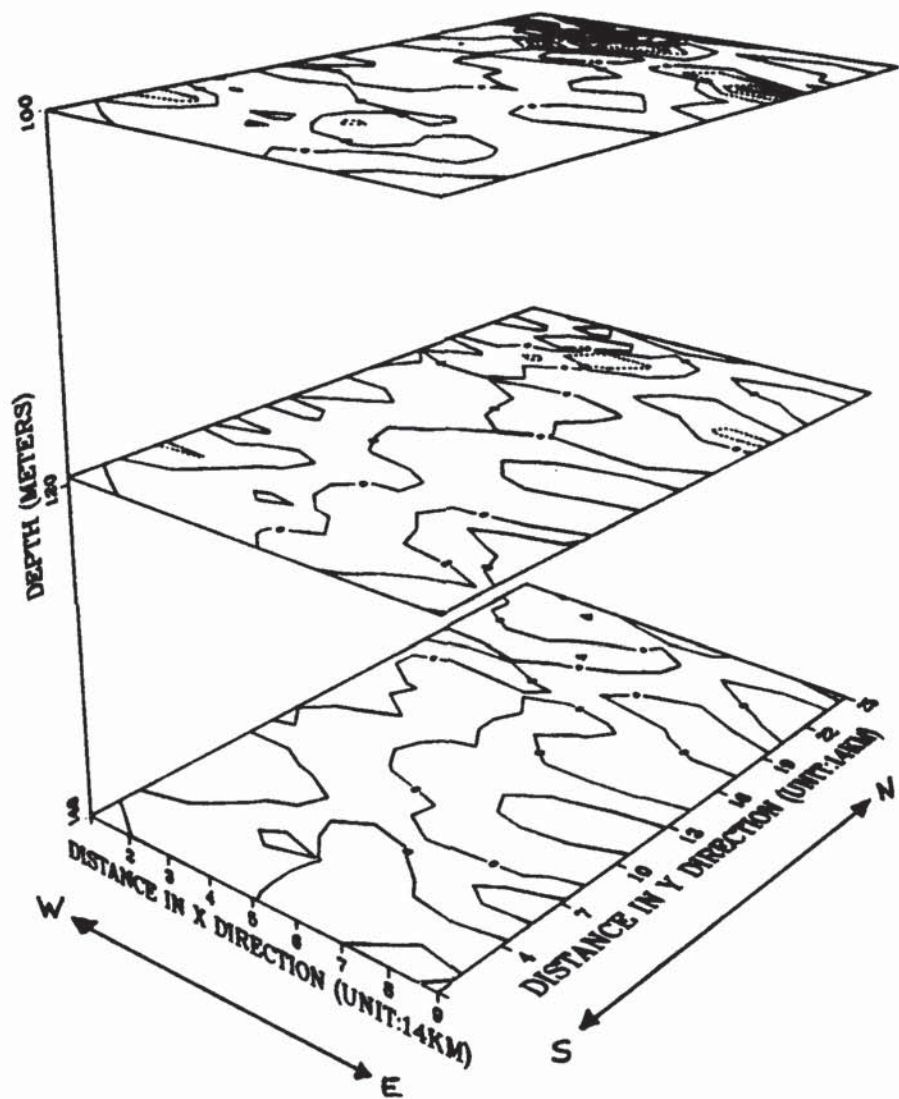
Figure 5.21. Ψ at 3 different depths, 100, 120, 140m Area-2.

Figure 5.22. Vertical section of density anomaly (Jessen, 1989). Compare with y=1 from Area-1.

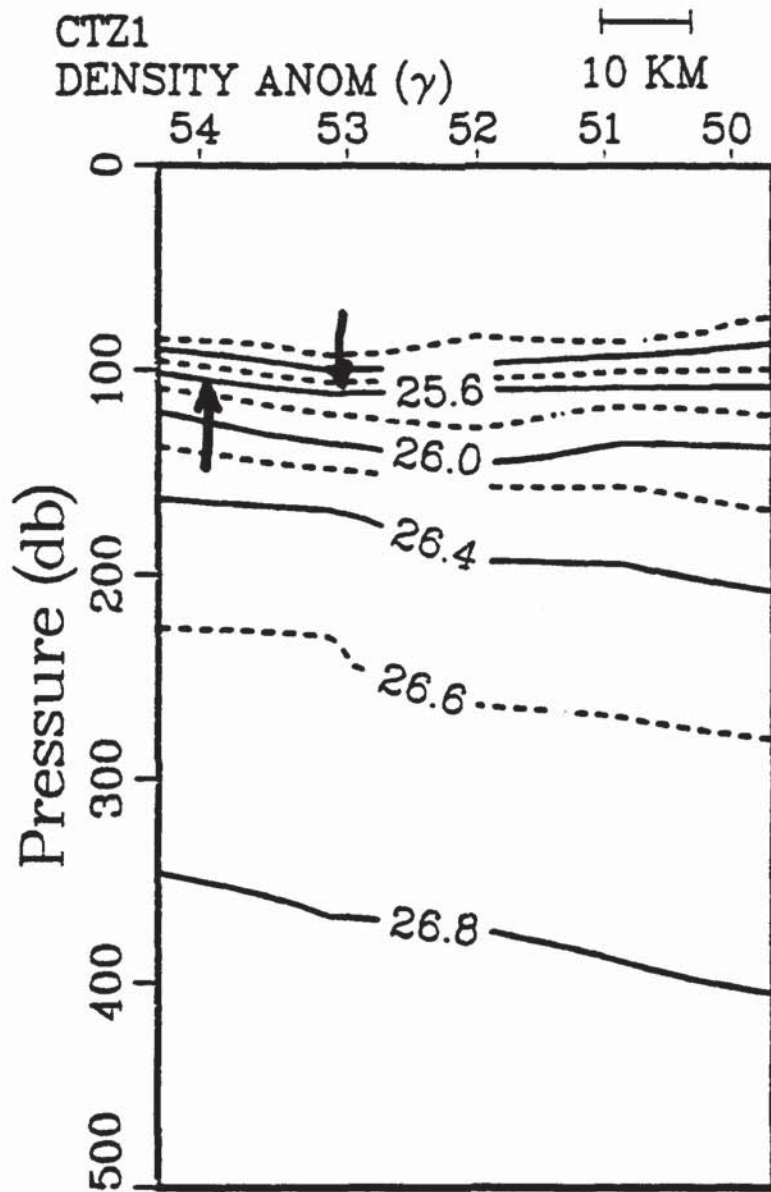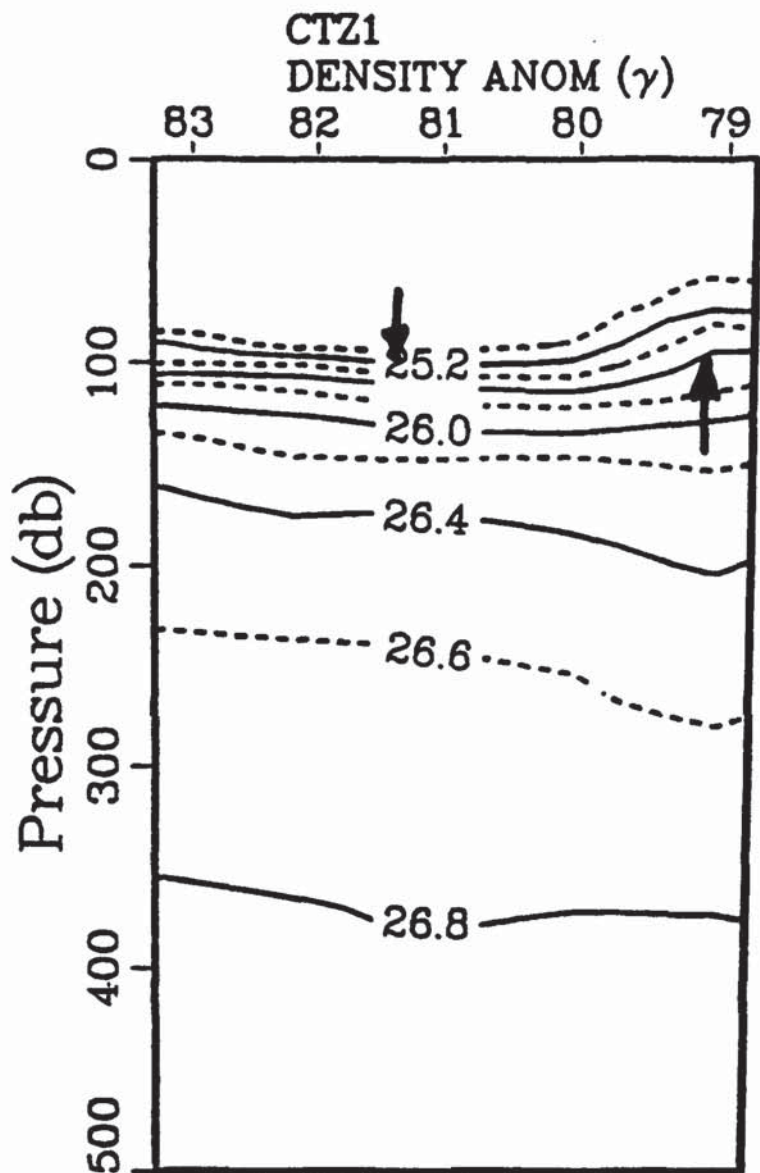**Figure 5.23.** Vertical section of density anomaly (Jessen, 1989). Compare with y=4 from Area-1.

86
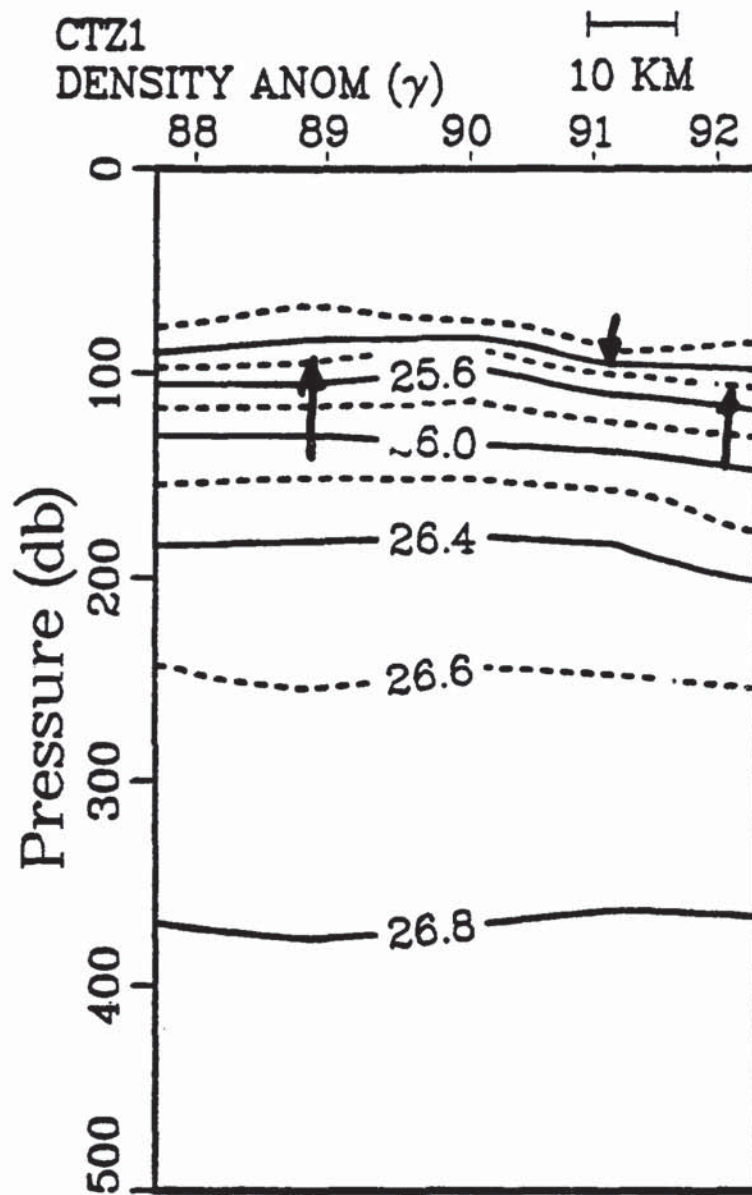
Figure 5.24. Vertical section of density anomaly (Jessen, 1989). Compare with y=7 from Area-1.
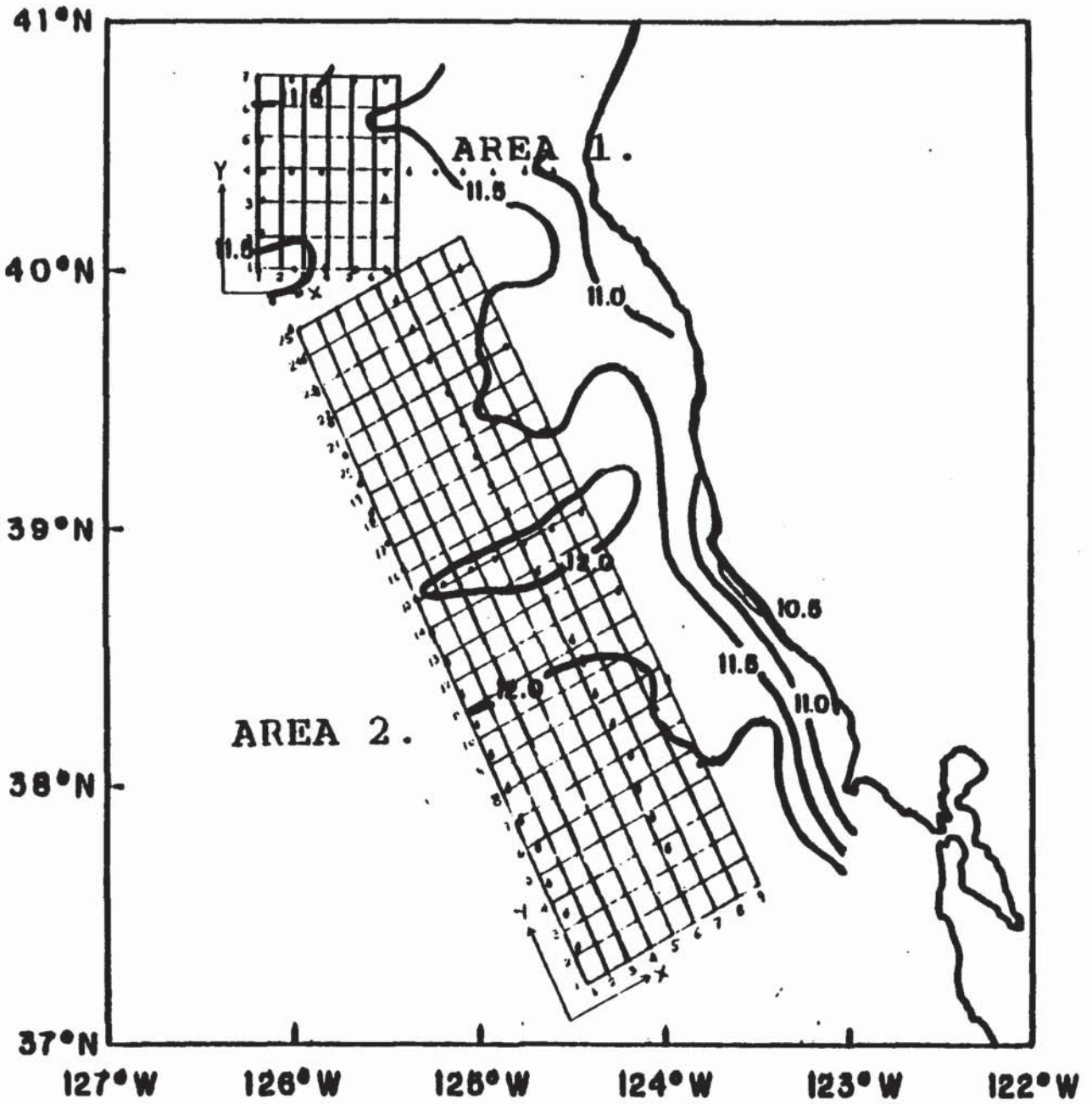
Figure 5.25. Map of surface temperature Cruise CTZ1 (Jessen, 1989), overlapped by the grid used for this study.

88
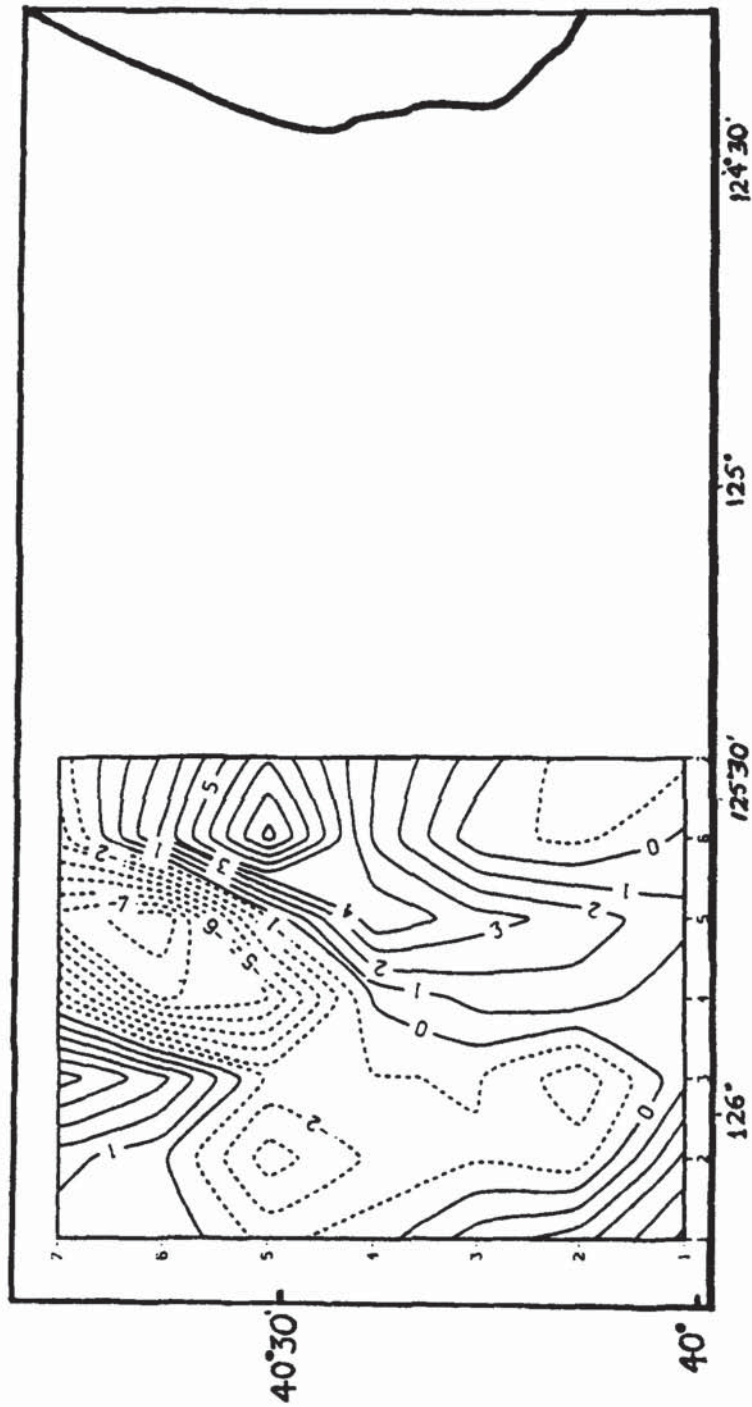
Figure 5.26. Ψ function at 1m depth from Area-1.

89
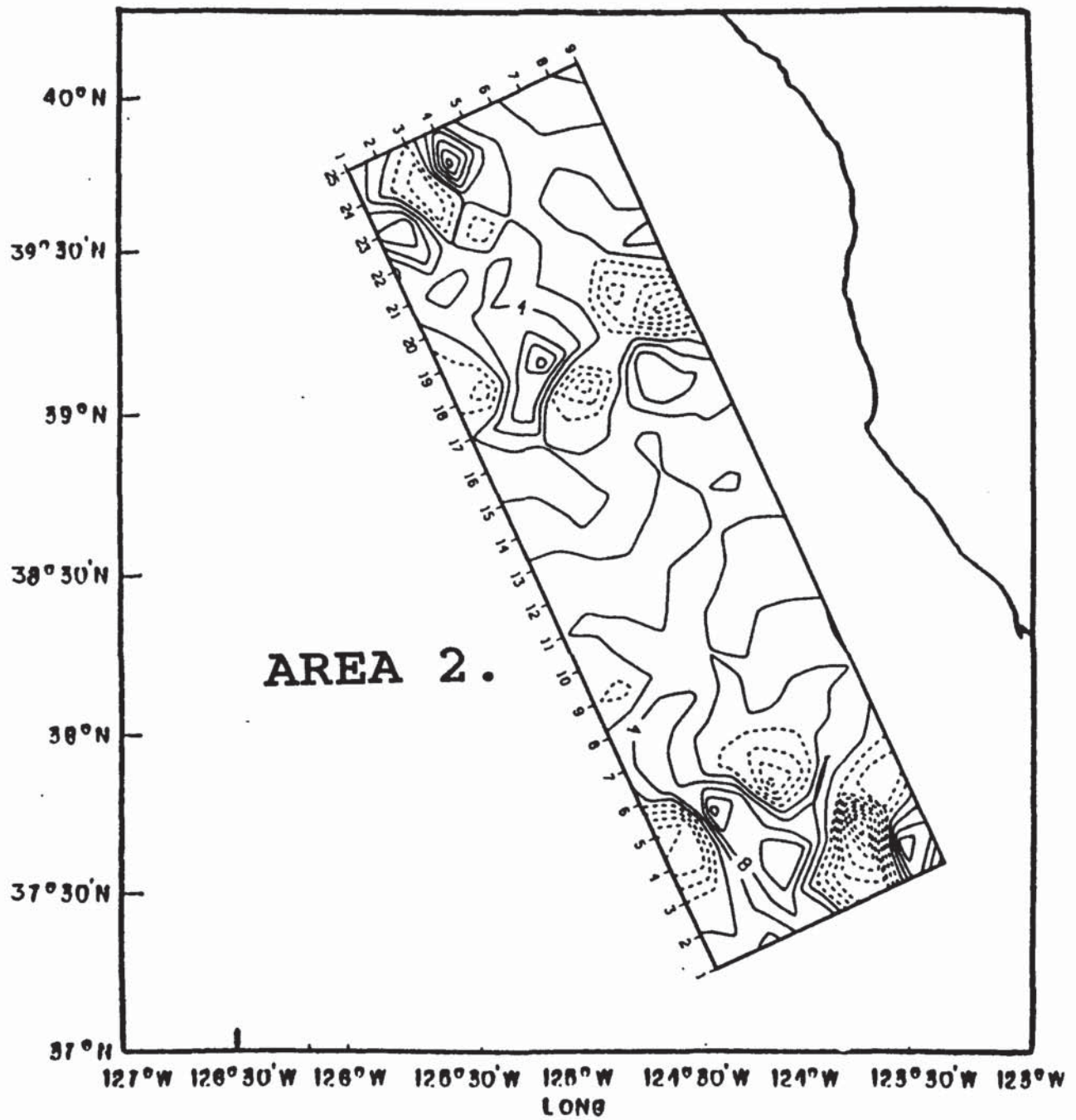
Figure 5.27. Ψ function at 1m depth from Area-2.

Figure 5.28. Satellite (NOAA-9) AVHRR infrared image of brightness temperature (March-27-2200z). Lighter shades indicate colder brightness temperatures.

91

LIST OF REFERENCES

Barnes, S. L., "A Technique For Maximizing Details In Numerical Weather Map Analyses," *J. Appl. Meteor.*, 3. pp. 396-409, 1964.

Barnes, S. L., "Mesoscale Objective Map Analysis Using Weighted Time Series Observations," NOAA Tech. Memo. ERL NSSL-62, 60 PP. [NTIS COM-73-10781], 1973.

Brink, K.H., and Cowles, T. J., "The Coastal Transition Zone Program," *Journal of Geophysical Research*, Vol. 96, pp. 14,637-14,647, 1991.
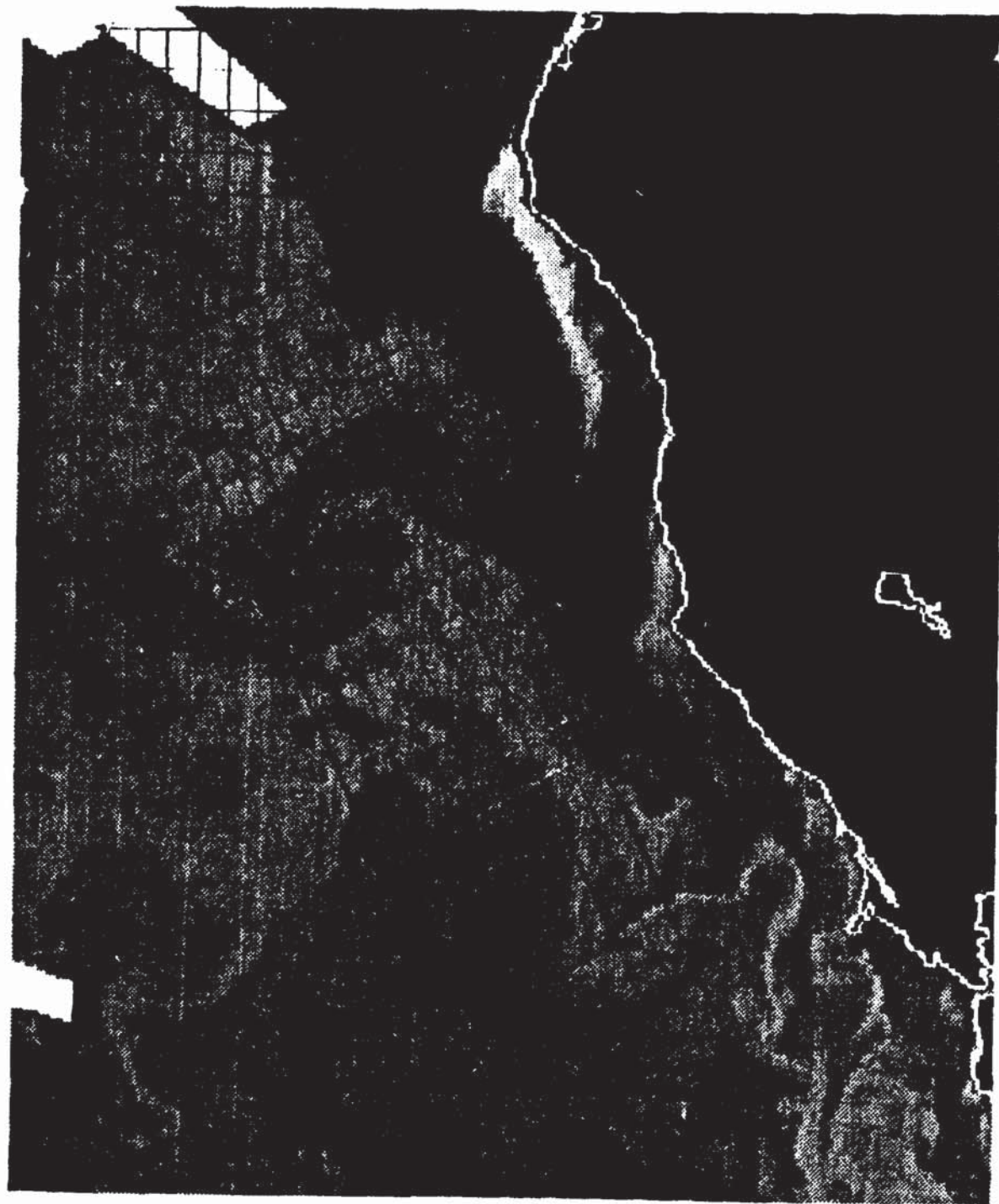
Chu, P. C., "Three Dimensional Eastern Greenland Sea Circulation Computed From A CTD Data Set", ARCSS Ocean-Atmosphere-Ice Interactors, NSF, pp. 61-64, 1992.

Chu, P. C., "Three Dimensional Pseudovorticity Field In The West Spitsbergen Current", Polar Meteorology and Oceanography, III, pp.101-104, 1992.

Doswell, C.A., "Obtaining Meteorologically Significant Surface Divergence Fields Through the Filtering Property of Objective Analysis, "*Mon. Wea. Rev.*, No. 105, pp. 885-892, 1977.

Eliassen, A., "On The Vertical Circulation In Frontal Zones," *Geophys. Publ.* 24, No. 4, pp. 147-160, 1962.

Gill, Adrian E., *Atmosphere-Ocean Dynamics*, Academic Press, Inc., 1982.

Hickey, Barbara, "Poleward Flow Near The Northern And Southern Boundaries Of The U.S. West Coast," *Poleward Flows Along Eastern Ocean Boundaries* Springer-Verlag, pp. 160-175, 1989.

Hoskins, B. J., Draghich, I., and Davies, H. C., "A New Look At The ω-Equation," *Quart. J. Roy. Meteor. Soc.*, 104, 31-38, 1978.

Huyer, Adriana, "Coastal Upwelling In The California Current System," *Prog. Oceanog* Vol. 12, pp. 259-284, 1983.

Huyer, Adriana, Kosro, P.M., Lentz, S.J., Beardsly, R.C., "Poleward Flow In The California Current System," *Poleward Flows Along Eastern Ocean Boundaries* Springer-Verlag, pp. 142-159, 1989.

Jessen, P. F., *Hydrographic Data From The Pilot Study Of The Coastal Transition Zone (CTZ) Program 17-26 March 1987*, Report for The Naval Postgraduate School Research Council, 1989.

Kosro, P. Michael, et al., "The Structure Of The Transition Zone Between Coastal Waters And The Open Ocean Off Northern California, Winter And Spring 1987,"*Journal of Geophysical Research,* Vol. 96, pp. 14,707-14,730, 1991.

Large, W. G., and S. Pond, "Open Ocean Momentum Flux Measurements In Moderate To Strong Winds,"*J, Phys. Oceanogr.,* 11, 324-336, 1981.

Maddox, R. A., "An Objective Technique For Separating Macroscale and Mesoscale Features in Meteorological Data," *American Meteorological Society,* 108, 1108-1121, 1980.

Pickard, George L., and Emery, William J., *Descriptive Physical Oceanography: An Introduction,* 4th Ed., Pergamon Press, 1982.

Nelson, C. S., "Wind Stress And Wind Stress Curl Over The California Current," NOAA Tech. Rept. NMFS SSRF-714, 1977.

Pond, Stephen, and Pickard, George L.,*Introductory Dynamical Oceanography,* 2nd Ed., Pergamon Press, 1983.

Simpson, James J., "El Niño-Induced Onshore Transport In The California Current During 1982-1983," *Geophysical Research Letters,* Vol. 11, No. 3, pp. 241-242, March, 1984.

Tintoré, J. D., Gomis, D., Alonso, S., Parrilla, G., "Mesoscale Dynamics And Vertical Motion In The Alborán Sea,"*Journal of Physical Oceanography,* 811-823, 1991.

Xu, Q., "Ageostrophic Pseudovorticity And Geostrophic C-Vector Forcing A New Look At The Q-Vector in Three Dimensions," *Journal of Atmospheric Science,* 49, 981-990, 1992.

INITIAL DISTRIBUTION LIST

1. Defense Technical Information Center   2
    Cameron Station
    Alexandria, VA 22304-6145

2. Library, Code 52   2
    Naval Postgraduate School
    Monterey, CA 93943-5000

3. Chairman (Code OC/Co)   1
    Department of Oceanography
    Naval Postgraduate School
    Monterey, CA 93943-5000

4. Chairman (Code MR/Hy)   1
    Department of Meteorology
    Naval Postgraduate School
    Monterey, CA 93943-5000

5. Mr. P. C. Chu
    Associate Professor   1
    Department of Oceanography
    Naval Postgraduate School
    Monterey, CA 93943-5000

6. Mr. R.W. Garwood
    Professor
    Department of Oceanography
    Naval Postgraduate School
    Monterey, CA 93943-5000   1

7. Commander   1
    Naval Oceanography Command
    Stennis Space Center
    MS 39529-5000

8. Chairman   1
    Oceanography Department
    U.S. Naval Academy
    Annapolis, MD 21402

94

9.   Office of Naval Research   1
     Naval Ocean Research and Development Activity
     800 N. Quincy Street
     Arlington, VA 22217

10. Director   1
     Instituto Oceanografico de la Armada
     Primera Zona Naval
     Guayaquil, Ecuador

11. Lt. Gonzalo Montenegro   2
     Juan Ignacio Pareja #136
     Sector Colegro la Dolorosa
     Quito, Ecuador